

**Study on Damage Identification Approaches for
Ultrasonic Lamb Wave-based Structural Health
Monitoring and Off-line Non-destructive Evaluation**

January 2015

Yaolu Liu

Graduate School of Engineering

CHIBA UNIVERSITY

(千葉大学審査学位論文)

**Study on Damage Identification Approaches for
Ultrasonic Lamb Wave-based Structural Health
Monitoring and Off-line Non-destructive Evaluation**

January 2015

Yaolu Liu

Graduate School of Engineering

CHIBA UNIVERSITY

ABSTRACT

Ultrasonic Lamb waves are the elastic waves in plate-like structures, which have been acknowledged as an effective tool for damage detection and identification. Ultrasonic Lamb wave-based Structural Health Monitoring (SHM) and off-line Non-Destructive Evaluation (NDE) techniques have been employed for damage prognosis of various structures including ground vehicles, ship and aerospace structures, bridges, pipelines and offshore platforms. They not only provide real-time or on-demand information about the condition of the monitored or evaluated structures, the output can be used to locate damage and evaluate the severity of the damage. The current research is a part of an ongoing multidisciplinary effort to develop Ultrasonic Lamb wave-based SHM and off-line NDE systems for engineering structures.

This dissertation firstly constructs a pseudospectral Mindlin plate element to perform wave propagation analyses of plate-like structures. Chebyshev polynomials are used as base interpolation functions and Chebyshev-Gauss-Lobatto points are used as grid points of the new Mindlin plate element. Furthermore, an untraditional numerical integration scheme, i.e., Chebyshev points quadrature (CPQ), is suggested by us to form the elemental mass matrix and stiffness matrix. The efficiency and high accuracy of the present pseudospectral Mindlin plate element are proven by solving wave propagation problems of one dimension (1D) and two dimensions (2D) and comparing its results with the results obtained by ABAQUS and experiments.

Secondly, the physical mechanisms behind wave propagation and wave

interaction with damage are studied by using the pseudospectral Mindlin plate element to make the interpretation of damage detection or damage evaluation results more easily. Aluminum plates with a through-thickness elliptically-shaped damage are used to investigate the influence of Lamb wave dispersion, the shape of damage, the excitation frequency in wave signals and the incident angle of the Lamb wave on the relative reflection intensity (RRI). The obtained numerical results show that the dispersion of the Lamb wave has no obvious effect on the RRI, whereas the other parameters mentioned above have remarkable influences on the RRI from elliptically-shaped damages. The results obtained can be helpful for understanding the complex interactions between Lamb waves and various areas of damage, for designing actuator/sensor placements and input wave signals, and for improving the reliability of methods of damage identification based on the analysis of signals reflected wave from damage.

Thirdly, inspired by the results of the influence of the shape of damage and the incident angle of the Lamb wave on RRI, for off-line NDE, a new wave energy flow (WEF) map concept is proposed and multiple lead zirconate titanate (PZT) sensors instead of a single acoustic emission (AE) sensor used in a conventional technique mentioned below are employed to improve the visualization technique using ultrasonic Lamb wave propagation proposed by Takatsubo *et al.*. The improved structural damage imaging approach can not only locate damage but also evaluate the shape and size of damage. Various damages in aluminum and carbon fiber reinforced plastic laminated plates are experimentally and numerically evaluated to validate the improved approach. The results show that it can effectively evaluate the shape and size of damage from wave field

variations around the damage in the WEF map.

Finally, for SHM, the present study focuses on monitoring local plasticity for the prediction of defect emergence in advance. A real-time monitoring technique for local plasticity using Lamb waves is developed. Tensile test of a thin aluminum plate with a circular hole is conducted to verify the effectiveness of the proposed technique. In this test, high stress concentration is induced around the hole, which led to local plasticity. During the tensile test, a series of wave signals passing through the local plastic region are collected using a directional actuator/sensor set to monitor the evolution of plasticity. Pulse compression technique is used to process the wave signals. With the increase of the tensile stress in the specimen, the changes of wave amplitudes of S_0 and A_0 modes are obtained, and the difference of Lamb wave signals is further evaluated using a proposed signal index I calculated by wavelet analysis. Combined with the numerical stress analysis of the tensile specimen, the influence of the plasticity on the amplitudes of S_0 and A_0 wave modes is analyzed. As the plastic zone grows gradually, the wave amplitudes and I of S_0 and A_0 wave modes show their different change tendencies compared with those in elastic stage. The amplitude change is more sensitive to the mild plasticity than the change of I , while the change of I caused by the severe plasticity is more obvious than the amplitude change.

ACKNOWLEDGMENT

It is a pleasure to express my sincere thankfulness to all who encouraged and supported me during my Ph.D. studies at Chiba University.

First and foremost I want to thank my advisor, Professor Ning Hu, who is my best role model of an outstanding scholar. For my all progress in accomplishing this thesis I am indebted to his extraordinary supervision. He has always been supporting me, provided whatever resources necessary to accomplish my goals. His valuable advice and philosophy on technical as well as personal matters will be a great treasure in my future career and life.

I am also grateful to the all members of Prof. Hu's Laboratory in Chiba University for their helps in experiments and computations, valuable discussions, technical support, and finally valuable comments during this thesis preparation.

Special thanks to MEXT scholarship for providing me the invaluable opportunity to study in Chiba University.

Finally, I am forever thankful to my parents, my husband and my son. Words fail me to express my appreciation to them for their dedication, love and support.

Acknowledgment

TABLE OF CONTENTS

ABSTRACT	I
ACKNOWLEDGMENT	V
TABLE OF CONTENTS	VII
LIST OF FIGURES.....	XI
LIST OF TABLES.....	XVI
Chapter1	1
Introduction	1
1.1 Background	2
1.2 Ultrasonic Lamb waves.....	5
1.2.1 Multimode of Lamb waves	6
1.2.2 Dispersion of Lamb waves.....	8
1.2.3 Generation of Lamb waves	13
1.3 Approaches for ultrasonic Lamb wave-based SHM and off-line NDE ..	14
1.3.1 Phase arrays.....	15
1.3.2 Lamb wave tomography.....	17
1.3.3 ANN	18
1.3.4 Time reversal	19
1.4 Thesis objectives	20
1.5 A preview of the thesis content	20

References	22
Chapter 2.....	31
Construction of a pseudospectral Mindlin plate element.....	31
2.1 Introduction	32
2.2 Description of pseudospectral Mindlin plate element	34
2.2.1 Shape functions and grid points	34
2.2.2 Theory of pseudospectral plate element and integration scheme.....	36
2.3 Effectiveness of pseudospectral Mindlin plate element	42
2.3.1 A 1D wave propagation problem	42
2.3.2 A 2D wave propagation problem	43
2.4 Conclusion	50
References	50
Chapter 3.....	53
Study on the interaction of ultrasonic Lamb waves with elliptically-shaped damages in metallic plates.....	53
3.1 Introduction	54
3.2 Influence of Lamb wave dispersion on RRI from damage	56
3.3 Influences of the damage geometry, incident angle and signal frequency on RRI from damage	65
3.3.1 Effect of damage shape	65

3.3.2 Effect of excitation frequency	71
3.3.3 Effect of incident angle of Lamb waves	76
3.4 Conclusion	79
References	80
Chapter 4.....	83
Development of a structural damage imaging approach based on a Wave Energy Flow (WEF) map	83
4.1 Introduction	84
4.2 A technique based on WEF map	87
4.3 Experimental and numerical procedures for damage evaluation.....	90
4.3.1 Experimental set-up	90
4.3.2 Evaluation of damage in aluminum plates	92
4.3.3 Evaluation of delamination in a CFRP laminated plate	102
4.4 Conclusion	109
References	110
Chapter 5.....	113
Development of a real-time technique for monitoring local plasticity using Ultrasonic Lamb waves	113
5.1 Introduction	114
5.2 Pre-requisite experiments	116

5.3 Description of experimental scheme	125
5.4 Experimental results	126
5.5 Discussion.....	132
5.5.1 0 MPa~130 MPa.....	134
5.5.2 130 MPa~155 MPa.....	135
5.5.3 155 MPa~180 MPa.....	135
5.6 Conclusion	136
References	137
Chapter 6.....	141
Summary and Future work.....	141
6.1 Summary of the thesis study.....	142
6.2 Further work	145

LIST OF FIGURES

Figure 1.1 Graphical illustration of basic ultrasonic wave modes	6
Figure 1. 2 The shapes of two types of Lamb wave modes	7
Figure 1.3 Phase velocity dispersion curves for the first two symmetric and antisymmetric Lamb wave modes using the material properties of aluminum.....	12
Figure 1.4 Group velocity dispersion curves for the first two symmetric and antisymmetric Lamb wave modes using the material properties of aluminum.....	12
Figure 1.5 Wavelength curves for the first two symmetric and antisymmetric Lamb wave modes using the material properties of aluminum.....	13
Figure 1.6 Tomographic reconstructions of a 1 inch diameter flat-bottom-hole 30% thickness loss: (a) parallel-projection result; (b) fan-beam result; (c) double-crosshole result.....	18
Figure 2.1 A 6×6 spectral plate element.....	35
Figure 2.2 Mesh and loads for computation of ABAQUS	45
Figure 2.3 Comparison between the present numerical method and ABAQUS: (a) 50 kHz; (b) 100 kHz; (c) 200 kHz.....	46
Figure 2. 4 Visualization system of wave propagation in an aluminum plate with a hole of diameter of 2 cm: (a) experimental setup for wave propagation visualization (length unit: mm); (b) enlarged scanning area (length unit: mm) (50 \times 50 grids with 2 mm step size)	47
Figure 2. 5 Input signal for simulating the excitation force	48

Figure 2. 6 Comparison of wave propagation results: (a) experimental ($t = 45 \mu\text{s}$); (b) experimental ($t = 71.35 \mu\text{s}$); (c) numerical ($t = 71.35 \mu\text{s}$)	49
Figure 3.1 Group and phase velocities and wavelength of A_0 mode for an aluminum plate of 5 mm thickness: (a) group velocity; (b) phase velocity; (c) wavelength	58
Figure 3.2 Computational model for investigating influence of dispersion: (a) a model of two sensor sets and one actuator set without damage; (b) mesh in numerical simulations	61
Figure 3.3 Wave signals of two sensor sets ($N=5, f= 80 \text{ kHz}$).....	63
Figure 3.4 Numerical results about the influence of wave dispersion	64
Figure 3.5 Computational model for damaged case	65
Figure 3.6 Shape of an elliptical hole	66
Figure 3.7 Waveform received by the sensor ($N=5, f=100 \text{ kHz}$)	66
Figure 3.8 Lamb wave propagation images at $t=62.96 \mu\text{s}$ and $83.95 \mu\text{s}$ for a circular hole	69
Figure 3.9 Reflection intensity versus A/B	70
Figure 3.10 Comparison of reflections from a crack and a circular hole: (a) a crack; (b) a circular hole	70
Figure 3.11 Influence of excitation frequency on reflection intensity	73
Figure 3.12 Images of Lamb wave propagation at two frequencies: (a) hole (100 kHz, $t=83.95 \mu\text{s}$); (b) hole (260 kHz, optimal excitation frequency, $t=62.96 \mu\text{s}$); (c) crack (100 kHz, $t=73.87 \mu\text{s}$); (d) crack (200 kHz, optimal excitation frequency, $t=62.96 \mu\text{s}$).....	75
Figure 3.13 Definition of incident angle of Lamb waves to a crack.....	76

Figure 3.14 Incident angle versus reflection intensity	77
Figure 3.15 Incident angle versus reflection intensity for θ_2 and θ_3	78
Figure 4.1 Schematic illustration of experimental setup.....	87
Figure 4.2 Aluminum plates: (a) with an elliptical through-hole; (b) with a non-penetrating slit; (c) position of sensors and damage.....	94
Figure 4.3 Experimental images of Lamb waves (time=70 μ s) using previous technique [19–21] for the aluminum plate with an elliptical through-hole: (a) PZT-1; (b) PZT-2; (c) PZT-3	95
Figure 4.4 Experimental images of γ distribution using the present WEF map technique for the aluminum plate with an elliptical through-hole: (a) PZT-1; (b) PZT-2; (c) PZT-3; (d) PZT-(1+2+3)	96
Figure 4.5 Numerical result images of γ distribution using the present WEF map technique for the aluminum plate with an elliptical through-hole: (a) PZT-1; (b) PZT-2; (c) PZT-3	97
Figure 4.6 Experimental images of γ distribution for the aluminum plate with a non-penetrating slit (irradiated side with slit): (a) PZT-1; (b) PZT-2; (c) PZT-3; (d) PZT-(1+2+3).....	100
Figure 4.7 Experimental images of γ distribution for the aluminum plate with a non-penetrating slit (irradiated side without slit, result of PZT-(1+2+3))	101
Figure 4.8 Test specimen of a CFRP laminated plate: (a) delamination damage; (b) position of sensors and damage.....	103
Figure 4.9 Images of delamination using traditional ultrasonic C-scan: (a) impacted side; (b) opposite side of impact	103

Figure 4.10 Experimental images of Lamb waves for CFRP laminate with delamination (time=40 μ s, 60 μ s) using the previous technique [15–17]: (a) PZT-1; (b) PZT-2; (c) PZT-3.....	104
Figure 4.11 Experimental images of γ distribution using the present WEF map technique: (a) PZT-1; (b) PZT-2; (c) PZT-3; (d) PZT-(1+2+3).....	105
Figure 4.12 Amplitude of Lamb waves versus propagation distance (5 mm increment) and propagation direction (30° increment) in a CFRP plate: (a) relationship between distance of propagation and amplitude (fitted by least squares method of a linear relationship); (b) experimental model of the measurement	108
Figure 4.13 Damage image using absolute value of sensor signals in a CFRP plate with delamination.....	108
Figure 5.1 Schematic view of experimental specimen	118
Figure 5.2 Nominal stress-nominal strain curves.....	118
Figure 5.3 Schematic view of experiment (rectangular-type PZT used as actuator)	
.....	120
Figure 5.4 Input signal: (a) waveform in time domain; (b) FFT spectrum	121
Figure 5.5 Dispersion curves of group velocity for an aluminum plate	121
Figure 5.6 Amplitudes of generated Lamb waves in different directions: (a) S_0 mode; (b) A_0 mode	122
Figure 5.7 Schematic view of experiment (rectangular-type PZT used as sensor)	
.....	123
Figure 5.8 Amplitudes of received Lamb waves in different directions: (a) S_0 mode; (b) A_0 mode	124

Figure 5.9 Experimental setup	126
Figure 5.10 Wave signals: (a) original wave signals at different stress levels; (b) wave signals processed by pulse compression technique at different stress levels.....	129
Figure 5.11 Pulse compression technique	130
Figure 5.12 Amplitude change of S_0 Lamb mode with the increase of stress level in the specimen.....	130
Figure 5.13 Amplitude change of A_0 Lamb mode with the increase of stress level in the specimen.....	131
Figure 5.14 Wavelet analysis of signals	131
Figure 5.15 Signal index I related to different stress levels: (a) A3; (b) D1; (c) D2; (d) D3	132
Figure 5. 16 Evolution of plastic zone during loading process: (a) 75 MPa; (b) 120 MPa; (c) 155 MPa; (d) 160 MPa; (e) 170 MPa; (f) 180 MPa	133
Figure 5.17 Lamb wave propagation model (one dimension)	134

LIST OF TABLES

Table 1.1 Material properties of aluminum.....	11
Table 2.1 Material properties of piezoelectric actuator.....	48
Table 3.1 Material properties of PZT and aluminum	57
Table 3.2 Incident angle of Lamb waves	77
Table 5.1 Material properties of A5052 aluminum.....	117

Chapter1

Introduction

1.1 Background

In recent years, with the developments in aerospace, civil and mechanical engineering, the significance of damage prognosis system in various structures, such as commercial aircrafts, civil infrastructures and manufacturing equipment, has increased dramatically. It is envisioned that a damage prognosis system could evaluate the current state of a structure, apprise the user of any incipient damage information in real-time or off-line and then predict the remaining useful life of the structure through simulations and past experiences. Such a damage prognosis system is very important for the modern society of human being. Taking the commercial aircrafts for example, there is a trend that various composite materials are more and more popular to the components of the airplanes. For instance, composite materials already make up 50 percent of the primary structure of the Boeing 787, including the fuselage and wing. The higher stiffness-to-mass ratio of the composite materials compared to conventional metals is the primary advantage, which would lead to higher efficiency of fuel consumption and lower operational cost for aerospace vehicles. Moreover, composite materials are able to resist corrosion more effectively and can be tailored in stiffness and strength in some specific directions associated with the situation of bearing loads. However, composite materials are more brittle than wrought metals and thus are more easily damaged by impact events. The impact damage always appears in the form of delamination, cracks or fiber breakage, which could remarkably reduce the strength of the materials and potentially lead to structural failure. The damage prognosis system could improve the confidence in the use of the composite structures by monitoring the state of the structure and informing any unexpected

impact events to operators. For civil infrastructures, there is also a need for damage prognosis of structures, such as bridges and high-rise buildings which are subjected to earthquakes or strong wind loads. The prognosis would estimate the condition of the civil structures and then confidently predict the response of the structures to future loading such as the inevitable aftershocks. A successful assessment and repairing projects could minimize the losses of the society. Hence, it is worth to put great effort into damage prognosis system to ensure the structural safety and economic benefits.

Non-destructive evaluation (NDE) and structural health monitoring (SHM) are two very important elements of the damage prognosis system. NDE is aimed to evaluate the properties of a material, structure or system without causing damage. The history of NDE can be traced back to the 1920s. At that time the magnetic particle tests (MT) and X-radiography (RT) began to be used in the medical field. From the late 1950s, NDE has seen exponential progress. Many approaches for NDE, such as infrared thermography, eddy current, ultrasonic C-scan, optical methods, etc., have been developed and widely used to examine metal materials, non-metallic materials, composite materials and their products in practices. However, approaches for NDE are time-consuming and labor intensive and the examined subjects always require structures being out of services, leading to a large economic loss. Regular maintenance for aircraft using NDE to ensure flight safety is an example which usually takes several hundred hours for inspection.

Therefore, since recent 20 years, SHM has been widely developed. It becomes a very important element of the damage prognosis system. The goal of

SHM is to provide real-time or on-demand information about the condition of the monitored structures to detect the present of damage and obtain detailed information about damage. An integrated SHM should involve sensory system, data acquisition and transmission, data processing and data interpretation. The design of sensory system includes the choice of sensors and their optimal placement. Sensors are classified by the capability of measuring desired physical like displacement, velocity, acceleration, pressure, strain, temperature and so on. Attributes of sensors, such as size, sensitivity, physical contact and operating principle, can be used as the criterions for sensor selection. The main tasks of data processing are related to signal de-noising and compression to produce meaningful information. There are a lot of signal processing technologies among which wavelet theory, a novel signal processing technology developed in recent years, has exhibited the validity of bridging data processing and SHM. The core knowledge of SHM is the interpretation of data, i.e., damage detection algorithm, which is aimed to obtain the information of the change in structural properties (mass, stiffness, damping) through monitoring the changes in static and dynamic responses of the structure. There are considerable researches that have been conducted on developing various damage algorithms to satisfy different features extracted from signal data.

Besides, SHM has the difference between active systems and passive systems depending on whether or not they involve the use of actuators. Passive systems make use of transducers that are only intended to “listen” the response of the structure. Acoustic emission (AE) and strain/loads monitoring are the most well-known examples of passive systems. For an AE-based SHM system, a

considerable number of sensors are distributed and attached on the surface of a structure or embedded in a structure to actively sense its response at discrete time intervals. It is usual to use the acoustic energy emitted by the creation or growth of a crack to determine its presence and location. For strain/load monitoring SHM system, strain gages are used to make sure that the applied loads would not exceed the predetermined critical load. However, both the above two kinds of SHM systems suffer from the drawback of requiring high sensor densities on the structure. Moreover, passive systems probably become invalid until an undesirable threshold or damage extent has been reached. Active systems are another alternative for SHM to make up the deficiency of the passive systems. In the active systems, a structure can be inspected at any time and position required by using actuators to excite the structure in a prescribed manner which can be repeated to ensure the reliability of inspection results. Among numerous schemes for the active systems, Ultrasonic Lamb waves-based SHM system is an attractive option since it can offer an effective method to evaluate the position, type and severity of damage.

In addition, it is well-known that ultrasonic Lamb waves are also widely used in NDE. Therefore, ultrasonic Lamb wave and the approaches used in SHM and NDE will be introduced in the following sections.

1.2 Ultrasonic Lamb waves

Ultrasonic Lamb waves are waves of plane strain that occur in a free plate. The only condition for these waves is that the associated traction force must vanish on the upper and lower surface of the plate. The wave theory shows two basic

vibration modes of motion with respect to the wave type generated in the material. This is illustrated graphically in Figure 1.1. In longitudinal waves (P), particles of the medium move in a direction parallel to the energy transport (or the wave velocity vector). In transverse or shear waves (S), particles of the medium move in a direction perpendicular to energy transport. When the transverse waves are described in the direction parallel to the plate, they form shear horizontal (SH) waves. In contrast, when the transverse waves are described in the direction perpendicular to the plate, they form shear vertical (SV) waves. Ultrasonic Lamb waves arise from a coupling between shear and longitudinal waves reflected between the top and bottom surfaces of a plate.

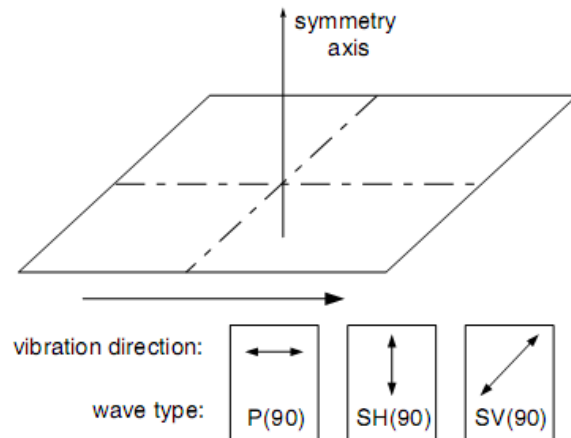


Figure 1.1 Graphical illustration of basic ultrasonic wave modes

1.2.1 Multimode of Lamb waves

Different wave modes can occur in a plate as the angle of wave incidence and the wave frequency are varied. The variety of modes can be classified as either antisymmetric, where the whole plate moves in a flexural motion, or symmetric,

where the center or neutral plane of the plate is stationary. Figure 1.2 shows the shapes of two types of Lamb wave modes. Each of these classes contains a series of zero and higher order modes. These are denoted by: A_0 , A_1 , A_2 , etc. for antisymmetric modes and S_0 , S_1 , S_2 etc. for symmetric modes. In general, Lamb wave propagation is in directions parallel to the plate faces and is dispersive, i.e., the phase and group velocities are frequency dependent. The two zero-order modes, denoted by A_0 and S_0 , can exist at all frequencies, whereas higher-order modes have cut-off frequencies (f_c) for a given sample, below which they cannot exist [1]. These frequencies are given by

$$f_c = nv_l/4b \text{ for } n = 1, 2, 3, \dots \quad (1.1a)$$

$$f_c = nv_t/4b \text{ for } n = 2, 4, 6, \dots \quad (1.1b)$$

$$f_c = nv_l/4b \text{ for } n = 2, 4, 6, \dots \quad (1.2a)$$

$$f_c = nv_t/4b \text{ for } n = 1, 2, 3, \dots \quad (1.2b)$$

where v_l and v_t are the longitudinal and transverse velocities, respectively.

A characteristic of the two types of mode is that, in general, the symmetric modes have a large in-plane component of particle motion, whereas the antisymmetric modes exhibit a significant feature of out-of-plane motion. Note that for a given plate thickness $2b$, there is a frequency limit given by f_c in

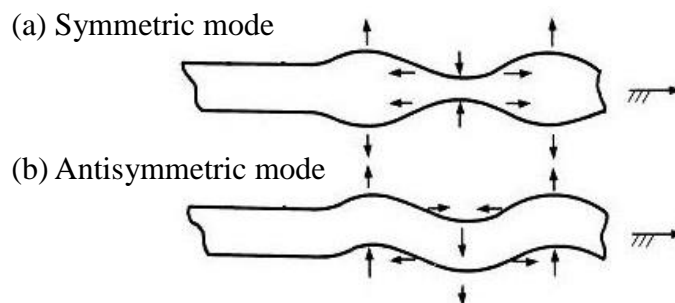


Figure 1.2 The shapes of two types of Lamb wave modes

Equations (1.1) and (1.2) below which only the A_0 and S_0 modes exist.

1.2.2 Dispersion of Lamb waves

Lamb waves are a form of elastic perturbation that can propagate in a solid plate with free surface boundaries [2, 3]. This type of wave phenomenon was first described in theory by Horace Lamb in 1917, however, he never attempted to reproduce them [4]. The two groups of Lamb waves (symmetric and antisymmetric modes) satisfy the wave equation and boundary conditions for this problem and each can propagate independently of the other. The dispersion is a very significant characteristic of Lamb waves, which largely limits the application of Lamb waves to SHM or NDE due to varying wave speeds. To effectively apply Lamb waves to SHM or NDE, Lamb wave propagation must be studied in detail. The fundamental way to describe the propagation of a Lamb wave in a particular material is to employ their dispersion curves, which plot the phase and group velocities versus the excitation frequency.

1.2.2.1 Rayleigh-Lamb equations

The wave equations describing Lamb wave propagation are Rayleigh-Lamb equations, which are expressed as:

Symmetric mode:

$$\frac{\tan k_t b}{\tan k_l b} = - \frac{4k_0^2 k_l k_t}{(k_0^2 - k_t^2)^2} \quad (1.3a)$$

Antisymmetric mode:

$$\frac{\tan k_t b}{\tan k_l b} = - \frac{(k_0^2 - k_t^2)^2}{4k_0^2 k_l k_t} \quad (1.3b)$$

$$k_l^2 = \left(\frac{\omega}{c_l}\right)^2 - k_0^2 \quad (1.4a)$$

$$k_t^2 = \left(\frac{\omega}{c_t}\right)^2 - k_0^2 \quad (1.4b)$$

where k_0 is the wave number in horizontal direction parallel to the plate face; b is the half thickness of plate; ω is the angular frequency ($\omega = 2\pi f$); v_l is the longitudinal velocity and v_t is the transverse velocity.

The two transcendental equations seem simple and easy to be solved, but the fact is not such. Although the frequency equations had been derived since the end of the 19th century, until to the sixties of the twentieth century, Mindlin [5] solved them in detail [1].

The set of wave equations determines the dispersion of Lamb wave, that is, the relation between ω and k_0 is nonlinear for Lamb modes, and different Lamb modes have different nonlinear relations. Because the relation between ω and k_0 is not linear, the phase velocity $c_{phase} = \omega/k_0$ is not a constant, but varies along with the variety of frequency. The group velocity c_{group} of Lamb wave propagation in a plate is different from the phase velocity, which is also solved later.

1.2.2.2 The analysis of Rayleigh-Lamb equations

Dispersion curves are the fundamental way to describe the propagation of Lamb waves, in the following text, the derivation of these curves will be discussed in detail.

The solution to the wave equation for the symmetric Lamb wave is:

$$\frac{\tan \sqrt{1-\zeta^2} d}{\tan \sqrt{\xi^2 - \zeta^2} d} = -\frac{4\zeta^2 \sqrt{1-\zeta^2} \sqrt{\xi^2 - \zeta^2}}{(2\zeta^2 - 1)^2} \quad (1.5a)$$

The solution to the wave equation for the antisymmetric Lamb wave is:

$$\frac{\tan \sqrt{1-\zeta^2} \bar{d}}{\tan \sqrt{\xi^2 - \zeta^2} \bar{d}} = -\frac{(2\zeta^2 - 1)^2}{4\zeta^2 \sqrt{1-\zeta^2} \sqrt{\xi^2 - \zeta^2}} \quad (1.5b)$$

where the non-dimensional parameters are:

$$\xi^2 = \frac{c_t^2}{c_l^2}, \quad \zeta^2 = \frac{c_t^2}{c_{phase}^2}, \quad \bar{d} = k_t b \quad (1.6)$$

These velocities can be defined by Lame's constants:

$$\mu = \frac{E}{2(1+v)}, \quad \lambda = \frac{Ev}{(1-2v)(1+v)} \quad (1.7)$$

$$c_t^2 = \frac{\mu}{\rho}, \quad c_l^2 = \frac{(\lambda + 2\mu)}{\rho}, \quad k_t = \frac{\omega}{c_t} \quad (1.8)$$

Substituting these equalities into the non-dimensional parameters yields:

$$\xi^2 = \frac{\mu}{(\lambda + 2\mu)} = \frac{1-2v}{2-2v} \quad (1.9a)$$

$$\zeta^2 = \frac{\mu}{\rho c_{phase}^2} = \frac{E}{2\rho(1+v)c_{phase}^2} \quad (1.9b)$$

$$\bar{d} = \frac{\omega b}{c_t} = \omega b \sqrt{\frac{\rho}{\mu}} = \omega b \sqrt{\frac{2\rho(1+v)}{E}} \quad (1.9c)$$

Finally, Equations (1.9) can be substituted into Equations (1.5), which can be solved numerically. For a given material, the Young's modulus E , Poisson's ratio v , and the density ρ are known, and the phase velocity c_{phase} is the dependent variable to be solved. This independent variable is iteratively solved corresponding to the frequency-thickness product, where ω is the driving frequency in radians/sec. An example of the phase velocity dispersion curves for the first two symmetric and antisymmetric Lamb wave modes using the material properties of aluminum shown in Table 1.1 can be seen in Figure 1.3. The other

useful plot is the group velocity dispersion curve, which can be easily derived from the phase velocity curve using the following Equations (1.10):

$$k_0 = \frac{2\pi}{\lambda_w} (\text{wave number}) \quad (1.10\text{a})$$

$$\lambda_w = \frac{c_{phase}}{f} (\text{wavelength}) \quad (1.10\text{b})$$

$$c_{group} = c_{phase} + \frac{\partial c_{phase}}{\partial k_0} k_0 = \frac{c_{phase}}{1 - \frac{f}{c_{phase}} \cdot \frac{\partial c_{phase}}{\partial f}} \quad (1.10\text{c})$$

Again, by using the material properties of aluminum, an example of group velocity dispersion curves and wavelength curves can be seen in Figures 1.4 and 1.5. The equations presented here are intended for isotropic materials, however, it has been shown in the literature that the A_0 is fairly invariant to the layup of a composite material, and can be closely approximated by using the bulk laminate properties. Finite element techniques have been used by other researchers in the literature to more accurately determine the wave velocities in composite materials.

Table 1.1 Material properties of aluminum

E (GPa)	ρ (kg/m^3)	ν
68.9	2710	0.3

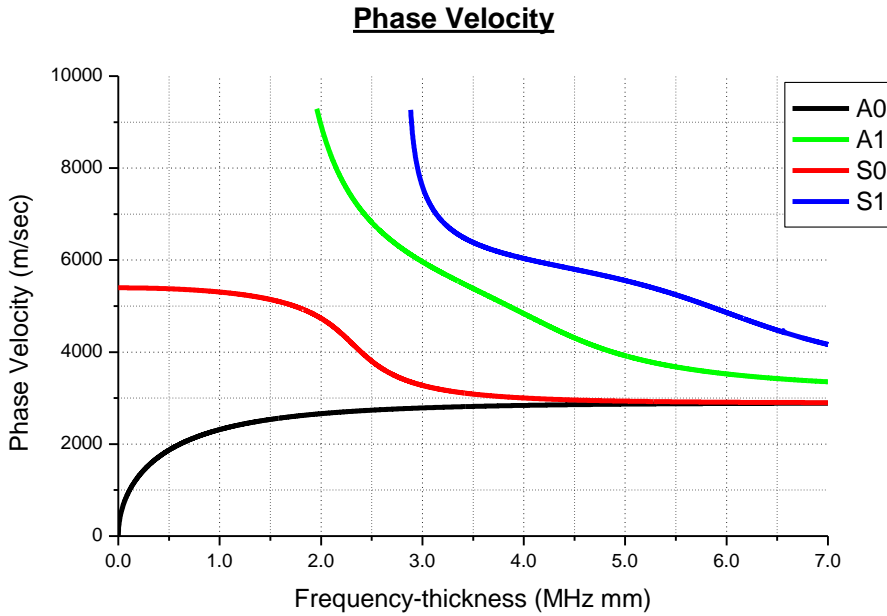


Figure 1.3 Phase velocity dispersion curves for the first two symmetric and antisymmetric Lamb wave modes using the material properties of aluminum

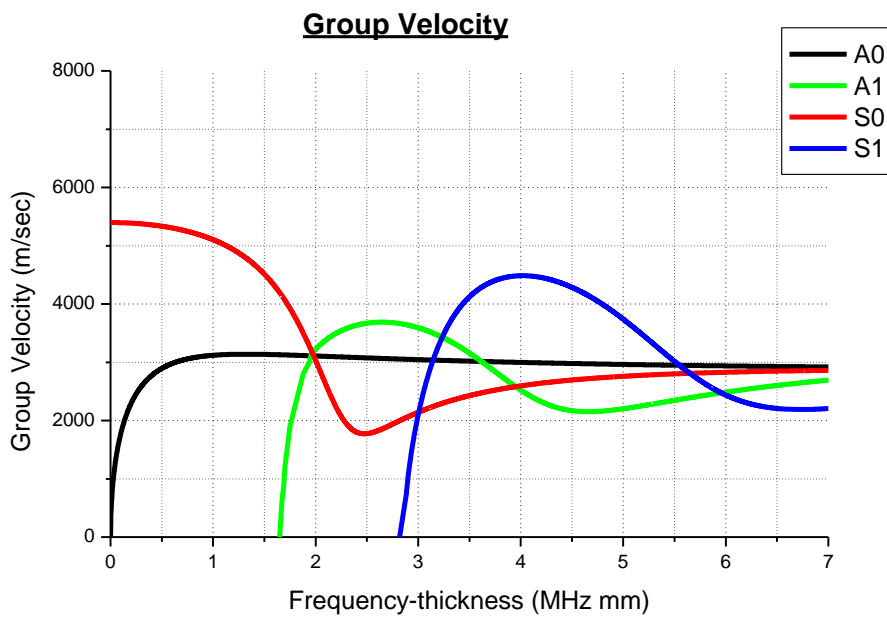


Figure 1.4 Group velocity dispersion curves for the first two symmetric and antisymmetric Lamb wave modes using the material properties of aluminum

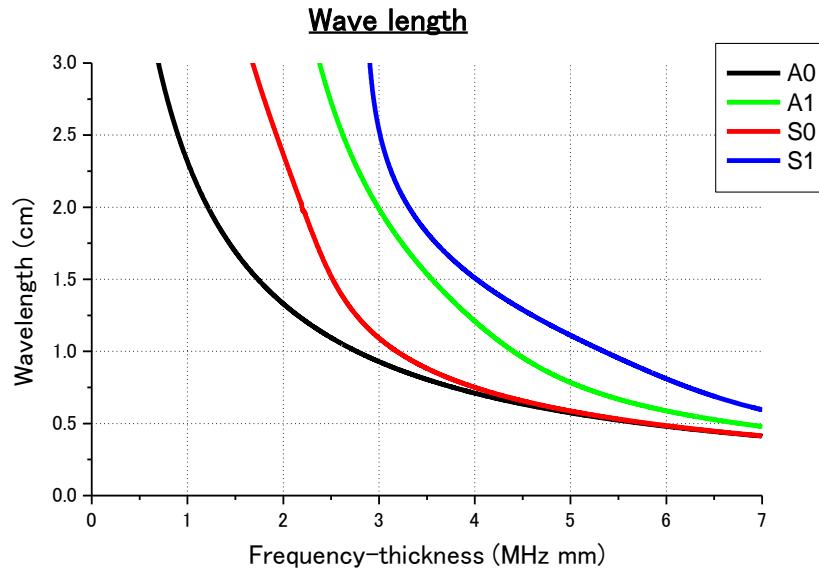


Figure 1.5 Wavelength curves for the first two symmetric and antisymmetric Lamb wave modes using the material properties of aluminum

1.2.3 Generation of Lamb waves

Lamb waves can be generated and collected by many different means, such as ultrasonic probe [6-12], laser [13-17], piezoelectric element [18-22], interdigital transducer [23-25], optical fiber [26-30], etc. Among those means, laser and Piezoelectric lead zirconate titanate (PZT) elements are the most common choices in damage detection researches.

1.2.3.1 Laser

Laser-based Ultrasonics (LBU) is a non-contact technique that uses laser to generate and detect ultrasonic Lamb waves. The basic components of LBU include a generation laser and a detection laser. The generation laser is a short pulse (from tens of nanoseconds to femtoseconds) and high peak power laser

employed for wave generation; the excited waves usually have a broad frequency range with several Lamb modes, providing more opportunities to select the desired modes. The detection laser is usually a continuous or long pulse (typically of tens of microseconds) laser employed in most methods of wave detection, among which laser interferometer is a reputable method for its high precision. In addition, LBU is an exceptionally effective approach for curved surfaces or complicated geometry.

1.2.3.2 PZT

PZT elements are particularly suitable for Lamb wave generation and acquisition because of their negligible mass/volume, excellent mechanical strength, easy integration, low power consumption, wide frequency responses, acoustic impedance and low cost. PZT elements are usually embedded in or surface-bonded on a structure. Because of the piezoelectric and inverse piezoelectric principles, when PZT is used as an actuator, applied high frequency voltage signal would cause waves to be excited in the structure; while used as a sensor, the in-plan strain over the PZT area would induces a voltage signal in the PZT element. There are numerous researches applied PZT to excite and collect Lamb waves for damage detection purpose. Lamb wave generated by PZT unavoidably includes multiple Lamb modes, thus signal processing techniques are required to deal with those complicated wave signals.

1.3 Approaches for ultrasonic Lamb wave-based SHM and off-line NDE

There are two configurations commonly used in ultrasonic Lamb wave-based

SHM and off-line NDE: pulse-echo and pitch-catch. In the former, a transducer is used as sensor as well as actuator. A narrow bandwidth pulse is applied to excite the structure, and echoes of the pulse coming from some internal material flaws are then detected. Suppose that the wave speed of the tone burst is known, and the wave signals from the boundaries can be removed by the filter method or subtracting the test signal from the baseline signal, wave signals from the internal material flaws are obtained if the flaws exist. Then the position of the flaws can be known using the wave speed and the time of flight between the incident wave and the wave reflected or scattered by damage. The representative approach using the pulse-echo configuration is phased arrays. In the second configuration, the actuator-sensor pairs are employed to excite the incident waves and receive the transmitted waves, respectively. This configuration is usually used in most approaches for damage detection based on ultrasonic Lamb waves, such as Lamb wave tomography, artificial neural networks (ANN), time reversal, and so on. Those approaches employ different damage features extracted from the test signals by a variety of signal processing techniques to classify the damage and to estimate its severity. In the following text, the main approaches used in ultrasonic Lamb wave-based SHM and off-line NDE are introduced for a review.

1.3.1 Phase arrays

As the name implies, phase arrays is an approach using a set of transducers, which are both suitable for SHM and off-line NDE. Each transducer is individually controlled in order to achieve the desired phased actuation. With such phased actuation, it is possible to promote constructive interference between the different

waves being generated by the several elements in the array-beam forming. Through the formation of a unified wave front, it is possible to increase the amplitude of generated, and consecutively, of reflected waves, increasing Signal to Noise Ratio (SNR) [31]. Although there are many types of phase arrays like rectangular and circular arrays, linear arrays that elements arranged on a straight line in one dimension are the most commonly used phased array for its simple configuration. Deutsch *et al.* [32] developed a self-focusing system which employs a linear phased array to generate Rayleigh and Lamb waves to locate damage in thin aluminum sheets with signal or multiple defects. Sundararaman *et al.* [33] presented a method for damage characterization in homogeneous and heterogeneous structures using beam formers produced by piezo-element linear phased arrays. Giurgiutiu *et al.* [34] put forward an “embedded ultrasonic structural radar” (EUSR) algorithm also using piezo-element linear phased arrays, which can accurately detect the broadside and the offside cracks in an aluminum plate specimen. Besides, the nonlinear phased arrays are also studied in some research works. Yu *et al.* [35] designed two non-uniform linear piezoelectric wafer active sensor (PWAS) arrays, the binomial array and the Dolph-Chebyshev array and experimentally verified their potential application. Marcus *et al.* [36] presented a minimum variance distortionless response (MVDR) approach for Lamb waves using a uniform rectangular array (URA) and a signal transmitter. The combination of the MVDR approach and the two-dimensional array improves the suppression of interfering Lamb modes. It can be seen from the past research work that phased arrays is a quite effective approach for damage detection.

1.3.2 Lamb wave tomography

Lamb wave tomography, mainly used in off-line NDE or SHM with a large number of actuator/sensor sets, is an imaging approach that surrounds the target area using a number of transducers, and lays down the scan lines through those determined actuators and sensors, then examines the distribution of the physical properties of the structure in target area, finally constructs an easily interpretable quantitative map of a characteristic parameter for damage identification. Parallel projection, crosshole projection and fan beam projection (see Figure 1.6 [37]) are three major schemes applied to Lamb wave tomography. Parallel projection is the one that has been most early used in the research work. Hutchins *et al.* [38-42], Nagata *et al.* [43] and Degertekin *et al.* [44] adopted a standard parallel-projection geometry with velocity and/or attenuation of Lamb waves as input for the tomographic reconstructions. However, compared to the two other schemes, crosshole projection is a more flexible and practical scheme [37]. In the research work done by McKeon and Hinders [45-49], besides the use of the parallel projection scheme, they also investigated the ‘crosshole’ tomographic scheme which is quite suitable for aircraft NDE. In addition, Hildebrand *et al.* [50] has done a preliminary pipe inspection study also using the crosshole tomographic scheme. The research work on fan beam projection is relatively less. Malyarenko and Hinders [51] compared two schemes of fan-beam and double-crosshole for mapping flaws in aging aircraft structures, and found the latter to be superior. It can be seen that Lamb wave tomography could rapidly inspect a large area but require a large number of sensors which may limit its applications for quick damage identification.

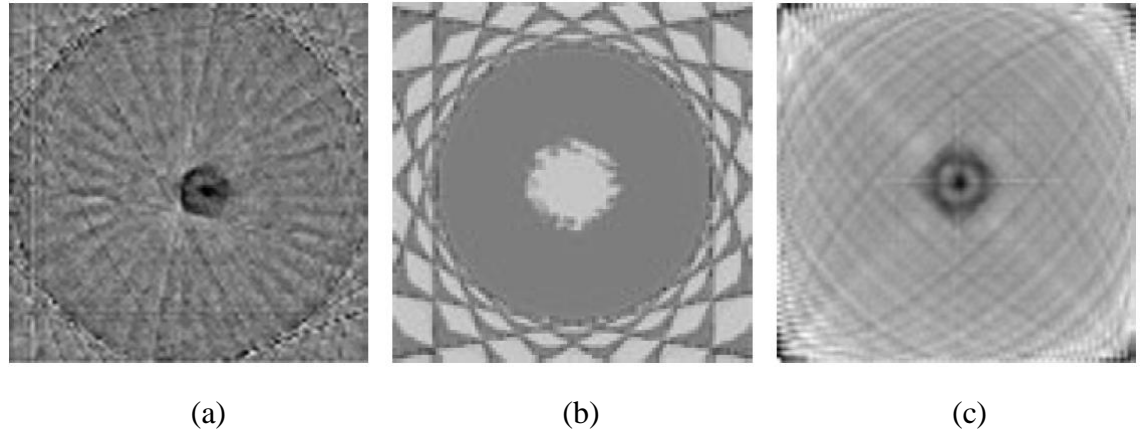


Figure 1.6 Tomographic reconstructions of a 1 inch diameter flat-bottom-hole 30% thickness loss: (a) parallel-projection result; (b) fan-beam result; (c) double-crosshole result

1.3.3 ANN

Inspired by the biological nervous systems, an efficient way of solving complex problems is to decompose them into many simpler and related elements as ‘neuron’ in nervous system for being able to understand them. An ANN is just such an approach. This approach is characterized by the two basic components, i.e., a set of nodes, and connection between nodes. The nodes can be thought of as computational units. They receive inputs and process them to obtain an output. The connections work as the interactions of nodes leading to a global behavior of the network [52]. A well-trained ANN can predict outcomes under an unknown stimulus according to pre-accumulated knowledge, while avoiding interrogating intricate constitutive relations. Various structural features, such as mode shape [53, 54], natural frequencies [55-58], combined modal information [59], acceleration

spectra [60], velocity and acceleration [61], applied force [62], displacement [63, 64], strain [65, 66], impedance [67] and so on, can be employed for network training [68]. Bork *et al.* [69, 70] developed a nondestructive technique for debonding in adhesively bonded joints by analyzing the transmitted ultrasonic Lamb wave signal with artificial neural networks. Yam *et al.* [71] put forward an integrated method for damage detection of composite using their vibration responses, wavelet transform and artificial neural networks. Su *et al.* [72, 73] also developed a damage identification technique for composite structures using ANN-interpreted Lamb wave signals. ANN is a promising solution for effective damage identification of some typical nonlinear inverse problems [74].

1.3.4 Time reversal

Time reversal is an approach that is based on the time-invariant and spatial reciprocity of a wave propagating in a medium. The time invariance means that a system output is invariable regardless of the time when an input is applied. The spatial reciprocity means that the position of a wave source and receiver can be interchanged without altering the result. Furthermore, it can be understood as the invariance of the wave equations in the time and space fields. For every wave from a source and possibly reflected, refracted, or scattered by any propagation media, there exists in theory a set of waves that precisely retraces all of these complex paths and converges in synchrony at the original source, as if time were going backward [75, 76]. However, this invariance would be broken down if a change (damage) appears in the propagating path of the wave. Wang *et al.* [77] investigated the applicability of the time-reversal concept to guided waves in

plates using piezoelectric transducer network for SHM. Ing *et al.* [78] experimentally performed flaw detection in plates using laser excitation and a multi-element sensor array with a pulse echo time reversal technique. Park *et al.* [79] used a combination of the time reversal approach with the wavelet-based signal processing technique to identify damage in thin composite plates without need of reference signals. Xu *et al.* [80] proposed a theoretical model for the analysis of piezoelectric wafer active sensors-related Lamb wave time reversal based on the exact solutions of the Rayleigh-Lamb wave equations.

1.4 Thesis objectives

The present work aims at the following objectives:

- 1) Construct a new element for simulating the propagation of ultrasonic Lamb waves.
- 2) Study the physical mechanisms behind wave propagation and wave interaction with damage for the interpretation of damage detection or damage evaluation results in ultrasonic Lamb wave-based SHM and NDE approaches.
- 3) Develop a structural damage imaging approach to not only locate damage but also evaluate its shape and size.
- 4) Develop a real-time monitoring technique to detect local plasticity for monitoring defect emergence in advance.

1.5 A preview of the thesis content

The thesis is structured as follows. After the reviewing the current state of SHM and NDE, and the present research purpose, the following five chapters are

presented.

Chapter 2 constructs a versatile pseudospectral Mindlin plate element for the analysis of wave propagation in complex plate-like structures. The new plate element is based on Chebyshev polynomials, and its efficiency and high accuracy are proven by solving wave propagation problems of one dimension (1D) and two dimensions (2D) and comparing its results with those obtained by ABAQUS and experiments.

Chapter 3 uses the pseudospectral Mindlin plate element to build plate and PZT models to systematically investigate the influence of Lamb wave dispersion, the shape of damage, the excitation frequency in wave signals and the incident angle of the Lamb wave on the relative reflection intensity (RRI) from through-thickness elliptically-shaped damage in an aluminum plate. The obtained numerical results show that the dispersion of the Lamb wave has no obvious effect on the RRI, whereas the other parameters mentioned above have a remarkable influence on the RRI from elliptically-shaped damages.

Chapter 4 puts forward a new wave energy flow (WEF) map concept to improve the visualization technique using ultrasonic Lamb wave propagation proposed by Takatsubo *et al.* [81-83]. The improved structural damage imaging approach can not only locate damage but also evaluate the shape and size of damage. In the improved approach, a simple signal processing algorithm is proposed to construct the WEF map when waves propagate through an inspection region, and multiple lead zirconate titanate (PZT) sensors are employed to improve inspection reliability. The effectiveness of the improved approach is verified using aluminum and carbon fiber reinforced plastic laminated plates with

various defects.

Chapter 5 develops a real-time monitoring technique for local plasticity using Lamb waves. To verify the effectiveness of the proposed technique, an experiment methodology by performing tensile test and generation/collection of Lamb waves simultaneously is designed. A thin aluminum plate with a circular hole is used in experiment. The changes of wave amplitudes and a proposed signal index I of S_0 and A_0 modes with the increase of the tensile stress in the plate are observed to analyze the relationship between the changes of the above quantities and the evolution of the local plastic zone.

Chapter 6 summarizes the work reported in this thesis and discusses some ideas and standpoints for future research.

References

- [1] J. Achenbach. Wave propagation in elastic solids. *Elsevier*, 1984.
- [2] I. A. Viktorov. Rayleigh and Lamb waves: physical theory and applications. *Plenum press New York*, 1967.
- [3] A. H. Nayfeh. Wave propagation in layered anisotropic media: With application to composites. *Elsevier*, 1995.
- [4] H. Lamb. On waves in an elastic plate. *Proceedings of the Royal Society of London. Series A, Containing papers of a mathematical and physical character*, 1917, 93:114-128.
- [5] R. Mindlin. Waves and vibrations in isotropic, elastic plates. *Structural Mechanics*, 1960, 199-232.
- [6] D. N. Alleyne and P. Cawley. The interaction of Lamb waves with defects. *IEEE Transactions on Ultrasonics, Ferroelectrics and Frequency Control*, 1992, 39: 381-397.
- [7] N. Guo and P. Cawley. Lamb waves for the NDE of composite laminates.

- Review of Progress in Quantitative Nondestructive Evaluation.* 1992, 11B: 1443-1450.
- [8] F. Degertakin and B. Khuri-Yakub. Lamb wave excitation by Hertzian contacts with applications in NDE. *IEEE Transactions on Ultrasonics, Ferroelectrics and Frequency Control*, 1997, 44: 769-779.
 - [9] M. Castaings and B. Hosten. Lamb and SH waves generated and detected by air-coupled ultrasonic transducers in composite material plates. *NDT & E International*, 2001, 34: 249-258.
 - [10] T. Ghosh, T. Kundu and P. Karpur. Efficient use of Lamb modes for detecting defects in large plates. *Ultrasonics*, 1998, 36: 791-801.
 - [11] Z. Guo, J. Achenbach and S. Krishnaswamy. EMAT generation and laser detection of single lamb wave modes. *Ultrasonics*, 1997, 35: 423-429.
 - [12] J. Achenbach. Quantitative nondestructive evaluation. *International Journal of Solids and Structures*, 2000, 37: 13-27.
 - [13] S. Yoshimura, G. Yagawa, A. Oishi and K. Yamada. Neural network based inverse analysis for defect identification with laser ultrasonics. *Key Engineering Materials*, 1997, 145: 443-452.
 - [14] S. Ishak, G. Liu, H. Shang and S. Lim. Locating and sizing of delamination in composite laminates using computational and experimental methods. *Composites Part B: Engineering*, 2001, 32: 287-298.
 - [15] C. Valle and J. W. Littles Jr. Flaw localization using the reassigned spectrogram on laser-generated and detected Lamb modes. *Ultrasonics*, 2002, 39: 535-542.
 - [16] W. Gao, C. Glorieux and J. Thoen. Laser ultrasonic study of Lamb waves: determination of the thickness and velocities of a thin plate. *International Journal of Engineering Science*, 2003, 41: 219-228.
 - [17] M. Silva, R. Gouyon and F. Lepoutre. Hidden corrosion detection in aircraft aluminum structures using laser ultrasonics and wavelet transform signal analysis. *Ultrasonics*, 2003, 41: 301-305.
 - [18] S. S. Kessler, S. M. Spearing and C. Soutis. Damage detection in composite materials using Lamb wave methods. *Smart Materials and Structures*, 2002,

- II: 269.
- [19] E. Dimitriadis, C. Fuller and C. Rogers. Piezoelectric actuators for distributed vibration excitation of thin plates. *Journal of Vibration and Acoustics*, 1991, 113: 100-107.
 - [20] S. S. Kessler, S. M. Spearing and M. J. Atalla. In-situ damage detection of composites structures using Lamb wave methods. *Proceedings of the First European Workshop on Structural Health Monitoring*, 2002.
 - [21] C. S. Wang and F.-K. Chang. Diagnosis of impact damage in composite structures with built-in piezoelectrics network. *SPIE's 7th Annual International Symposium on Smart Structures and Materials*, 2000.
 - [22] M. Schulz, P. Pai and D. Inman. Health monitoring and active control of composite structures using piezoceramic patches. *Composites Part B: Engineering*, 1999, 30: 713-725.
 - [23] R. Monkhouse, P. Wilcox, M. Lowe, R. Dalton and P. Cawley. The rapid monitoring of structures using interdigital Lamb wave transducers. *Smart Materials and Structures*, 2000, 9: 304.
 - [24] R. Monkhouse, P. Wilcox and P. Cawley. Flexible interdigital PVDF transducers for the generation of Lamb waves in structures. *Ultrasonics*, 1997, 35: 489-498.
 - [25] S. Hurlebaus and L. Gaul. Smart layer for damage diagnostics. *Journal of Intelligent Material Systems and Structures*, 2004, 15: 729-736.
 - [26] G. Pitt, P. Extance, R. Neat, D. Batchelder, R. Jones, J. Barnett and R. Pratt. Optical-fibre sensors. *IEE Proceedings J (Optoelectronics)*, 1985, 132: 214-248.
 - [27] W. Staszewski, G. Pierce, K. Worden and B. Culshaw. Cross-wavelet analysis for Lamb wave damage detection in composite materials using optical fibres. *Key Engineering Materials*, 1999, 167: 373-380.
 - [28] K. Levin. Durability of Embedded Fibre Optic Sensors in Composites. *Institutionen for flygteknik*, 2001.
 - [29] S. Pierce, W. Philp, B. Culshaw, A. Gachagan, A. McNab, G. Hayward and F. Lecuyer. Surface-bonded optical fibre sensors for the inspection of CFRP

- plates using ultrasonic Lamb waves. *Smart Materials and Structures*, 1996, 5: 776.
- [30] S. Pierce, W. Philp, A. Gachagan, A. McNab, G. Hayward and B. Culshaw. Surface-bonded and embedded optical fibers as ultrasonic sensors. *Applied Optics*, 1996, 35: 5191-5197.
- [31] C. Silva, B. Rocha and A. Suleman. PZT Network and Phased Array Lamb Wave Based SHM Systems. *Journal of Physics: Conference Series*, 2011, 305: 012087.
- [32] W. Deutsch, A. Cheng and J. Achenbach. Self-focusing of Rayleigh waves and Lamb waves with a linear phased array. *Journal of Research in Nondestructive Evaluation*, 1997, 9: 81-95.
- [33] S. Sundararaman, D. E. Adams and E. J. Rigas. Structural damage identification in homogeneous and heterogeneous structures using beamforming. *Structural Health Monitoring*, 2005, 4: 171-190.
- [34] V. Giurgiutiu and J. Bao. Embedded-ultrasonics structural radar for in situ structural health monitoring of thin-wall structures. *Structural Health Monitoring*, 2004, 3: 121-140.
- [35] L. Yu and V. Giurgiutiu. In-situ optimized PWAS phased arrays for Lamb wave structural health monitoring. *Journal of Mechanics of Materials and Structures*, 2007, 2: 459-487.
- [36] M. Engholm and T. Stepinski. Adaptive beamforming for array imaging of plate structures using Lamb waves. *IEEE Transactions on Ultrasonics, Ferroelectrics and Frequency Control*, 2010, 57: 2712-2724.
- [37] K. R. Leonard, E. V. Malyarenko and M. K. Hinders. Ultrasonic Lamb wave tomography. *Inverse Problems*, 2002, 18: 1795.
- [38] W. Wright, D. Hutchins, D. Jansen and D. Schindel. Air-coupled Lamb wave tomography. *IEEE Transactions on Ultrasonics, Ferroelectrics and Frequency Control*, 1997, 44: 53-59.
- [39] D. Jansen, D. Hutchins and J. Mottram. Lamb wave tomography of advanced composite laminates containing damage. *Ultrasonics*, 1994, 32: 83-90.

- [40] D. Hutchins, D. Jansen and C. Edwards. Lamb-wave tomography using non-contact transduction. *Ultrasonics*, 1993, 31: 97-103.
- [41] D. Jansen and D. Hutchins. Immersion tomography using Rayleigh and Lamb waves. *Ultrasonics*, 1992, 30: 245-254.
- [42] D. Jansen and D. Hutchins. Lamb wave tomography. *Ultrasonics Symposium, 1990. Proceedings, 1990 IEEE*, 1990, 2: 1017-1020.
- [43] Y. Nagata, J. Huang, J. Achenbach and S. Krishnaswamy. Lamb wave tomography using laser-based ultrasonics. *Springer*, 1995.
- [44] F. L. Degertekin, J. Pei, B. T. Khuri-Yakub and K. C. Saraswat. Insitu acoustic temperature tomography of semiconductor wafers. *Applied Physics Letters*, 1994, 64: 1338-1340.
- [45] M. K. Hinders and J. C. McKeon. Lamb wave tomography for corrosion mapping. *The Second Joint NASA/FAA/DoD Conference on Aging Aircraft*, 1999, 2:732-740.
- [46] M. Hinders, E. Malyarenko and J. McKeon. Contact scanning Lamb wave tomography. *The Journal of the Acoustical Society of America*, 1998, 104: 1790-1791.
- [47] J. C. McKeon and M. K. Hinders. Parallel projection and crosshole Lamb wave contact scanning tomography. *The Journal of the Acoustical Society of America*, 1999, 106: 2568-2577.
- [48] J. C. McKeon and M. K. Hinders. Lamb wave contact scanning tomography. *Springer*, 1999.
- [49] M. K. Hinders, E. V. Malyarenko and J. C. McKeon. Ultrasonic Lamb wave tomographic scanning. *Nondestructive Evaluation of Aging Aircraft, Airports, and Aerospace Hardware III*, 1999, 3586: 279-291.
- [50] B. Hildebrand, T. Davis, G. Posakony and J. Spanner. Lamb Wave Tomography for Imagimg Erosion/Corrosion in Piping. *Springer*, 1999.
- [51] E. V. Malyarenko and M. K. Hinders. Fan beam and double crosshole Lamb wave tomography for mapping flaws in aging aircraft structures. *The Journal of the Acoustical Society of America*, 2000, 108: 1631-1639.

- [52] C. Gershenson. Artificial neural networks for beginners. *Neural and Evolutionary Computing*, 2003.
- [53] P. Tsou and M.-H. Shen. Structural damage detection and identification using neural networks. *AIAA Journal*, 1994, 32: 176-183.
- [54] C.-B. Yun and E. Y. Bahng. Substructural identification using neural networks. *Computers & Structures*, 2000, 77: 41-52.
- [55] Z. Chaudhry and A. Ganino. Damage detection using neural networks: an initial experimental study on debonded beams. *Journal of Intelligent Material Systems and Structures*, 1994, 5: 585-589.
- [56] A. C. Okafor, K. Chandrashekara and Y. Jiang. Delamination prediction in composite beams with built-in piezoelectric devices using modal analysis and neural network. *Smart Materials and Structures*, 1996, 5: 338.
- [57] T. Chang, C. Chang and Y. Xu. Updating structural parameters: an adaptive neural network approach. *Proceedings of the 2nd International Workshop on Structural Health Monitoring*, 1999.
- [58] C. Zang and M. Imregun. Structural damage detection using artificial neural networks and measured FRF data reduced via principal component projection. *Journal of Sound and Vibration*, 2001, 242: 813-827.
- [59] C. Chang, T. Chang, Y. Xu and M. Wang. Structural damage detection using an iterative neural network. *Journal of Intelligent Material Systems and Structures*, 2000, 11: 32-42.
- [60] X. Wu, J. Ghaboussi and J. Garrett Jr. Use of neural networks in detection of structural damage. *Computers & Structures*, 1992, 42: 649-659.
- [61] B. Zu and Z. Wu. Neural-networks-based structural health monitoring strategy with dynamic responses. *Proceedings of the 3rd International Workshop on Structural Health Monitoring*, 2001.
- [62] J. Rhim and S. W. Lee. A neural network approach for damage detection and identification of structures. *Computational Mechanics*, 1995, 16: 437-443.
- [63] H. Chen, G. Qi, J. Yang and F. Amini. Neural network for structural dynamic model identification. *Journal of Engineering Mechanics*, 1995, 121: 1377-1381.

- [64] S. Barai and P. Pandey. Time-delay neural networks in damage detection of railway bridges. *Advances in Engineering Software*, 1997, 28: 1-10.
- [65] C. Hwu and Y. Liang. Hole/crack identification by static strains from multiple loading modes. *AIAA Journal*, 2001, 39: 315-324.
- [66] W. Staszewski, K. Worden, R. Wardle and G. Tomlinson. Fail-safe sensor distributions for impact detection in composite materials. *Smart Materials and Structures*, 2000, 9: 298.
- [67] V. Lopes, G. Park, H. H. Cudney, D. J. Inman and F. Chang. Smart structures health monitoring using artificial neural network. *Structural Health Monitoring 2000*, 1999, 976-985.
- [68] Z. Su, L. Ye and Y. Lu. Guided Lamb waves for identification of damage in composite structures: A review. *Journal of Sound and Vibration*, 2006, 295: 753-780.
- [69] U. Bork. Non-destructive evaluation of adhered metal joints using ultrasonic Lamb waves and artificial neural networks. *NDT & E International*, 1997, 30: 329-329.
- [70] U. Bork and R. Challis. Artificial neural networks applied to Lamb wave testing of T-form adhered joints. *Proceedings of the Conference on the Inspection of Structural Composites, London, UK*, 1994.
- [71] L. Yam, Y. Yan and J. Jiang. Vibration-based damage detection for composite structures using wavelet transform and neural network identification. *Composite Structures*, 2003, 60: 403-412.
- [72] Z. Su and L. Ye. Lamb wave propagation-based damage identification for quasi-isotropic cf/ep composite laminates using artificial neural algorithm: part i-methodology and database development. *Journal of Intelligent Material Systems and Structures*, 2005, 16: 97-111.
- [73] Z. Su and L. Ye. Lamb wave-based quantitative identification of delamination in CF/EP composite structures using artificial neural algorithm. *Composite Structures*, 2004, 66: 627-637.
- [74] Y. Lu, L. Ye, Z. Su, L. Zhang and C. Li. Artificial neural network (ANN)-based crack identification in aluminum plates with Lamb wave

- signals. *Journal of Intelligent Material Systems and Structures*, 2008, doi: 10.1177/1045389X08088782.
- [75] R. Gangadharan,C. Murthy, S. Gopalakrishnan and M. Bhat. Time reversal technique for health monitoring of metallic structure using Lamb waves. *Ultrasonics*, 2009, 49: 696-705.
- [76] M. Fink. Time-reversal acoustics. *Journal of Physics: Conference Series*, 2008, 118: 012001.
- [77] C. H. Wang, J. T. Rose and F.-K. Chang. Computerized time-reversal method for structural health monitoring. *Proc. SPIE 5046, Nondestructive Evaluation and Health Monitoring of Aerospace Materials and Composites II*, 2003, doi:10.1117/12.484668.
- [78] M. Fink. Time recompression of dispersive lamb waves using a Time Reversal mirror-application to flaw detection in thin plates. *Ultrasonics Symposium, 1996. Proceedings, 1996 IEEE*, 1996, 1: 659-663.
- [79] H. W. Park, H. Sohn,K. H. Law and C. R. Farrar. Time reversal active sensing for health monitoring of a composite plate. *Journal of Sound and Vibration*, 2007, 302: 50-66.
- [80] B. Xu and V. Giurgiutiu. Single mode tuning effects on Lamb wave time reversal with piezoelectric wafer active sensors for structural health monitoring. *Journal of Nondestructive Evaluation*, 2007, 26: 123-134.
- [81] J. Takatsubo, B. Wang, H. Tsuda and N. Toyama. Generation laser scanning method for the visualization of ultrasounds propagating on a 3-D object with an arbitrary shape. *Journal of Solid Mechanics and Materials Engineering*, 2007, 1: 1405-1411.
- [82] S. Yashiro, J. Takatsubo and N. Toyama. An NDT technique for composite structures using visualized Lamb-wave propagation. *Composites Science and Technology*, 2007, 67: 3202-3208.
- [83] S. Yashiro, J. Takatsubo, H. Miyauchi and N. Toyama. A novel technique for visualizing ultrasonic waves in general solid media by pulsed laser scan. *NDT & E International*, 2008, 41: 137-144.

Chapter 2

Construction of a pseudospectral Mindlin plate element

2.1 Introduction

Wave propagation phenomena in solids have received a great deal of attention due to their manifestation in various engineering problems, such as SHM and NDE [1-3]. Over the years, many analytical and numerical techniques have been developed for dealing with elastic wave problems. Such methods include: the finite difference method (FDM) [4], the conventional finite element method (FEM) [2, 3, 5-7], and the boundary element method (BEM) [8, 9]. These methods can deal with most complex situations, especially the complex geometry, arbitrary time history of excitation and the non-local properties. However, computational solvability and accuracy based on these approaches deteriorate dramatically, as the spatial domain becomes larger and as the time duration of the excitation becomes shorter. Parallel to the above general approaches, there have been quite remarkable progresses in exact or semi-numerical methods, such as the transfer function matrix method [10], dynamic stiffness matrix method [11], space-time FE method [12], strip element method [13], spectral FE method for beams [14, 15] and Levy-type plate [16] etc.. In general, these methods constructed in the frequency domain need much less memory storage space for necessary data. However, it is very difficult to use them for problems with complex geometries.

Another important approach is a spectral or pseudospectral method in the time domain, which may be firstly proposed by Patera [17], based on trial functions of the Chebyshev series, for the solution of partial differential equations of laminar flow problems. Despite of the terminology, this method in the time domain is completely different from the spectral element methods [14-16] in the

frequency domain. An important advantage of this method is that the numerical errors decrease more quickly than any power of $1/p$, i.e., so-called ‘spectral convergence’, where p is the order of the used polynomial [18]. Similar to Ritz method, where the global structural approximate displacement fields are assumed directly, it is difficult to employ the above approaches for complex structures.

Another approach in this field is based on the variational principle to construct some versatile elements for Mindlin plate problems of complex geometries. The reported methods in this aspect have been very few, e.g., only [19, 20] to the best knowledge of authors. The idea of this pseudospectral element method is very similar to that of FEM except for the specific piecewise interpolation functions within elements as it uses. Sridhar *et al.* [19] used a pseudospectral FEM based on Chebyshev polynomials for wave propagation analysis involving anisotropic materials like composites and inhomogeneous materials like the functionally graded materials. An implicit time integration scheme, i.e., the Newmark method in [19], was used to solve the system equations of motion. Kudela *et al.* [20] developed a pseudospectral Mindlin-plate finite element with 36 nodes defined at Gauss–Lobatto–Legendre points. They constructed the elemental shape functions based on Legendre polynomials and presented numerical results of the propagation of A_0 Lamb mode in a composite plate.

In this chapter, a pseudospectral Mindlin plate element was built up for simulating the propagation of Lamb waves. The Chebyshev polynomials are chosen as the elemental interpolation functions due to their strong suitability for wave modeling. For instance, with the Chebyshev spectral element method for

acoustic wave modeling of Helmholtz equation [21, 22], it has been shown that one only needs a low number of grid points per minimum wavelength (denoted by G) and the high accuracy is preserved even for very long propagation distances. In section 2.2, the new element was described in details, and its efficiency for simulating wave propagation was investigated in section 2.3.

2.2 Description of pseudospectral Mindlin plate element

2.2.1 Shape functions and grid points

We describe the elemental shape functions based on Chebyshev polynomials corresponding to some previous studies [17, 19, 20]. The 2D shape functions defined in the local coordinate system of the element as shown in Figure 2.1, i.e., $\hat{\Omega} = [-1 \leq \xi \leq 1] \times [-1 \leq \eta \leq 1]$ are described as follows:

$$\Phi_I = \psi_i \psi_j \quad (2.1)$$

with

$$\psi_i = \frac{2}{N_\xi} \sum_{m=0}^{N_\xi} \frac{1}{c_i c_m} T_m(\xi_i) T_m(\xi) \quad (2.2a)$$

$$\psi_j = \frac{2}{N_\eta} \sum_{n=0}^{N_\eta} \frac{1}{c_j c_n} T_n(\eta_j) T_n(\eta) \quad (2.2b)$$

where N_ξ and N_η are the orders of Chebyshev polynomials in ξ and η directions, respectively. Therefore, there are $N_\xi+1$ nodes in ξ direction and $N_\eta+1$ nodes in η direction, respectively. And the subscript I in Equation (2.1) representing nodal number is

$$1 \leq I \leq (N_\xi + 1)(N_\eta + 1) \quad (2.3)$$

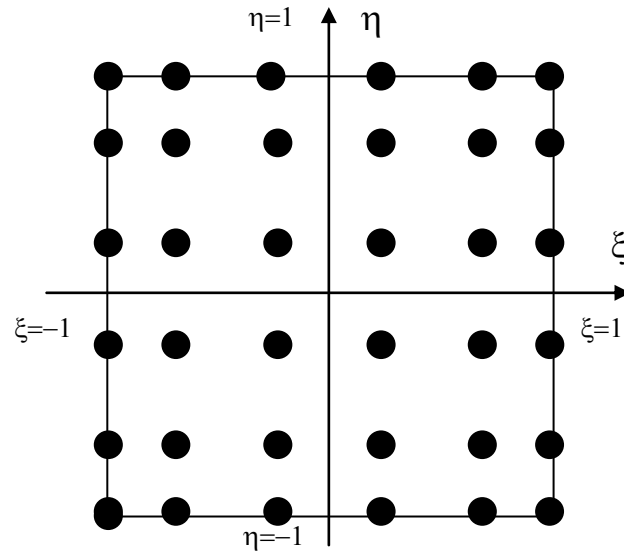


Figure 2.1 A 6×6 spectral plate element

Also, i , j , and c_i in Equations (2.2) are described as

$$0 \leq i \leq N_\xi \quad (2.4a)$$

$$0 \leq j \leq N_\eta \quad (2.4b)$$

$$c_i = \begin{cases} 2 & i = 0, N_\xi \text{ or } N_\eta \\ 1 & 0 < i < N_\xi \text{ or } N_\eta \end{cases} \quad (2.4c)$$

In Equations (2.2), T_j are the Chebyshev polynomials of the first kind. They can be expressed as: $T_j(\cos \theta) = \cos(j\theta)$. Using the mapping: $x = \cos \theta$, the Chebyshev polynomials can be written as: $T_j(x) = \cos(j \cos^{-1} x)$.

The grid points to be used for the spectral plane element are the quadrature points of Chebyshev-Gauss-Lobatto quadrature, which are

$$x_i = -\cos \frac{\pi i}{N}, 0 \leq i \leq N_\xi \text{ or } N_\eta \quad (2.5)$$

Taking the 6×6 pseudospectral plate element as an example, there are 6 nodes both in ξ direction and in η direction. It can be seen from Figure 2.1 that the

distribution of the grid points is irregular which is different from that of conventional FEM whose elemental nodes are uniformly spaced within elements.

Therefore, the Cartesian coordinate of arbitrary points in elements can be expanded as:

$$x = \sum_{I=1}^{(N_\xi+1)(N_\eta+1)} \Phi_I x_I = \sum_{i=0}^{N_\xi} \sum_{j=0}^{N_\eta} \psi_i \psi_j x_{i \times (N_\eta+1) + (j+1)} \quad (2.6a)$$

$$y = \sum_{I=1}^{(N_\xi+1)(N_\eta+1)} \Phi_I y_I = \sum_{i=0}^{N_\xi} \sum_{j=0}^{N_\eta} \psi_i \psi_j y_{i \times (N_\eta+1) + (j+1)} \quad (2.6b)$$

where $x_{i \times (N_\eta+1) + (j+1)}$ and $y_{i \times (N_\eta+1) + (j+1)}$ represent the x and y coordinates of the grid point numbered as $i \times (N_\eta+1) + (j+1)$ within the element.

2.2.2 Theory of pseudospectral plate element and integration scheme

In this section, we briefly introduce the theory of the present pseudospectral plane element, which is identical to that used in conventional FEM for Mindlin plate. In this research, to extend the present element into more complex cases in future, e.g., asymmetric stacking sequence of composite laminates, we consider five degree of freedoms at one node, which are u_0, v_0, w_0, θ_x , and θ_y . The displacement fields of plate can be expressed as follows:

$$u(x, y, z) = u_0 - z\theta_x \quad (2.7a)$$

$$v(x, y, z) = v_0 - z\theta_y \quad (2.7b)$$

$$w(x, y) = w_0 \quad (2.7c)$$

where u_0, v_0 and w_0 are the translation displacements on the neutral plane of plate along x, y and z directions, and θ_x and θ_y the rotations about the y and x axes,

respectively.

By using the interpolation functions in Equation (2.1), the displacement components can be expressed as

$$u_0 = \sum_{I=1}^{(N_\xi+1)(N_\eta+1)} \Phi_I u_I^0 \quad (2.8a)$$

$$v_0 = \sum_{I=1}^{(N_\xi+1)(N_\eta+1)} \Phi_I v_I^0 \quad (2.8b)$$

$$w = \sum_{I=1}^{(N_\xi+1)(N_\eta+1)} \Phi_I w_I \quad (2.8c)$$

$$\theta_x = \sum_{I=1}^{(N_\xi+1)(N_\eta+1)} \Phi_I \theta_I^x \quad (2.8d)$$

$$\theta_y = \sum_{I=1}^{(N_\xi+1)(N_\eta+1)} \Phi_I \theta_I^y \quad (2.8e)$$

Then, the generalized strains associated with the above displacements can be described as follows:

$$\boldsymbol{\epsilon} = \begin{Bmatrix} \epsilon_x^0 \\ \epsilon_y^0 \\ \gamma_{xy}^0 \\ \kappa_x \\ \kappa_y \\ \kappa_{xy} \\ \gamma_{xz} \\ \gamma_{yz} \end{Bmatrix} = \begin{Bmatrix} \frac{\partial u_0}{\partial x} \\ \frac{\partial v_0}{\partial y} \\ \frac{\partial v_0}{\partial x} + \frac{\partial u_0}{\partial y} \\ -\frac{\partial \theta_x}{\partial x} \\ -\frac{\partial \theta_y}{\partial y} \\ -\left(\frac{\partial \theta_y}{\partial x} + \frac{\partial \theta_x}{\partial y}\right) \\ \frac{\partial w}{\partial x} - \theta_x \\ \frac{\partial w}{\partial y} - \theta_y \end{Bmatrix} = \sum_{I=1}^{(N_\xi+1)(N_\eta+1)} \mathbf{B}_I \mathbf{d}_I \quad (2.9)$$

where $\varepsilon_x^0, \varepsilon_y^0$ and γ_{xy}^0 are strains at the neutral plane, κ_x and κ_y bending curvatures, κ_{xy} twisting curvature, and γ_{xz} and γ_{yz} are transverse shear strains, respectively.

The nodal strain-displacement matrix \mathbf{B}_I and nodal displacement vector \mathbf{d}_I corresponding to the node I are described as

$$\mathbf{B}_I = \begin{bmatrix} \frac{\partial \Phi_I}{\partial x} & 0 & 0 & 0 & 0 \\ 0 & \frac{\partial \Phi_I}{\partial y} & 0 & 0 & 0 \\ \frac{\partial \Phi_I}{\partial y} & \frac{\partial \Phi_I}{\partial x} & 0 & 0 & 0 \\ 0 & 0 & 0 & -\frac{\partial \Phi_I}{\partial x} & 0 \\ 0 & 0 & 0 & 0 & -\frac{\partial \Phi_I}{\partial y} \\ 0 & 0 & 0 & -\frac{\partial \Phi_I}{\partial y} & -\frac{\partial \Phi_I}{\partial x} \\ 0 & 0 & \frac{\partial \Phi_I}{\partial x} & -\Phi_I & 0 \\ 0 & 0 & \frac{\partial \Phi_I}{\partial y} & 0 & -\Phi_I \end{bmatrix} \text{ and } \mathbf{d}_I = \begin{bmatrix} u_I^0 \\ v_I^0 \\ w_I \\ \theta_I^x \\ \theta_I^y \end{bmatrix} \quad (2.10)$$

The generalized force associated with the generalized strains in Equation (2.9) can be described as follows:

$$\boldsymbol{\sigma} = \begin{bmatrix} [N] \\ [M] \\ [Q] \end{bmatrix} = \begin{bmatrix} N_x \\ N_y \\ N_{xy} \\ M_x \\ M_y \\ M_{xy} \\ Q_x \\ Q_y \end{bmatrix} \quad (2.11)$$

where N_x, N_y, N_{xy}, Q_x and Q_y are resultant forces of the plate, and M_x, M_y and M_{xy} are resultant moments of plate.

Moreover, the generalized material matrix can be described as follows:

$$\begin{Bmatrix} N_x \\ N_y \\ N_{xy} \\ M_x \\ M_y \\ M_{xy} \\ Q_x \\ Q_y \end{Bmatrix} = \begin{bmatrix} [A] & [B] & [0] \\ [B] & [D] & [0] \\ [0] & [0] & [Q_s] \end{bmatrix} \begin{Bmatrix} \varepsilon_x^0 \\ \varepsilon_y^0 \\ \gamma_{xy}^0 \\ K_x \\ K_y \\ K_{xy} \\ \gamma_{xz} \\ \gamma_{yz} \end{Bmatrix} = \mathbf{D} \begin{Bmatrix} \varepsilon_x^0 \\ \varepsilon_y^0 \\ \gamma_{xy}^0 \\ K_x \\ K_y \\ K_{xy} \\ \gamma_{xz} \\ \gamma_{yz} \end{Bmatrix} \quad (2.12)$$

where $[A]$, $[B]$ and $[D]$ are the in-plane stiffness, coupling stiffness and bending stiffness matrix of plate, respectively, and $[Q_s]$ is the shear stiffness matrix of plate.

From Equations (2.9) and (2.10), the elemental strain-displacement matrix and the elemental displacement vector can be expressed as

$$\mathbf{B} = [\mathbf{B}_1 \dots \mathbf{B}_I \dots \mathbf{B}_{(N_\xi+1)(N_\eta+1)}] \text{ and } \mathbf{d} = \left\{ \begin{array}{c} \mathbf{d}_1 \\ \vdots \\ \mathbf{d}_I \\ \vdots \\ \mathbf{d}_{(N_\xi+1)(N_\eta+1)} \end{array} \right\} \quad (2.13)$$

For the elemental stiffness matrix as shown in the following,

$$\mathbf{K} = \begin{bmatrix} \mathbf{K}_{11} & \mathbf{K}_{12} & \cdots & \cdots & \mathbf{K}_{1[(N_\xi+1)(N_\eta+1)]} \\ & \mathbf{K}_{22} & \cdots & \cdots & \mathbf{K}_{2[(N_\xi+1)(N_\eta+1)]} \\ & & \mathbf{K}_{II} & \dots\dots & \mathbf{K}_{I[(N_\xi+1)(N_\eta+1)]} \\ & symmetric & & \mathbf{K}_{[(N_\xi+1)(N_\eta+1)-1][(N_\xi+1)(N_\eta+1)-1]} & \mathbf{K}_{[(N_\xi+1)(N_\eta+1)-1][(N_\xi+1)(N_\eta+1)]} \\ & & & & \mathbf{K}_{[(N_\xi+1)(N_\eta+1)][(N_\xi+1)(N_\eta+1)]} \end{bmatrix}$$

the elemental stiffness sub-matrix can be calculated as

$$\mathbf{K}_{IJ} = \int_{-1}^{+1} \int_{-1}^{+1} \mathbf{B}_I^T \mathbf{D} \mathbf{B}_J \det \mathbf{J}^e d\xi d\eta = \sum_{p=1}^{N_\xi+1} \sum_{q=1}^{N_\eta+1} (\mathbf{B}_I^T \mathbf{D} \mathbf{B}_J \det \mathbf{J}^e)_{(\xi_p, \eta_q)} W_p W_q \quad (2.15)$$

where ξ_p and η_q are the coordinates of integration points, W_p and W_q are the weights, and \mathbf{J}^e is the Jacobian of element, which is evaluated by using the global coordinates of all nodes in the element, and derivatives of $\frac{\partial \Phi_I}{\partial \xi}$ and $\frac{\partial \Phi_I}{\partial \eta}$.

In this research, an uncommon integration scheme, i.e., Chebyshev points quadrature (CPQ), which uses the positions of the grid points as the quadrature points, is employed to obtain the stiffness matrix. For CPQ, its weight functions need to be solved since it is not routine integration scheme. This numerical integration method is based on interpolation, e.g., Lagrange interpolation or Newton's forward interpolation etc. Here, the weight functions at the interpolation points can be obtained from Lagrange interpolation polynomials and described as:

$$W_j = \int_a^b h_j(x) dx, \text{ with } h_j(x) = \frac{\prod_{i \neq j} (x - x_i)}{\prod_{i \neq j} (x_j - x_i)} \quad (2.16)$$

From the previous descriptions, e.g., Equation (2.1), we know that $a=-1$ and $b=1$, and x_i and x_j are local coordinates of grid points that can be easily calculated from Equation (2.5). Therefore, it is easy to get the weight functions of CPQ by using Equation (2.16). Usually, the algebraic accuracy of this integration is only of the order of $n-1$ for n integration points, which is lower than that of Gaussian type integration methods, e.g., $2n-1$ for Guass-Legendre quadrature, and $2n-3$ for Guass-Lobatto quadrature. However, it is sufficient to integrate a Chebyshev polynomial of the order of $n-1$ when n grid points (or n integration points) are used.

By using CPQ, a lumped elemental mass matrix is obtained. It is crucial to reduce numerical operations for being able to use the central difference method. Since the present element is a high-order element, It means that a larger size of the element can be used compared with the common finite elements, which directly results in a larger available time step. It is undoubted that the computational time will be decreased. The elemental mass matrix can be expressed as follows:

$$\mathbf{M} = \begin{bmatrix} \mathbf{M}_{11} & \cdots & 0 & \cdots & 0 \\ & \ddots & \vdots & & \vdots \\ & & \mathbf{M}_{II} & \cdots & 0 \\ & & & \ddots & \vdots \\ & & & & \mathbf{M}_{[(N_\zeta+1)(N_\eta+1)][(N_\zeta+1)(N_\eta+1)]} \end{bmatrix} \quad (2.17)$$

The sub-matrix in the above matrix can be described as

$$\mathbf{M}_{II} = \int_{-1}^{+1} \int_{-1}^{+1} \mathbf{N}_I^T \Delta \mathbf{N}_J \det \mathbf{J}^e d\xi d\eta = \sum_{p=1}^{N_\zeta+1} \sum_{q=1}^{N_\eta+1} (\mathbf{N}_I^T \Delta \mathbf{N}_J \det \mathbf{J}^e)_{(\xi_p, \eta_q)} W_p W_q \quad (2.18)$$

For five degree of freedoms, the matrix of shape function with dimension of 5×5 can be expressed as

$$\mathbf{N}_I = [\Phi_I \quad \Phi_I \quad \Phi_I \quad \Phi_I \quad \Phi_I] \quad (2.19)$$

For the different degree of freedoms, the matrix of Δ has the different components, which can be expressed as follows

$$\Delta = \begin{bmatrix} \rho t & 0 & 0 & 0 & 0 \\ 0 & \rho t & 0 & 0 & 0 \\ 0 & 0 & \rho t & 0 & 0 \\ 0 & 0 & 0 & \lambda & 0 \\ 0 & 0 & 0 & 0 & \lambda \end{bmatrix} \quad (2.20)$$

where the first three components, i.e., ρt , relate to three translational degree of freedoms, u_0 , v_0 and w , respectively, for the plate thickness of t . λ relates to the rotational degree of freedoms, i.e., θ_x and θ_y , which can be described as

follows by referring to the work [23]

$$\lambda = \rho t \text{Max} \left\{ t^2 / 12, V / (8t) \right\} \quad (2.21)$$

where V is the elemental volume.

2.3 Effectiveness of pseudospectral Mindlin plate element

2.3.1 A 1D wave propagation problem

To verify the effectiveness of the present plate element for simulating the wave propagation in a moderately thick beam or plate, i.e., 5 mm thickness, the commercial ABAQUS software is employed for comparison. The waveform of input signal is described as follows:

$$P(t) = \begin{cases} 0.5[1 - \cos(2\pi ft/N)] \cos(2\pi ft), & t \leq N/f \\ 0, & t > N/f \end{cases} \quad (2.22)$$

where f is the central frequency in Hz and N is the number of sinusoidal cycles within a pulse, i.e., cycle number. In this section, N is equal to 5. As noted in [24], considering those practical experiences, five cycles in signal is the best choice, and this cycle number will be constantly used in the following contents.

A long aluminum beam with the length of 600 mm, the thickness of 5 mm, and the width of 10 mm is used. The material properties of aluminum are listed in Table 1.1. At one end of the mid-plane of the beam, the line-distributed loads of total $1.0 N$ are applied with the form of Equation (2.22) (see Figure 2.2), and the other end of the beam is fixed. To avoid the influence of two free side surfaces of the beam, zero displacements in the width direction are applied to all nodes. The signal frequency is set as 50 kHz, 100 kHz and 200 kHz, respectively. In the computations of ABAQUS, 8-noded 3D linear brick elements are used. As shown

in Figure 2.2, 10 divisions are used along the thickness and the width directions, respectively. Along the length direction, the elemental size is 1 mm. There are at least over ten elements within a wavelength by noting that the shortest wavelength is around 10.0 mm for 200 kHz. For the present Mindlin plate element, two divisions are used in the width direction, and along the length direction, the elemental size is 5 mm. In fact, a mesh size of 2.5 mm in the length direction yields the same result which guarantees the convergence. The wave signals at the two points, located at 50 mm and 100 mm from the loading point, which are defined as “Point 1” and “Point 2”, respectively, are used for comparison. The comparisons between the two kinds of results are shown in Figure 2.3 for the three frequencies. It can be found that the present results agree with those of ABAQUS very well. In Figure 2.3(c), for 200 kHz, there are some noises after the first wave packet in both results of the present method and ABAQUS, which may be caused by the two free side surfaces in the width direction of the beam.

2.3.2 A 2D wave propagation problem

To further verify the proposed plate element for 2D plate problems, an aluminum plate of the thickness of 5 mm, which contains a hole of diameter of 2 cm, is employed as shown in Figure 2.4(a). A technique for visualizing ultrasound wave propagation in Reference [24] is adopted. As shown in Figure 2.4(a), this technique uses a pulsed laser as actuator that scans the test piece for ultrasound wave generation and a fixed acoustic emission (AE) sensor as receiver. The received signals of sensor are stored in a computer by way of an amplifier and a digital oscilloscope. Waveforms are collected at grid points within a given

scanning area where the pulsed laser is used to excite ultrasound waves as shown in Figure 2.4(a). By using the assumption of reversible wave propagation, as shown in Figure 2.4(b), the collected waveform data can be transformed into a set of data which denotes the wave propagation where the sensor works as an actuator and the grid points work as sensors virtually. Here, in numerical simulations, we use a circular piezoelectric actuator, which is attached at the position of the AE sensor in Figure 2.4(b) on the surface of the plate, to simulate the working condition of the pulsed laser. The diameter and thickness of the virtual piezoelectric actuator is 10 and 0.5 mm, respectively. The material properties of this piezoelectric actuator are shown in Table 2.1. The excitation signal of the pulsed laser cannot be obtained directly. Here, the response of the AE sensor, which is located very near a point irradiated by the pulsed laser, is used. This experimental signal is shown in Figure 2.5. The central frequency of this signal is around 170 kHz. In numerical simulations, the input voltage signal of the piezoelectric actuator is taken from the experimental data before 0.0001 s as shown in Figure 2.5. The largest element size using CPQ in this analysis is taken as 5 mm, which is smaller than the half wave length of S_0 and A_0 wave modes at 170 kHz. Of course, near the hole, the mesh size is adjusted to be smaller. The experimental wave propagation visualization at $t = 45 \mu\text{s}$ is demonstrated in Figure 2.6(a), from which S_0 and A_0 wave modes can be identified clearly. Our numerical simulated results also contain S_0 and A_0 wave modes, which implies that it is suitable to employ the piezoelectric actuator attached on the surface of the plate to model the working condition of the pulsed laser. Both experimental and numerical wave scattering visualizations for A_0 wave mode at $t=71.35 \mu\text{s}$ are

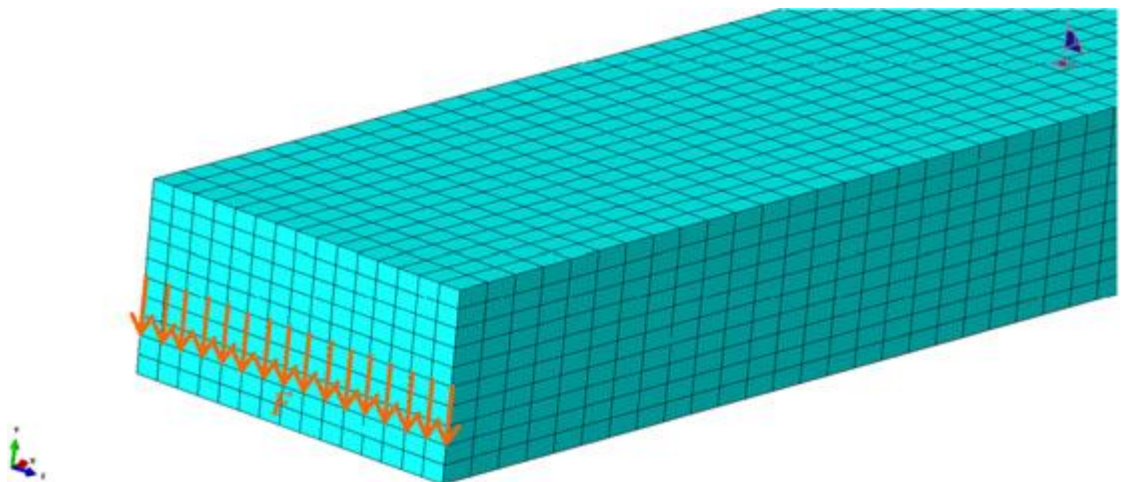
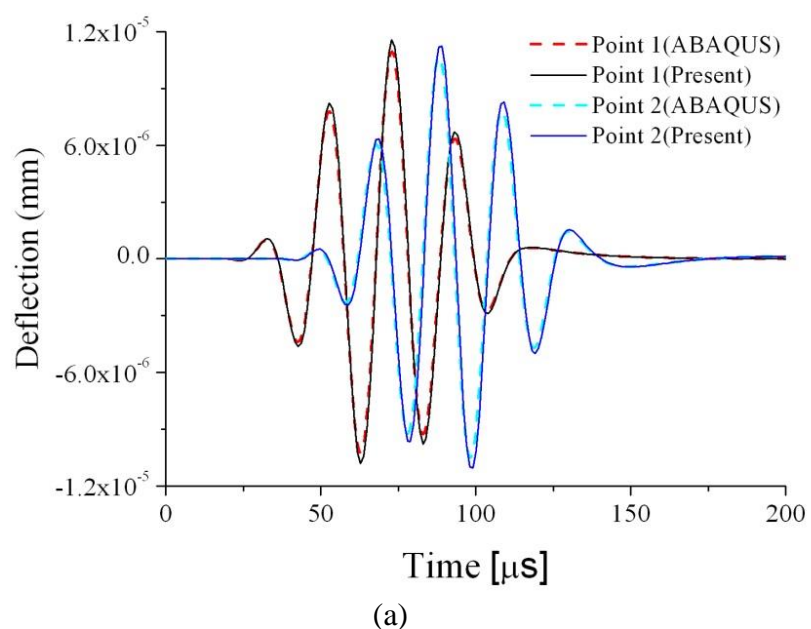


Figure 2.2 Mesh and loads for computation of ABAQUS



(a)

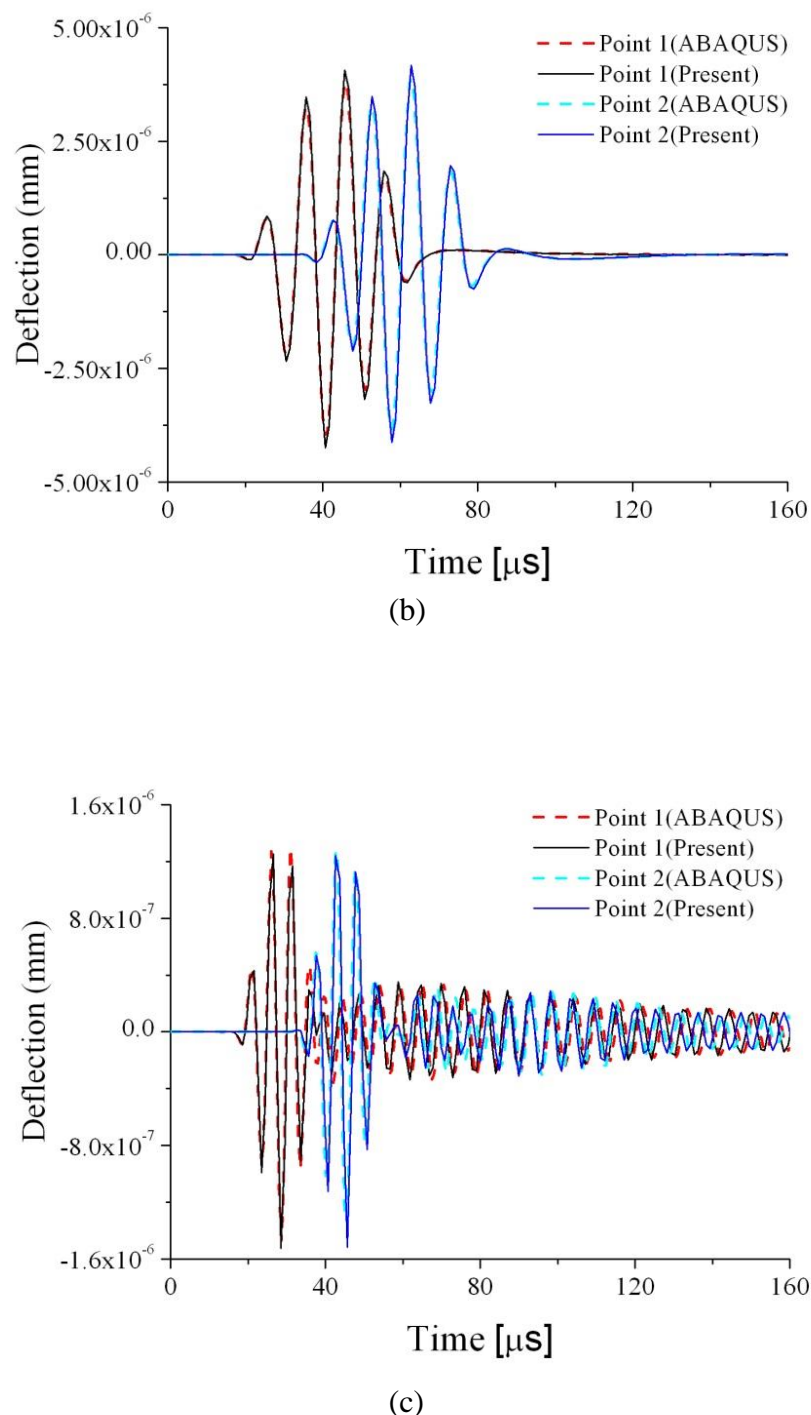
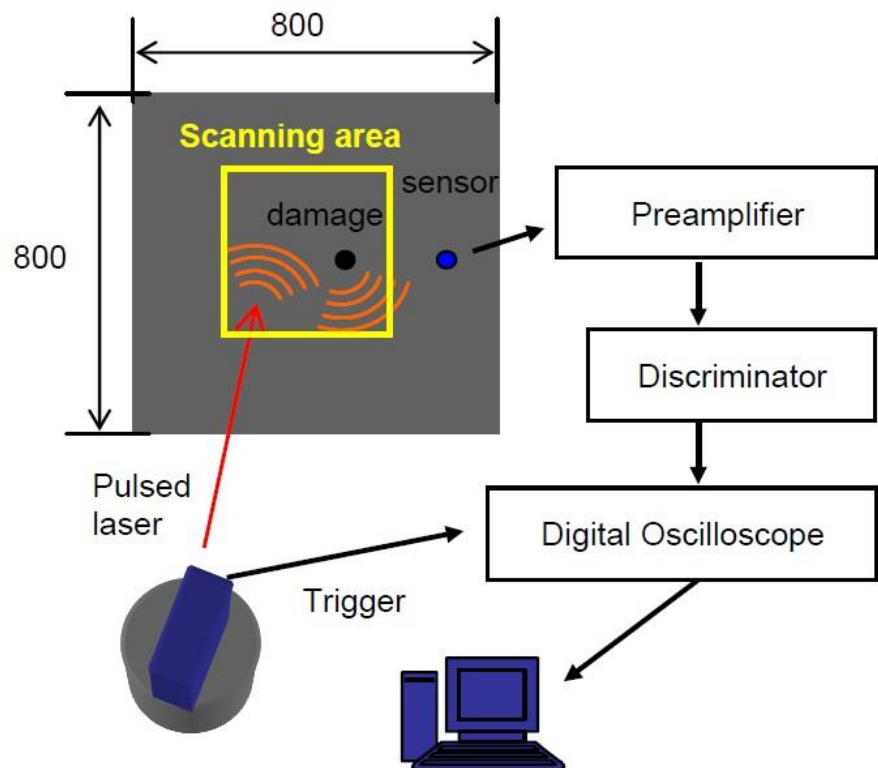
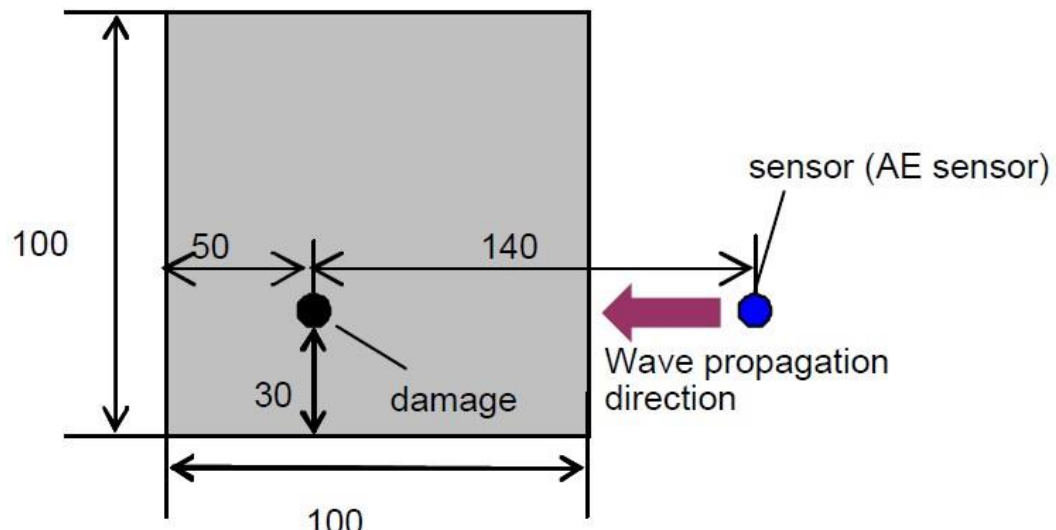


Figure 2.3 Comparison between the present numerical method and ABAQUS: (a) 50 kHz; (b) 100 kHz; (c) 200 kHz



(a)



(b)

Figure 2. 4 Visualization system of wave propagation in an aluminum plate with a hole of diameter of 2 cm: (a) experimental setup for wave propagation visualization (length unit: mm); (b) enlarged scanning area (length unit: mm)
(50×50 grids with 2 mm step size)

Table 2.1 Material properties of piezoelectric actuator

Young's Modullus [GPa]	62
Piezoelectric Coefficient [pC/N]	$d_{33} = 472 \ d_{31} = -210 \ d_{15} = 758$

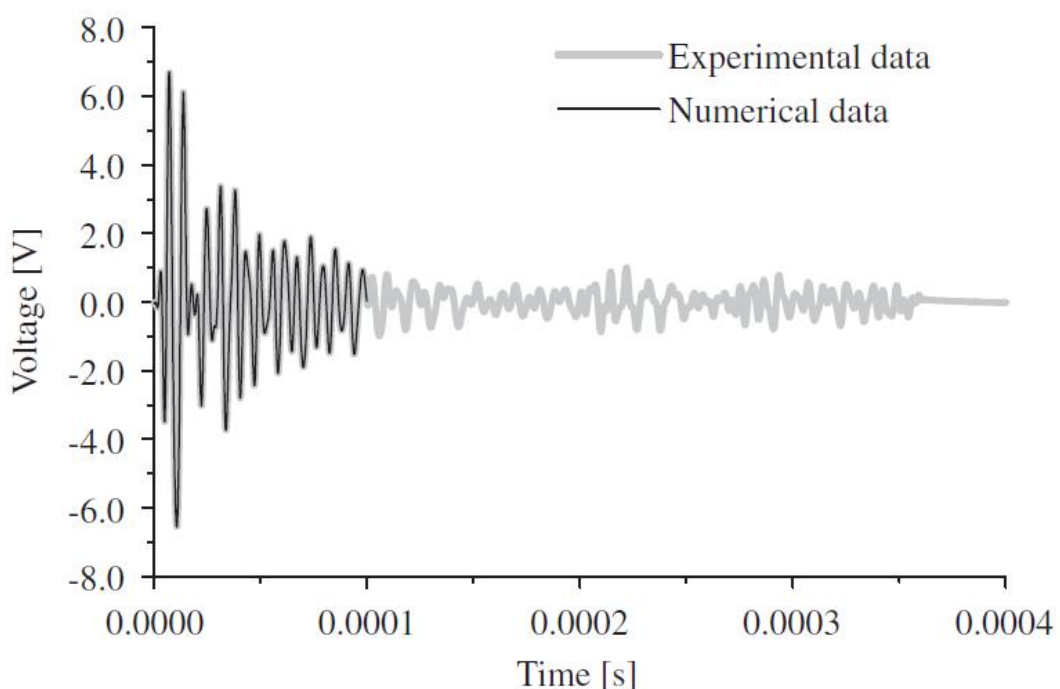


Figure 2. 5 Input signal for simulating the excitation force

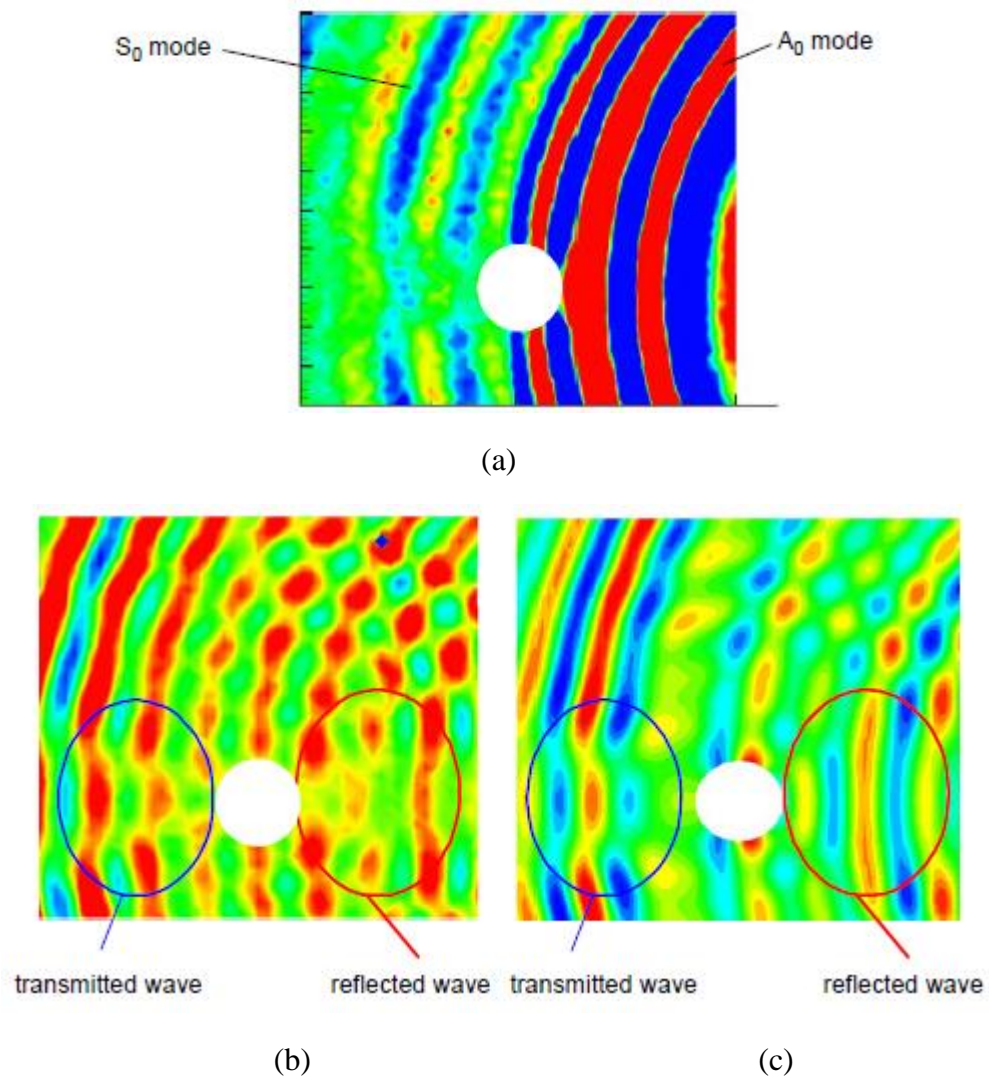


Figure 2. 6 Comparison of wave propagation results: (a) experimental ($t = 45 \mu\text{s}$);
(b) experimental ($t = 71.35 \mu\text{s}$); (c) numerical ($t = 71.35 \mu\text{s}$)

shown in Figures 2.6(b) and (c). From these figures, we can find that the numerical result agrees with the experimental one very well if we compare the transmitted waves and reflected waves near the hole in two figures. This experimental example further validates the effectiveness of the proposed numerical approach for 2D complex problems. Moreover, the computational cost using this new approach is much lower than that of traditional FEM elements.

2.4 Conclusion

A pseudospectral Mindlin plate element is proposed for simulating the propagation of ultrasonic Lamb waves. Chebyshev polynomials are used as base functions and Chebyshev-Gauss-Lobatto points are used as grid points of the new Mindlin plate element. An untraditional numerical integration scheme, i.e., Chebyshev points quadrature (CPQ), is suggested by us to form the elemental mass matrix and stiffness matrix. A lumped elemental mass matrix is generated due to the discrete orthogonality of Chebyshev polynomials and overlapping of the quadrature points with the grid points. This element possesses the high accuracy of spectral method and the flexibility of the conventional finite element method. Wave propagation problems of 1D and 2D are presented to demonstrate the efficiency of the present pseudospectral Mindlin plate element by comparing with the results of ABAQUS and experiments.

References

- [1] T. Ghosh, T. Kundu and P. Karpur. Efficient use of Lamb modes for detecting defects in large plates. *Ultrasonics*, 1998, 36: 791-801.
- [2] N. Hu, T. Shimomukai, C. Yan and H. Fukunaga. Identification of

- delamination position in cross-ply laminated composite beams using S₀ Lamb mode. *Composites Science and Technology*, 2008, 68: 1548-1554.
- [3] N. Hu, T. Shimomukai, H. Fukunaga and Z. Su. Damage identification of metallic structures using A0 mode of Lamb waves. *Structural Health Monitoring*, 2008, 7: 271-285.
 - [4] J. C. Strikwerda. Finite difference schemes and partial differential equations. *Siam*, 2004.
 - [5] O. C. Zienkiewicz and R. L. Taylor. The finite element method: Solid mechanics. *Butterworth-heinemann*, 2000.
 - [6] M. Koshiba, S. Karakida and M. Suzuki. Finite-element analysis of Lamb wave scattering in an elastic plate waveguide. *IEEE Transactions on Sonics and Ultrasonics*, 1984, 31: 18-25.
 - [7] D. N. Alleyne and P. Cawley. Optimization of Lamb wave inspection techniques. *NDT & E International*, 1992, 25: 11-22.
 - [8] Y. Cho and J. L. Rose. A boundary element solution for a mode conversion study on the edge reflection of Lamb waves. *The Journal of the Acoustical Society of America*, 1996, 99: 2097-2109.
 - [9] Y.-H. Pao,D.-C. Keh and S. M. Howard. Dynamic response and wave propagation in plane trusses and frames. *AIAA Journal*, 1999, 37: 594-603.
 - [10] J. Bannerjee and F. Williams. Exact dynamic stiffness matrix for composite Timoshenko beams with applications. *Journal of Sound and Vibration*, 1996, 194: 573-585.
 - [11] L.-J. Hou and D. Peters. Application of triangular space-time finite elements to problems of wave propagation. *Journal of Sound and Vibration*, 1994, 173: 611-632.
 - [12] G. Liu and J. Achenbach. A strip element method for stress analysis of anisotropic linearly elastic solids. *Journal of Applied Mechanics*, 1994, 61: 270-277.
 - [13] J. F. Doyle. Wave Propagation in Structures: Spectral Analysis Using Fast Discrete Fourier Transform. *Mechanical Engineering Series*, 1997.

- [14] D. Roy Mahapatra and S. Gopalakrishnan. A spectral finite element model for analysis of axial–flexural–shear coupled wave propagation in laminated composite beams. *Composite Structures*, 2003, 59: 67-88.
- [15] U. Lee and J. Lee. Spectral-element method for Levy-type plates subject to dynamic loads. *Journal of Engineering Mechanics*, 1999, 125: 243-247.
- [16] A. T. Patera. A spectral element method for fluid dynamics: laminar flow in a channel expansion. *Journal of Computational Physics*, 1984, 54: 468-488.
- [17] C. Pozrikidis. Introduction to finite and spectral element methods using MATLAB. *CRC Press*, 2005.
- [18] R. Sridhar, A. Chakraborty and S. Gopalakrishnan. Wave propagation analysis in anisotropic and inhomogeneous uncracked and cracked structures using pseudospectral finite element method. *International Journal of Solids and Structures*, 2006, 43: 4997-5031.
- [19] P. Kudela, A. Zak, M. Krawczuk and W. Ostachowicz. Modelling of wave propagation in composite plates using the time domain spectral element method. *Journal of Sound and Vibration*, 2007, 302: 728-745.
- [20] G. Seriani and E. Priolo. Spectral element method for acoustic wave simulation in heterogeneous media. *Finite Elements in Analysis and Design*, 1994, 16: 337-348.
- [21] G. Seriani. Double-grid Chebyshev spectral elements for acoustic wave modeling. *Wave Motion*, 2004, 39: 351-360.
- [22] T. J. Hughes. The finite element method: linear static and dynamic finite element analysis. *Courier Dover Publications*, 2012.
- [23] Z. Su, L. Ye and Y. Lu. Guided Lamb waves for identification of damage in composite structures: A review. *Journal of Sound and Vibration*, 2006, 295: 753-780.
- [24] N. Hu, H. Fukunaga, M. Kameyama, D. R. Mahapatra and S. Gopalakrishnan. Analysis of wave propagation in beams with transverse and lateral cracks using a weakly formulated spectral method. *Journal of Applied Mechanics*, 2007, 74: 119-127.

Chapter 3

**Study on the interaction of ultrasonic Lamb waves with
elliptically-shaped damages in metallic plates**

3.1 Introduction

The interpretation of damage detection or damage evaluation results in ultrasonic Lamb wave-based SHM can become easier when the physical mechanisms behind wave propagation and wave interaction with damage are well understood. Therefore, as summarized in [1], a lot of research works on wave interaction with damage have been done for this purpose. Most studies are related to wave scattering problems using classical, analytical and numerical approaches. In metallic structures, for cracks or surface defects, some examples in one-dimensional problems include elastic wave interactions, with various crack configurations using the mass-spring lattice model approach [2], with an inclined crack [3] using a T-matrix and boundary element hybrid method, with various surface breaking defects [4] using elastodynamic hybrid boundary elements or a combined FE and modal expansion method [5], and with various surface cracks using a weakly formulated spectral method [6]. For damages in two-dimensional metallic plates, there have also been some examples, such as wave interaction with a crack in plates using the FE analysis [7-10] and the local interaction simulation approach [11]. Most of these studies concerned the interaction of S_0 wave mode with the crack [8-10] although both A_0 and S_0 modes were also modeled in some works, e.g., [11]. For a circular hole or a rectangular slot in metallic plates, there have also been a few studies [7, 10-15]. For composite beam or plates, some studies of Lamb wave interactions with a hole [16, 17] and delamination [18-21] were reported. The above studies have shown the interaction of Lamb waves with various damages in various materials is indeed difficult and needs further investigations. Moreover, all of the above studies have been limited

to one or two special damage cases, and there are several issues which have not been systematically addressed, e.g., the influences of damage geometry, wave incident direction, and signal parameters on the interaction phenomenon.

In order to enhance the reliability and sensitivity of the application techniques used in ultrasonic Lamb wave-based SHM and NDE, compared with the intensity of incident wave, it is expected to collect the strongest intensity of reflected waves (or the weakest intensity of transmitted waves) at damage from sensors. In this work, we focus on the relative reflection intensity (RRI) of Lamb waves from an arbitrary through-thickness elliptical hole in metallic plates, which can be transformed into a crack-like hole or a circular hole freely. Here, RRI is defined as: the ratio of the intensity of the reflected wave from damage to that of the incident wave received by the same sensor, which is located away from the damage with a certain distance. The influences of the damage shape, wave incident angle and the signal central frequency on RRI are explored comprehensively. To carry out these investigations, a pseudospectral Mindlin plate element proposed in the chapter 2 is used. In this study, A_0 Lamb wave mode is used although the obtained conclusions in this work are also applicable to S_0 mode. Since the Lamb waves are dispersive depending on the frequency range, it is important to confirm whether the dispersion of Lamb waves has the significant influence on RRI from damage. Hence, this problem is explored firstly in section 3.2. In section 3.3, the effects of damage shape, incident angle and wave central frequency on RRI are studied in detail. The obtained results can be helpful to comprehensively understand the complex interactions of Lamb waves with various damages, and to improve the reliability and sensitivity of the techniques

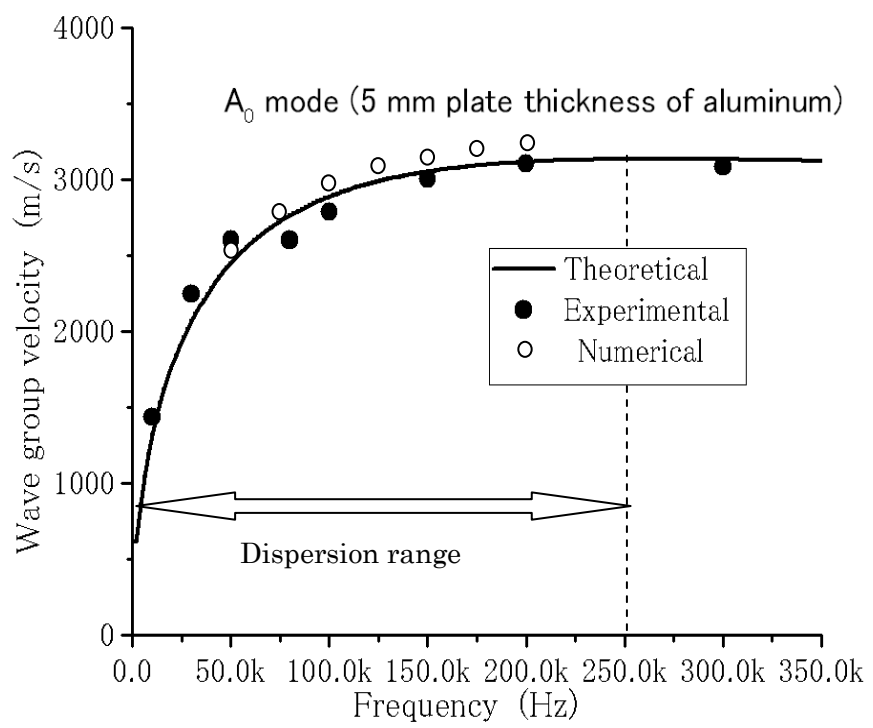
using Lamb waves by designing suitable actuator/sensor placements and input wave signals.

3.2 Influence of Lamb wave dispersion on RRI from damage

With a dispersive frequency domain, the wave phase or group velocity of the Lamb wave varies as the wave frequency changes. In Figure 3.1, the group and phase velocities, and the wavelength of the A_0 mode in an aluminum plate of 5 mm thickness are plotted. The theoretical results are obtained from the Rayleigh-Lamb equation [22]. The experimental data for the group velocity from the reference [7] are directly adopted, and the numerical data in Figure 3.1 will be explained later. From Figures 3.1(a) and (b), the approximate dispersion range of the A_0 mode in this plate is from 0 to 250 kHz. When the Lamb wave propagates in this region, the wave packet with highly concentrated wave energy is gradually broadened, and therefore the energy density per unit area becomes smaller. This dispersion causes the decrease of the wave amplitude during its propagation. In this section, before the exploration of the RRI from damage, it is necessary to confirm whether this RRI is affected by the dispersion of the Lamb wave since the sensor is distant from the damage. If the RRI received at the sensor is affected by dispersion due to wave propagation on the forward/backward paths between the sensor and the damage, it is difficult to evaluate the influence of other parameters on the RRI.

Table 3.1 Material properties of PZT and aluminum

Material properties	
PZT	$E_{11}=62 \text{ GPa}$, $E_{33}=49 \text{ GPa}$, $d_{33}=472 \text{ pC/N}$, $d_{31}=-210 \text{ pC/N}$, $\rho=7500 \text{ kg/m}^3$
Aluminum	$E=68.9 \text{ GPa}$, $\nu=0.3$, $\rho=2710 \text{ kg/m}^3$



(a)

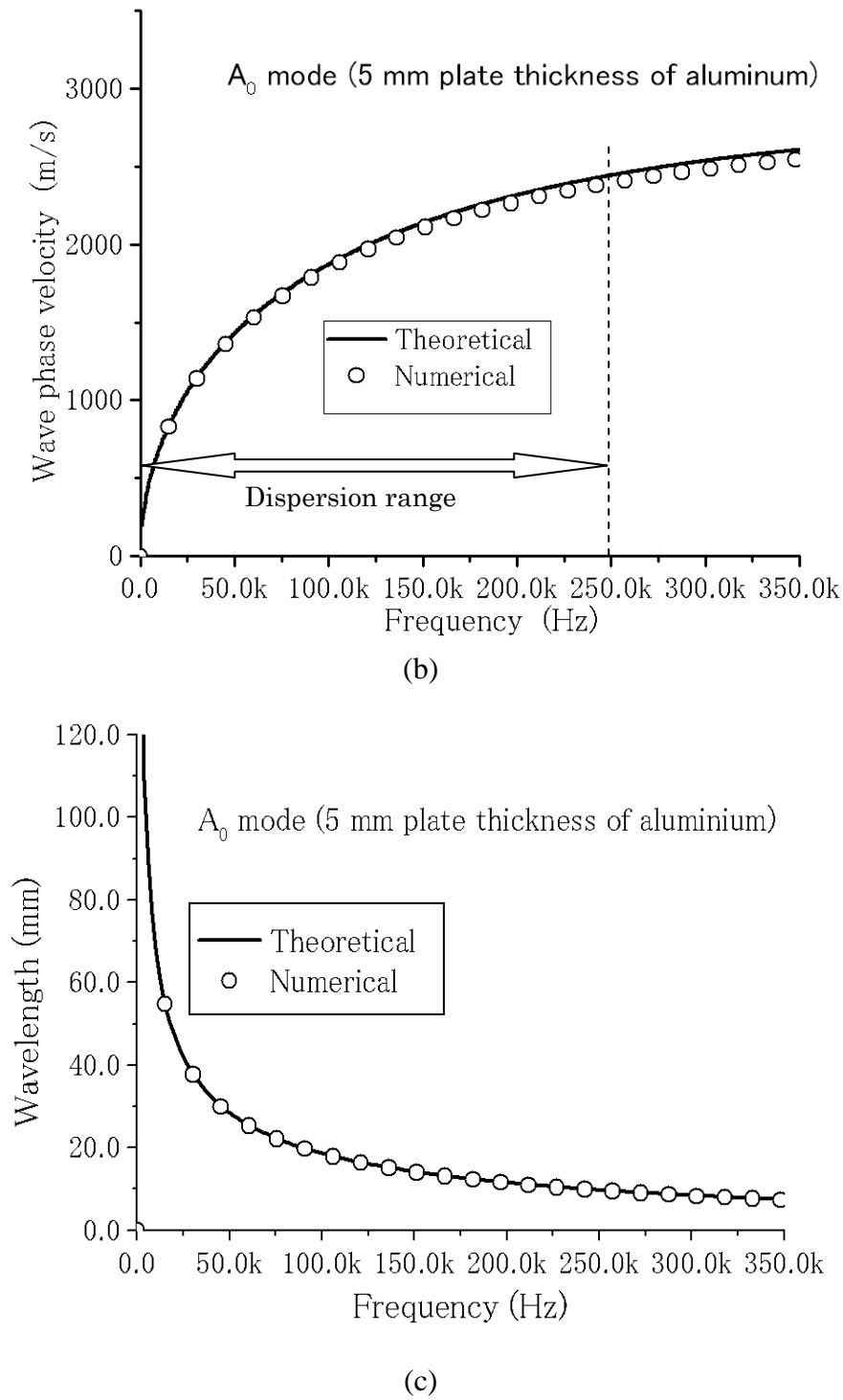


Figure 3.1 Group and phase velocities and wavelength of A_0 mode for an aluminum plate of 5 mm thickness: (a) group velocity; (b) phase velocity; (c) wavelength

To investigate the effect of wave dispersion on the decrease of wave intensity during Lamb wave propagation, the computational modal without damage is shown in Figure 3.2. Similarly to the technique used in [23], two circular PZT units of the diameter of 10 mm and the thickness of 0.5 mm are attached to the top and bottom surfaces of a 5 mm aluminum plate as actuators and out-of-phase voltages ($\pm 25V$) are applied to them to generate the A_0 wave mode. The waveform of input signal is described as follows:

$$P(t) = \begin{cases} 0.5[1 - \cos(2\pi ft/N)] \cos(2\pi ft), & t \leq N/f \\ 0, & t > N/f \end{cases} \quad (3.1)$$

f in Equation (3.1) ranges from 80 to 220 kHz. Similarly, two PZT sensors are attached to the two surfaces of the plate working as sensor 1, and so on for sensor 2 in the same pattern. In this case, pure A_0 wave data can be obtained by taking the signal difference of the top and bottom sensors at the same position. The distance between sensor 1 and sensor 2 is 200 mm. The material properties of the aluminum plate and PZT are listed in Table 3.1, and no physical damping is considered in the simulations. The material properties of PZT in Table 3.1 are the same as those of C-6 PZT (Fuji Ceramics Co.). This C-6 PZT unit was also used in the reference [7] for measuring the group velocity in Figure 3.1(a).

The mesh for the numerical analysis is shown in Figure 3.2(b). Convergence of this mesh has been checked. Note that the present plate element is of multi-layers. In the regions of actuator and sensor, there are three layers (Figure 3.2(b)), i.e., two actuator or sensor layers and one aluminum plate layer. Therefore, the actuators and sensors are considered as independent layers in the plate element, which have different material properties from those of the aluminum plate. The

stiffness and inertia contributions of the actuator and sensor units are integrated into the plate element. In a single layer of actuator, e.g., the upper actuator, the applied voltage is first transformed into the in-plane strain components in this layer by using the elastic constitutive matrix of the actuator. Finally, the in-plane stress components are used to obtain the nodal force vector of the element. The same procedure is performed for the other actuator layer. Since the out-of-phase voltages are simultaneously applied on the two actuator layers, the pure bending moment is consequently generated on this element.

The typical waveforms of sensor 1 and sensor 2 ($N = 5, f = 80$ kHz) denoted by the average strains are plotted in Figure 3.3. To evaluate the signal intensity, as shown in Figure 3.3, similarly to reference [7], the wavelet transformation operated on the original data in the time domain is employed to get the first peaks of the arrival wave, H1 (sensor 1) and H2 (sensor 2). Figure 3.3 shows that the wave amplitude decreases from H1 to H2 as the wave propagates. Finally, H1 and H2 at different frequencies are shown in Figure 3.4. Both H1 and H2 decrease as the frequency increases. Moreover, the rates of decrease at different frequencies, i.e., $H2/H1$, are plotted in Figure 3.4, which shows that the rate of decrease is constant when the wave frequency varies from 80 to 220 kHz. Therefore, it can be concluded that, under this special implemented configuration, such as the plate thickness and distance of the transducers, within the frequency domain from 80 to 220 kHz, the dispersion has no significant effect on the RRI of the wave from damage, which will be neglected in the following sections.

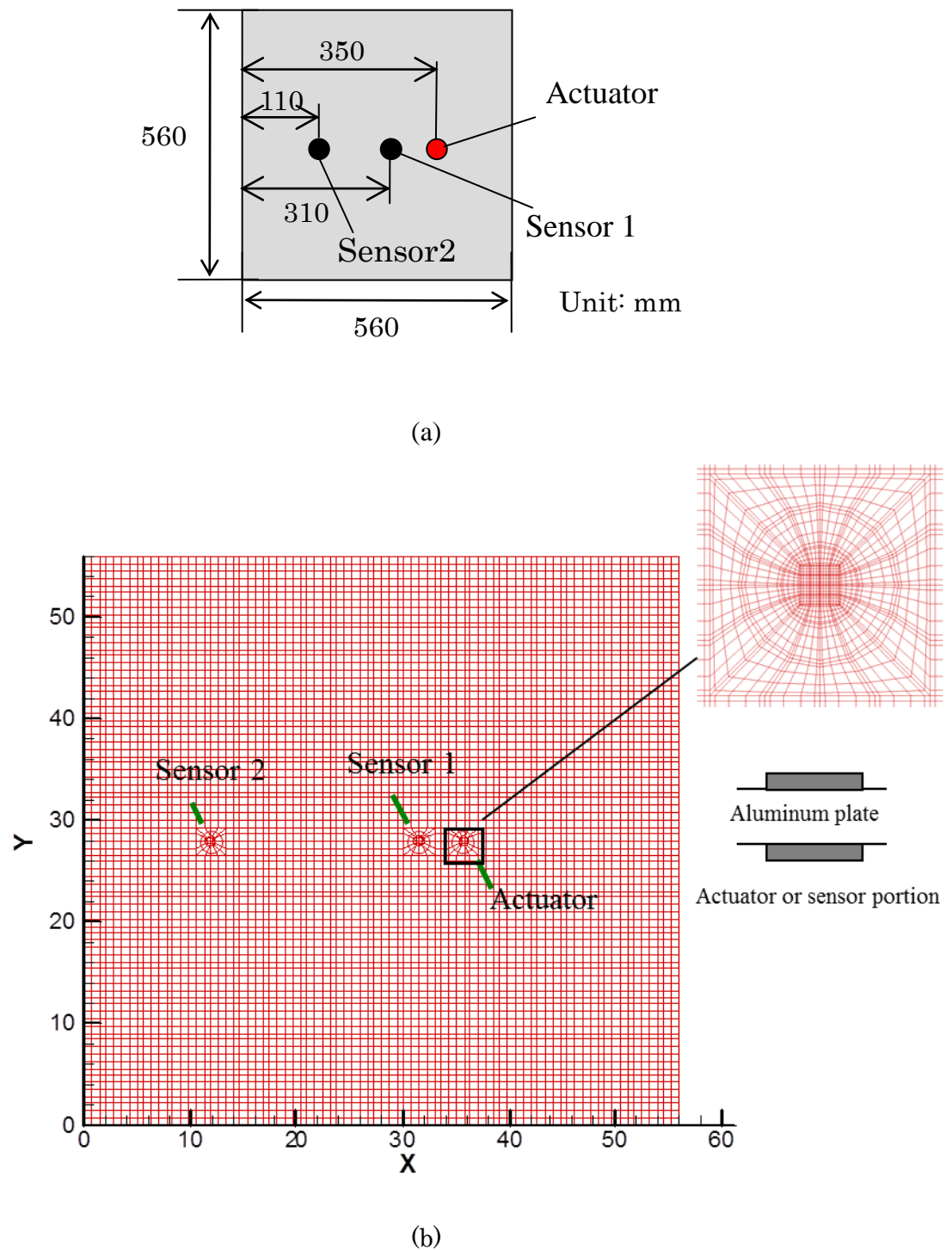


Figure 3.2 Computational model for investigating influence of dispersion: (a) a model of two sensor sets and one actuator set without damage; (b) mesh in numerical simulations

Moreover, we calculate the wave group speed using the model in Figure 3.2 to verify the effectiveness of the pseudospectral Mindlin plate element. The arrival times of the wave at sensor 1 and sensor 2, which correspond to the maximum amplitudes H1 and H2 in Figure 3.3 after the wavelet transformation, are used to obtain the difference of arrival time. With the information on the distance between the two sensor sets, the group velocity can be evaluated as shown in Figure 3.1(a) from 50 to 200 kHz. In this figure, the present numerical model can yield very good results compared with the theoretical and experimental data although the numerical group velocity becomes slightly higher than the experimental and theoretical ones as the frequency increases. In Figure 3.1(b), the numerical phase velocities are also provided. Note that this phase velocity is evaluated from the eigenvalues of a characteristic equation obtained from the governing differential equations of flexural motion (A_0 mode) based on Mindlin plate theory [24]. Then, the numerical wavelength in Figure 3.1(c) is directly obtained from this phase velocity and the frequency. Figures 3.1(b) and (c) demonstrate that the numerical results obtained from the Mindlin plate theory agree very well with the theoretical ones obtained from the Rayleigh-Lamb equation [22].

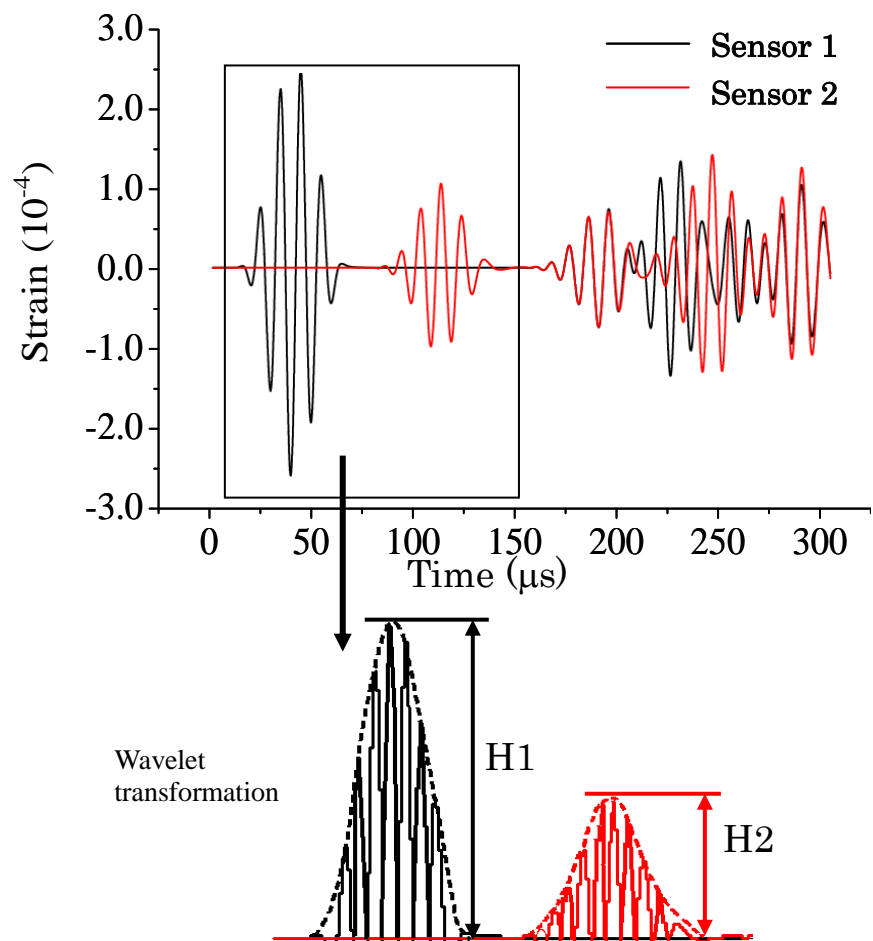


Figure 3.3 Wave signals of two sensor sets ($N=5, f= 80 \text{ kHz}$)

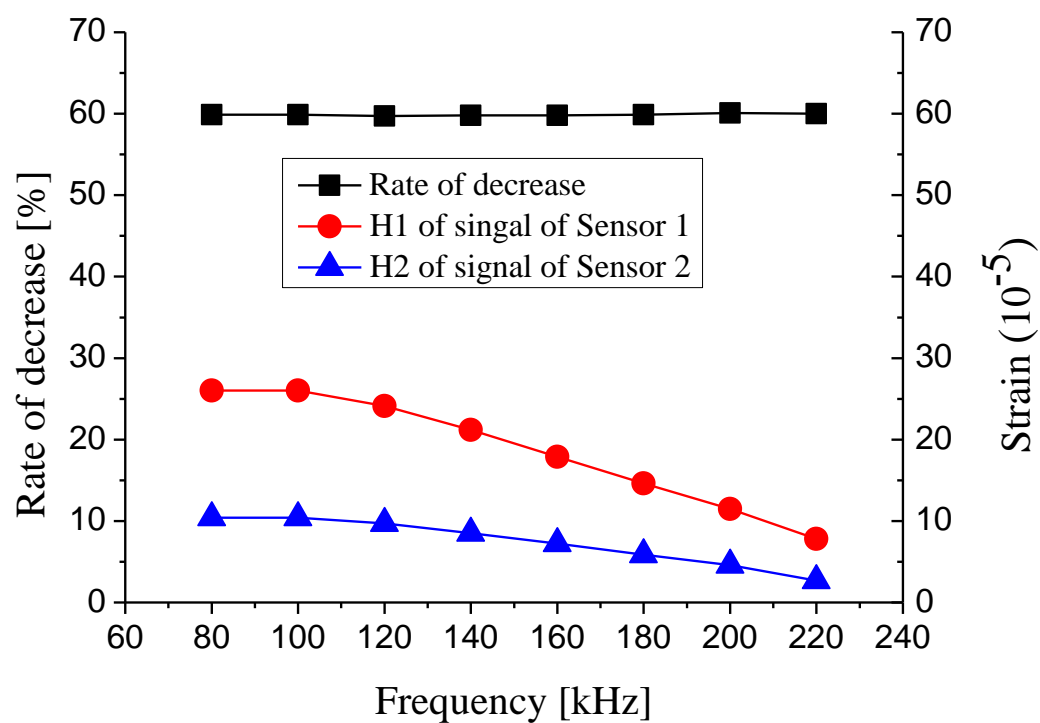


Figure 3.4 Numerical results about the influence of wave dispersion

3.3 Influences of the damage geometry, incident angle and signal frequency on RRI from damage

3.3.1 Effect of damage shape

The computational model is shown in Figure 3.5. The shape of a through-thickness hole in an aluminum plate of the thickness of 5 mm is elliptical, and the shape of the damage is changed as shown in Figure 3.6. The length of the long axis is fixed to be a constant of 20.0 mm and the ratio of A to B , i.e., A/B , varies from 0.1 to 4. Four typical frequencies, i.e., 70 kHz, 80 kHz, 100 kHz and 120 kHz, are employed here. The actuator pair and sensor pair located on the two surfaces of the plate, respectively, are the same with those stated in section 3.2.

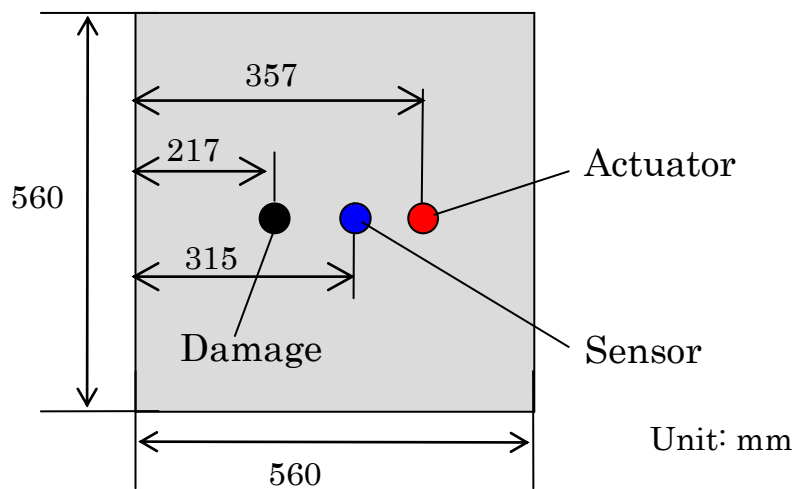


Figure 3.5 Computational model for damaged case

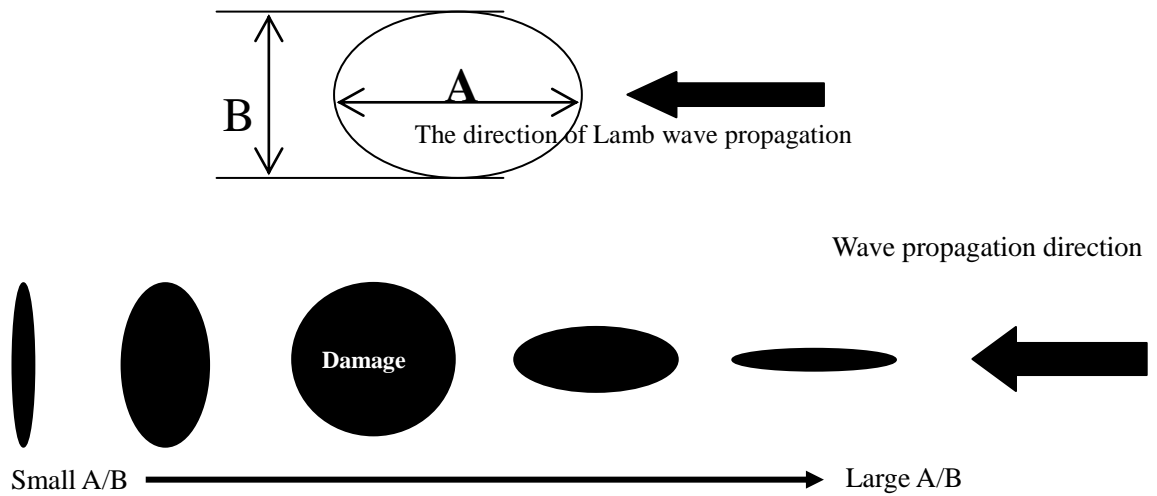


Figure 3.6 Shape of an elliptical hole

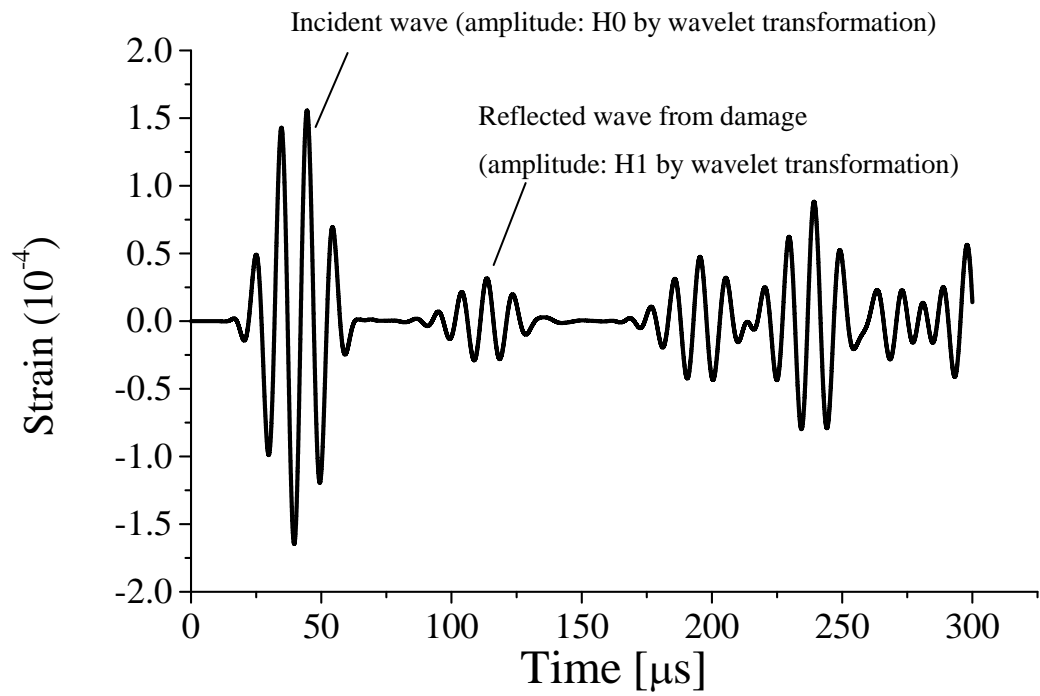


Figure 3.7 Waveform received by the sensor ($N=5, f=100 \text{ kHz}$)

As an example, the lengths of the two axes, i.e., A and B , are 2 mm and 20 mm, respectively. Figure 3.7 shows a typical waveform of 100 kHz received by the sensor. From this signal, we can clearly identify the incident wave and the reflected wave from the damage. Then their corresponding intensities, i.e., H_0 and H_1 , can be obtained from wavelet transformation, and are used to calculate RRI (H_1/H_0). Moreover, the wave propagation configurations for a circular hole, i.e., $A=B=20$ mm, at the time points of 62.96 μ s and 83.95 μ s, are plotted in Figure 3.8, where we can clearly identify the reflected wave from the circular hole in the enlarged illustrations. Figure 3.9 presents the relationship between the shape of damage A/B and RRI from various damages. At four frequencies, there is no obvious difference in RRI. Moreover, by looking at Figures 3.9 and 3.6, it is interesting to note that RRI from a vertical crack-like elliptical hole ($A/B=0.1$) is around two times higher than that from a circular hole ($A/B=1$) when the length of the crack is equal to the diameter of the hole. To understand this result more clearly, as shown in Figure 3.10, we consider a crack of the length of $2R$ and a circular hole of the diameter of $2R$. For the crack, assume that the wave intensity of incident wave at the front of crack is H_0 , without consideration of transmission effect, the reflected wave should be of the intensity H_0 at the front of crack since the incident wave is vertical to the length direction of crack (Figure 3.10(a)). By assuming that the reflected wave intensity received by the distant sensor is H_1 , RRI from the crack can be approximately evaluated as

$$\left. \frac{H_1}{H_0} \right|_c \propto \lambda \times 2R \quad (3.2)$$

where λ is a parameter which represents the attenuation effect due to wave propagation on the backward path from the crack to the sensor. Note that Equation

(3.2) only means that $\left. \frac{H1}{H0} \right|_c$ should be proportional to the crack length if the crack length and the wavelength (Figure 3.1(c)) are approximately of the same order. For instance, the crack length is within several centimeters. Moreover, the maximum $H1/H0$ should be lower than 1 by considering the attenuation no matter how long the crack length is.

On the other hand, for the circular hole, as shown in Figure 3.10(b), the component of the reflected wave at the hole front along x -axis, which can be received by the sensor, is $H0 \cos(2\theta)$. Therefore, by performing the integral along the arc length of the hole front, we can evaluate RRI received by the distant sensor as

$$\left. \frac{H1}{H0} \right|_h \propto \lambda \times \int_{\theta^-}^{\theta^+} \cos(2\theta) R d\theta \quad (3.3)$$

where we assume that the attenuation effect λ due to wave propagation is equal to that in the crack case (Equation (3.2)), which is valid if the distance between the sensor and the damage is much larger than the damage size.

With the consideration of condition $H0 \cos(2\theta) > 0$ to determine the upper and lower limits of the integral for θ , i.e., θ^+ and θ^- , the reflected intensity from the circular hole, which can be received by the sensor, can be evaluated as

$$\left. \frac{H1}{H0} \right|_h \propto \lambda \times \int_{-\frac{\pi}{4}}^{+\frac{\pi}{4}} \cos(2\theta) R d\theta = \lambda \times R \quad (3.4)$$

By comparing Equations (3.2) and (3.4), it can be found that RRI from a crack of the length of $2R$ is just two times higher than that from a circular hole of a $2R$ diameter, which verifies the numerical results in Figure 3.9. Figure 3.9 also implies that a higher RRI can be generated when the direction of Lamb wave

propagation is perpendicular to the long or major axis direction of the elliptical hole by referring to Figure 3.6.

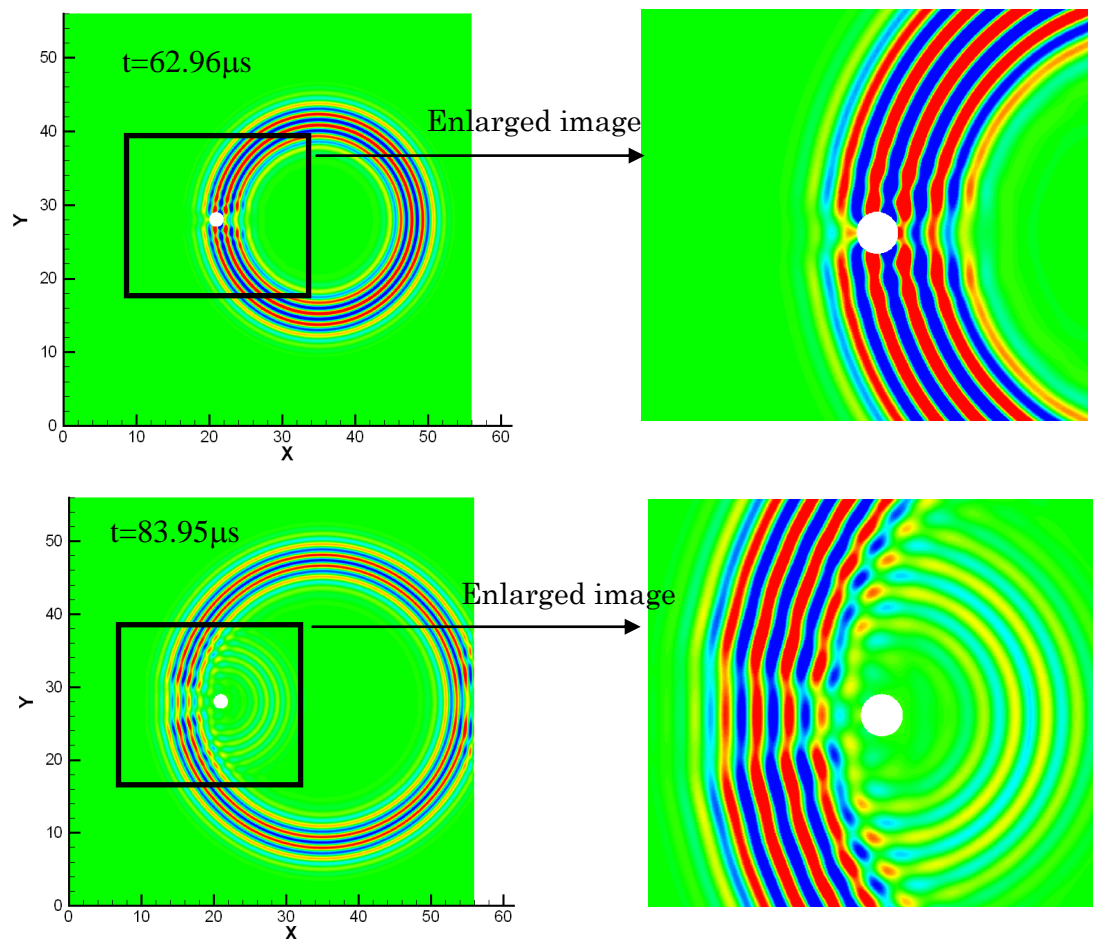


Figure 3.8 Lamb wave propagation images at $t=62.96 \mu\text{s}$ and $83.95 \mu\text{s}$ for a circular hole

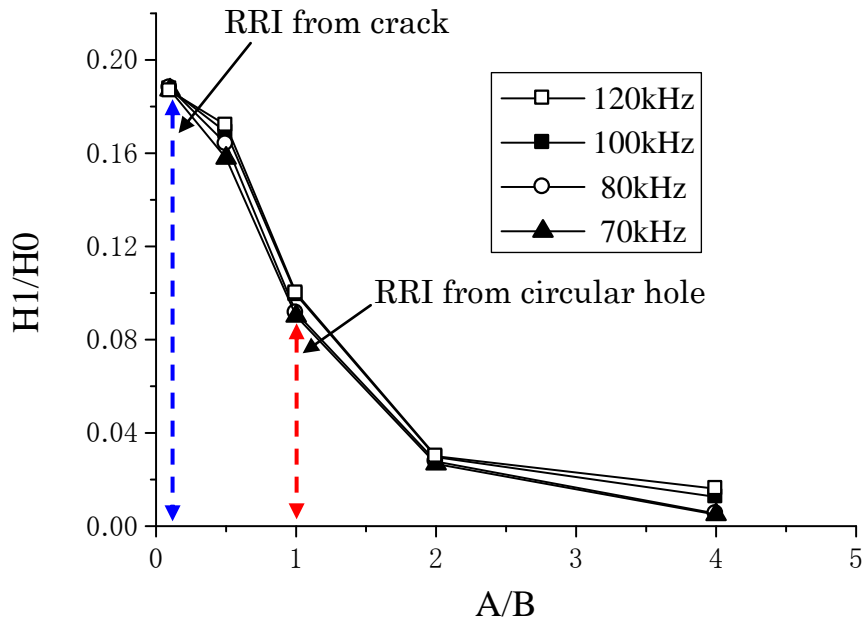


Figure 3.9 Reflection intensity versus A/B

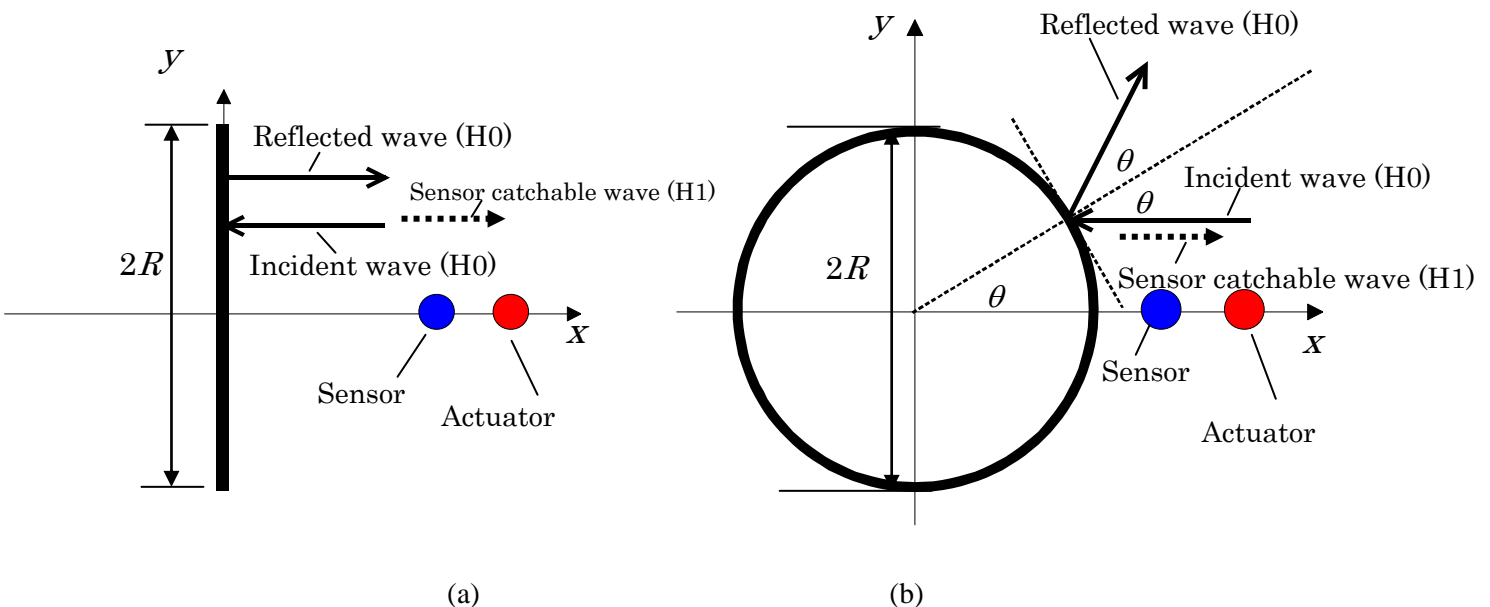


Figure 3.10 Comparison of reflections from a crack and a circular hole: (a) a crack;
(b) a circular hole

3.3.2 Effect of excitation frequency

To investigate the effect of the excitation frequency on RRI from damage, two kinds of damage are chosen, which are a circular hole and a crack-like elliptical hole, i.e., for the hole, $(A, B)=(20 \text{ mm}, 20 \text{ mm})$ and for the crack, $(A, B)=(2 \text{ mm}, 20 \text{ mm})$. The direction of Lamb wave propagation is perpendicular to the long axis of damage. The excitation frequency increases from 80 kHz to 300 kHz with an interval of 20 kHz.

The obtained results are shown in Figure 3.11 for the relationship between the excitation frequency and RRI of the two damages. From it, we can find that there is a special excitation frequency which can induce the highest RRI for both damages. In the following, this special excitation frequency is named as the optimal excitation frequency (OEF). For the hole, OEF is close to 260 kHz; and for the crack, OEF is near 200 kHz. Moreover, the results in Figure 3.11 confirm that the crack is more sensitive to Lamb wave compared with a circular hole as discussed in section 3.3.1.

To address the OEF clearly, the resonant frequency of PZT is obtained as [25]

$$f_r = \frac{\eta_1}{\pi D} \sqrt{\frac{1}{\rho s_{11}^E (1+\nu)(1-\nu)}} \quad (3.5)$$

when the Poisson's ratio ν is taken as 0.35, the parameter η_1 is taken as 2.08 [25]. D is the PZT diameter (10mm), and the in-plane elastic compliance s_{11}^E and the mass density ρ can be obtained from Table 3.1 for the C-6 PZT unit [26]. The calculated PZT resonant frequency in the radial direction of the PZT plate from Equation (3.5) is 203.2 kHz, which is near the reported value of 196.0 kHz for the C-6 PZT unit [26]. Although this PZT resonant frequency is close to the OEF of

the crack, it is obviously lower than that of the hole. Therefore, although at the PZT resonant frequency the maximum intensity of incident wave can be induced, the RRI may not be the highest one since it also depends on some other parameters, such as damage shape, incident angle, etc.

By using the nodal deflections of the plate, the images of Lamb wave propagation in the plate at two excitation frequencies are demonstrated in Figure 3.12. One frequency is the OEF and the other one is a reference frequency for comparison. From Figure 3.12, we can clearly identify that at the OEF the reflected wave packets for the two damages are highly concentrated compared with those at the reference frequencies (see Figure 3.12(d)).

By referring to Figure 3.1(c), at the OEFs for both the crack and the hole, the wavelengths are around 10 mm, which is a half of the hole diameter and crack length. Therefore, wave diffraction phenomena may be significant. However, the results in Figure 3.11 also imply that the RRI does not definitely increase as the excitation frequency increases (or wavelength decreases) regardless of the signal-to-noise ratio problem. Therefore, the common sense that the waves of smaller wavelength are more sensitive to defects may not be absolutely correct, at least in our defined frequency range. Similar results have also been obtained for the delamination in CFRP laminated beams [21], where there are multiple OEFs even for one delamination case, and the wavelengths of some extremely low OEFs are obviously larger than the delamination length. These multiple OEFs were found to be coincident to the natural vibration frequencies of the local delaminated portion [21]. Therefore, the present strongest RRI may be caused by the resonance phenomenon of the damaged region as explained in [21]. For the

present through-thickness areas of damage, it is difficult to build up a model to analyze the natural frequencies due to their strong dependence on the size of the selected local region containing the areas of damage. If the strongest RRI from the damage (Figure 3.12(d)) due to the resonance phenomenon in the local region containing the damage is estimated, there may be some other OEFs when the investigated frequency domain is enlarged.

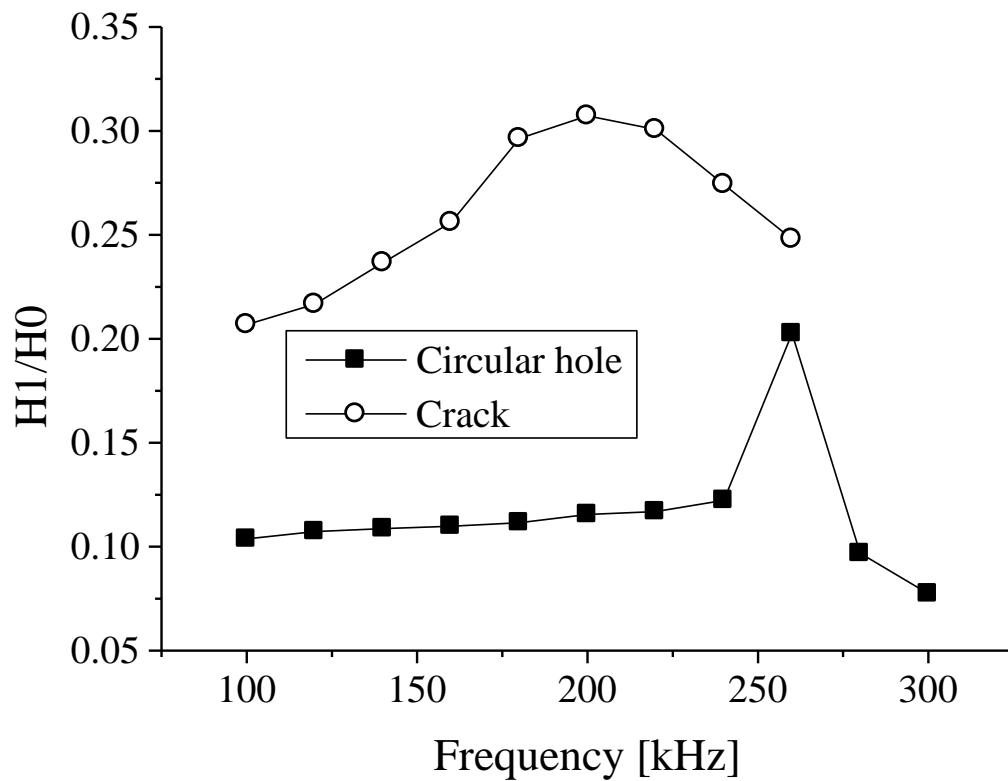
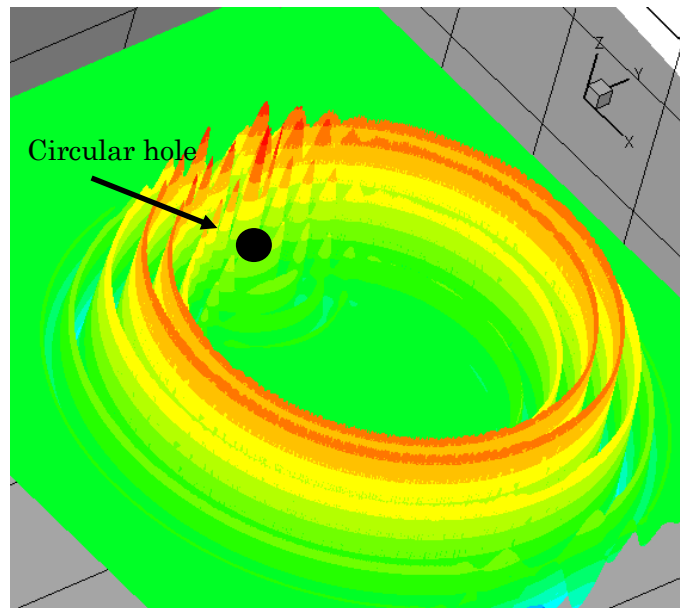
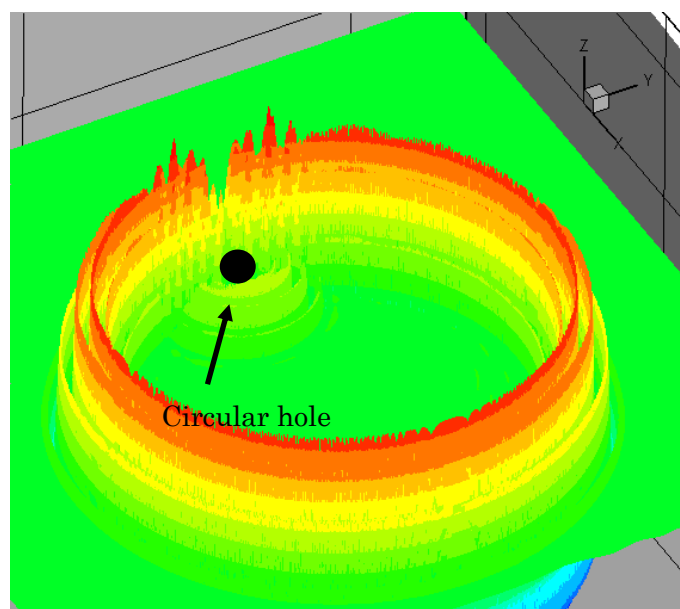


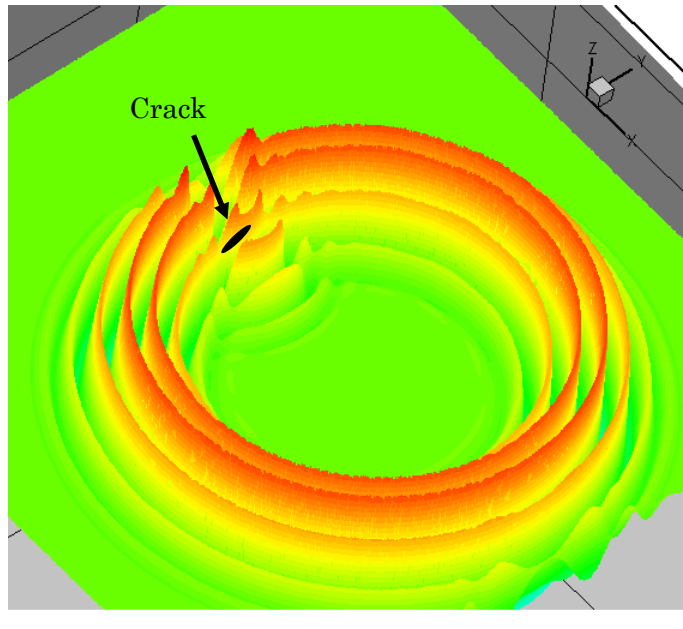
Figure 3.11 Influence of excitation frequency on reflection intensity



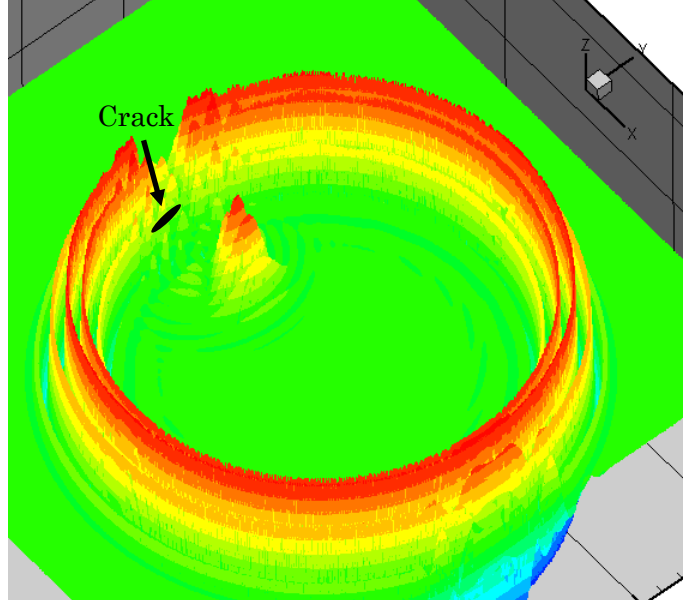
(a)



(b)



(c)



(d)

Figure 3.12 Images of Lamb wave propagation at two frequencies: (a) hole (100 kHz, $t=83.95 \mu\text{s}$); (b) hole (260 kHz, optimal excitation frequency, $t=62.96 \mu\text{s}$); (c) crack (100 kHz, $t=73.87 \mu\text{s}$); (d) crack (200 kHz, optimal excitation frequency, $t=62.96 \mu\text{s}$)

$t=62.96 \mu\text{s}$

3.3.3 Effect of incident angle of Lamb waves

The effect of the incident angle of Lamb waves, i.e., the angle between the direction of Lamb wave propagation and the crack-like elliptical hole defined in Figure 3.13, on the RRI from the damage is investigated. The crack-like elliptical hole is the same as that in section 3.3.2, i.e., $(A, B) = (2 \text{ mm}, 20 \text{ mm})$. Five angles, i.e., $\theta_1, \theta_2, \theta_3, \theta_4$ and θ_5 , as shown in Table 3.2 are chosen in our numerical simulations. The excitation frequency of the incident signal varies from 60 kHz to 240 kHz.

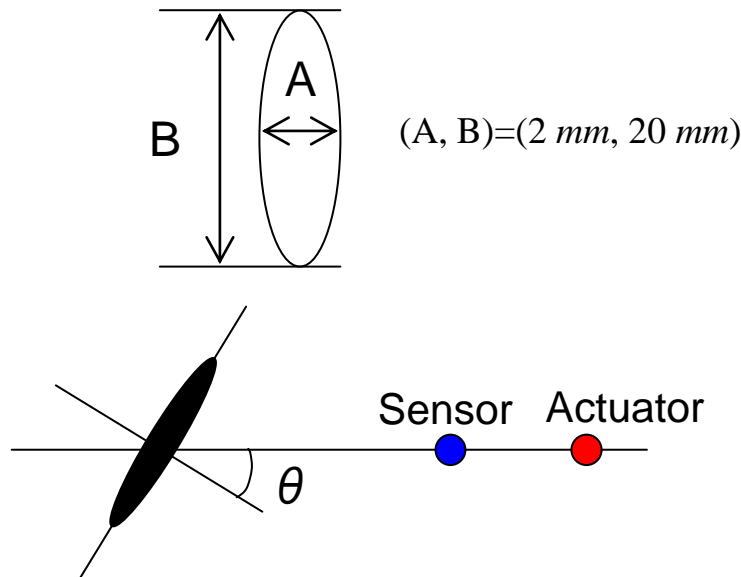


Figure 3.13 Definition of incident angle of Lamb waves to a crack

Table 3.2 Incident angle of Lamb waves

Angle	Degree
θ_1	16.4°
θ_2	23.6°
θ_3	39.2°
θ_4	50.8°
θ_5	61.3°

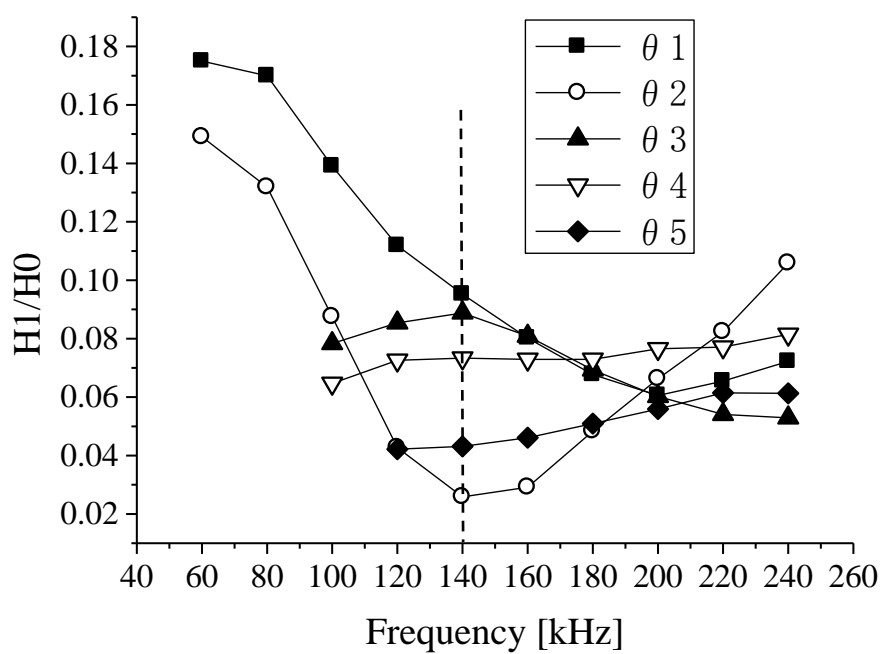


Figure 3.14 Incident angle versus reflection intensity

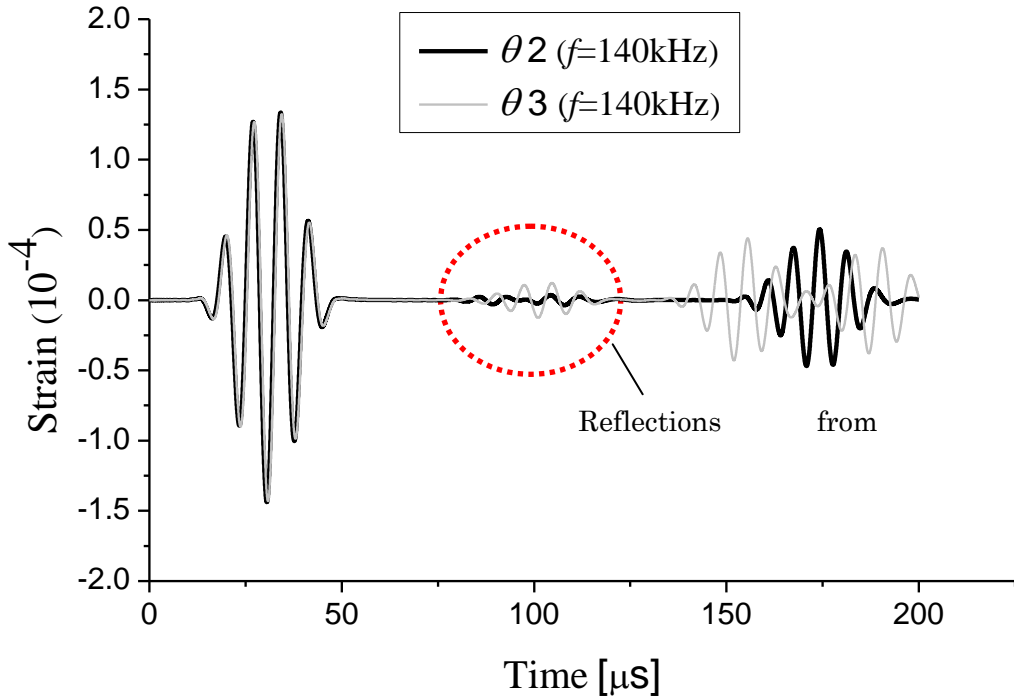


Figure 3.15 Incident angle versus reflection intensity for θ_2 and θ_3

The obtained results are plotted in Figure 3.14. For θ_1 and θ_2 , the RRI from the crack decreases first and then increases as the excitation frequency increases. Therefore, there may be some OEFs below 60 kHz and above 240 kHz. Especially for θ_1 , the slope of the curve at 60 kHz is very small, and an OEF may appear near 50 kHz. This observation confirms our speculation in section 3.3.2 for the existence of multiple OEFs. For θ_3 , there is a peak value near 140 kHz. Interestingly, at 140 kHz, the lowest RRI appears for θ_2 . The wave signals for θ_2 and θ_3 at this frequency (wavelength=18 mm) are plotted in Figure 3.15. From this figure, the strong dependence of the RRI on the incident angle can be clearly observed. For θ_4 and θ_5 , the RRI increases gradually as the excitation frequency

increases, and there may be an OEF in the high-frequency region above 240 kHz. Therefore, it is believed that there must be at least one OEF for any incident angle. Moreover, as the incident angle θ increases (also see Figure 3.11 for $\theta=0^\circ$), the highest value of the RRI decreases and the curve varies more gently. This suggests that as the angle increases the strongest RRI from the crack decreases and the RRI from the crack gradually becomes insensitive to the excitation frequency.

3.4 Conclusion

By employing the Chebyshev pseudospectral Mindlin plate element proposed in chapter 2, the influences of Lamb wave dispersion, excitation frequency in wave signals, the shape of damage, and incident angle of Lamb waves on the RRI from through-thickness elliptically-shaped damages in an aluminum plate are explored in detail. The numerical results show that the Lamb wave dispersion has no obvious effect on RRI. However, the damage geometry, incident angle, and signal frequency have very significant effects on RRI from damage. There are one or multiple OEFs to induce the strongest RRI from damage. This phenomenon may be caused by the resonance at the local damaged region. When the direction of Lamb wave propagation is perpendicular to the long axis direction of elliptical damage, a stronger RRI can be obtained compared with that of wave propagation direction vertical to the short axis direction of damage. Moreover, as the incident angle of Lamb waves increases, the highest RRI decreases and becomes more insensitive to the excitation frequency.

References

- [1] Z. Su and L. Ye. Identification of damage using Lamb waves: from fundamentals to applications. *Springer*, 2009.
- [2] H. Yim and Y. Sohn. Numerical simulation and visualization of elastic waves using mass-spring lattice model. *IEEE Transactions on Ultrasonics, Ferroelectrics and Frequency Control*, 2000, 47: 549-558.
- [3] L. Wang and J. Shen. Scattering of elastic waves by a crack in a isotropic plate. *Ultrasonics*, 1997, 35: 451-457.
- [4] Y. Cho and J. L. Rose. An elastodynamic hybrid boundary element study for elastic guided wave interactions with a surface breaking defect. *International Journal of Solids and Structures*, 2000, 37: 4103-4124.
- [5] S. Liu, S. Datta and A. Shah. Transient scattering of Rayleigh-Lamb waves by surface-breaking and buried cracks in a plate. *Springer*, 1992.
- [6] N. Hu, H. Fukunaga, M. Kameyama, D. R. Mahapatra and S. Gopalakrishnan. Analysis of wave propagation in beams with transverse and lateral cracks using a weakly formulated spectral method. *Journal of Applied Mechanics*, 2007, 74: 119-127.
- [7] N. Hu, T. Shimomukai, H. Fukunaga and Z. Su. Damage identification of metallic structures using A0 mode of Lamb waves. *Structural Health Monitoring*, 2008, 7: 271-285.
- [8] A. Zak, M. Krawczuk and W. Ostachowicz. Propagation of in-plane waves in an isotropic panel with a crack. *Finite Elements in Analysis and Design*, 2006, 42: 929-941.
- [9] E. Le Clézio, M. Castaings and B. Hosten. The interaction of the S_0 Lamb mode with vertical cracks in an aluminium plate. *Ultrasonics*, 2002, 40: 187-192.
- [10] Y. Lu, L. Ye, Z. Su and N. Huang. Quantitative evaluation of crack orientation in aluminium plates based on Lamb waves. *Smart Materials and Structures*, 2007, 16: 1907.
- [11] B. Lee and W. Staszewski. Lamb wave propagation modelling for damage

- detection: I. Two-dimensional analysis. *Smart Materials and Structures*, 2007, 16: 249.
- [12] G. Verdict, P. Gien and C. Burger. Finite element study of Lamb wave interactions with holes and through thickness defects in thin metal plates. *Springer*, 1992.
- [13] Z. Chang and A. Mal. Scattering of Lamb waves from a rivet hole with edge cracks. *Mechanics of materials*, 1999, 31: 197-204.
- [14] O. Diligent, T. Grahn, A. Boström, P. Cawley and M. J. Lowe. The low-frequency reflection and scattering of the S₀ Lamb mode from a circular through-thickness hole in a plate: finite element, analytical and experimental studies. *The Journal of the Acoustical Society of America*, 2002, 112: 2589-2601.
- [15] B. Lee and W. Staszewski. Modelling of Lamb waves for damage detection in metallic structures: Part II. Wave interactions with damage. *Smart Materials and Structures*, 2003, 12: 815.
- [16] V. Agostini, J.-C. Baboux, P. P. Delsanto, T. Monnier and D. Olivero. Application of Lamb waves for the characterization of composite plates. *The Ninth International Symposium on Nondestructive Characterization of Materials*, 1999.
- [17] V. Agostini, P. Delsanto and D. Zoccolan. Flaw detection in composite plates by means of Lamb waves. *Proceedings of the 15th World Conference on NDT*, 2000.
- [18] N. Hu, T. Shimomukai, C. Yan and H. Fukunaga. Identification of delamination position in cross-ply laminated composite beams using S₀ Lamb mode. *Composites Science and Technology*, 2008, 68: 1548-1554.
- [19] D. N. Alleyne and P. Cawley. The interaction of Lamb waves with defects. *IEEE Transactions on Ultrasonics, Ferroelectrics and Frequency Control*, 1992, 39: 381-397.
- [20] N. Guo and P. Cawley. The interaction of Lamb waves with delaminations in composite laminates. *The Journal of the Acoustical Society of America*, 1993, 94: 2240-2246.

- [21] N. Hu, Y. Liu, Y. Li, X. Peng and B. Yan. Optimal excitation frequency of Lamb waves for delamination detection in CFRP laminates. *Journal of Composite Materials*, 2010, 44: 1643-1663.
- [22] I. A. Viktorov. Rayleigh and Lamb waves: physical theory and applications. *Plenum press New York*, 1967.
- [23] Z. Su and L. Ye. Selective generation of Lamb wave modes and their propagation characteristics in defective composite laminates. *Proceedings of the Institution of Mechanical Engineers, Part L: Journal of Materials Design and Applications*, 2004, 218: 95-110.
- [24] N. Hu, H. Wang, B. Yan, H. Fukunaga, D. Roy Mahapatra and S. Gopalakrishnan. The partition of unity finite element method for elastic wave propagation in Reissner–Mindlin plates. *International Journal for Numerical Methods in Engineering*, 2007, 70: 1451-1479.
- [25] Fuji Ceramics Co. Piezoelectric Ceramics: Technical Handbook. <http://www.fujicera.co.jp/product/j/index.html>.
- [26] Fuji Ceramics Co. Material Properties Table. <http://www.fujicera.co.jp/product/j/index.html>.

Chapter 4

**Development of a structural damage imaging approach
based on a Wave Energy Flow (WEF) map**

4.1 Introduction

In order to improve the safety, reliability and operation life of various aged structures, development of powerful NDE techniques to detect possible defects is critical. To date, some techniques, e.g., X-ray inspection [1], infrared temperature measurement [2], thermography [3], eddy-current detection [4], Lamb wave tomography [5], ultrasonic C-scan [6], etc., have been developed. Those methods based on ultrasonic waves [5-8] have been attracting increasing attention and ultrasonic scanning [6] is one of the most commonly used techniques in practice. With this method, a probe scanning at the surface of a structure generates bulk ultrasonic waves, which then propagate along the thickness direction. Internal structural defects can be evaluated by analyzing the time-domain or frequency-domain signal characteristics of transmitted or reflected waves caused by the defects. However, the inspection region of this technique is relatively small. In addition, overlapping and interference of multiple reflected and diffracted waves make the estimation a technical challenge as the validation of inspection results may largely depend on the experience and skill of inspectors. It is quite possible to overlook or even misinterpret some types of defects.

To deal with these problems, some new damage monitoring or inspection techniques based on Lamb waves propagating over a long distance in structural span directions, have been recently developed. The reliability of these approaches has been confirmed in the time reversal method [9-17] and probability-based imaging techniques [18]. The time reversal method is a powerful wave signal conversion technique, which is basically based on Betti's reciprocal theorem, and needs comparatively complex mathematical and experimental operations. The

probability-based imaging approaches need base-line data of intact specimens, which is basically more suitable for on-line health monitoring compared to off-line evaluation. Based on the laser scanning method (LSM) and Betti's reciprocal theorem, Takatsubo *et al.* [19-21] proposed a simple visualization technique using ultrasonic Lamb wave propagation to perform damage inspections. In this method, ultrasonic elastic waves are thermally excited by a pulse laser in a scanned inspection region, and then collected using a fixed acoustic emission (AE) sensor on the surface of a test body. Based on Betti's reciprocal theorem, the waveform propagating from a laser irradiating point to the AE sensor can be directly converted into the waves originating from the sensor and then propagating to the laser irradiating point. Then, a series of snapshots of the wave propagation from the artificial wave source (the sensor position) to the scanned inspection region can be constructed. In this way, defects can be easily identified by directly observing wave scattering caused by them in the snapshots of the wave propagation at different time points, leading to high inspection reliability. Note that this method focuses on the reciprocity of space, i.e., the locations of wave source (actuator) and sensor can be exchanged without any influence on wave propagation in linear and elastic problems. This idea is different from the traditional time reversal method that imitates time back. Moreover, compared with the conventional ultrasonic scanning methods, this technique has the following advantages: quick inspection of a large area, no adjustment on the incident angle of laser irradiation due to stable ultrasonic waves excited by thermal expansion, no need to move sensor, far field operation, simple signal processing, etc..

Unfortunately, although the damage location can be easily identified with this method, often with high accuracy, damage shape and size cannot be evaluated.

In this chapter, inspired by the results obtained in chapter 3, the imaging technique proposed by Takatsubo *et al.* [19-21] was improved to be able to evaluate the shape and size of damage areas. Figures 3.6 and 3.9 present that RRI from a vertical crack-like elliptical hole ($A/B=0.1$) is around two times higher than that from a circular hole ($A/B=1$) even though the length of the crack is equal to the diameter of the hole. It means that reflection or transmission at damage includes some information relating to the shape of damage. Thus, a new wave energy flow (WEF) map concept was proposed. Furthermore, Figures 3.14 and 3.15 show that the intensity of reflected wave from damage is strongly dependent on the incident angle even at the same excitation frequency. Thus, multiple cheap lead zirconate titanate (PZT) sensors instead of a single AE sensor were employed to avoid missing damage with any shape or angle. To validate the improved technique including a new signal processing algorithm, an elliptical through hole or a non-penetrating slit in aluminum plates and invisible internal delamination in a carbon fiber reinforced plastic (CFRP) laminated plate were experimentally evaluated. In addition, numerical simulations were carried out to confirm the obtained experimental results.

This chapter is arranged as follows: the improved technique is described in detail in section 4.2 and the experimental procedure is depicted in section 4.3.1. The experimental and numerical investigations for various damages in aluminum plates and a CFRP laminated plate are reported in sections 4.3.2 and 4.3.3. Finally, some conclusions are drawn in section 4.4.

4.2 A technique based on WEF map

As shown in Figure 4.1, the wave propagating from the laser scanning point A to the sensor B can be directly converted into that propagating from the sensor B to point A based on Betti's reciprocal theorem [19-21]. When irradiating all grid points in an inspection region using LSM, these data can be collected and transformed. With this new data set, the sensor works as an “artificial actuator” and the generated waves propagate from it toward the inspection region. Therefore, in the present work, “sensor” can be considered as “actuator” or wave source point.

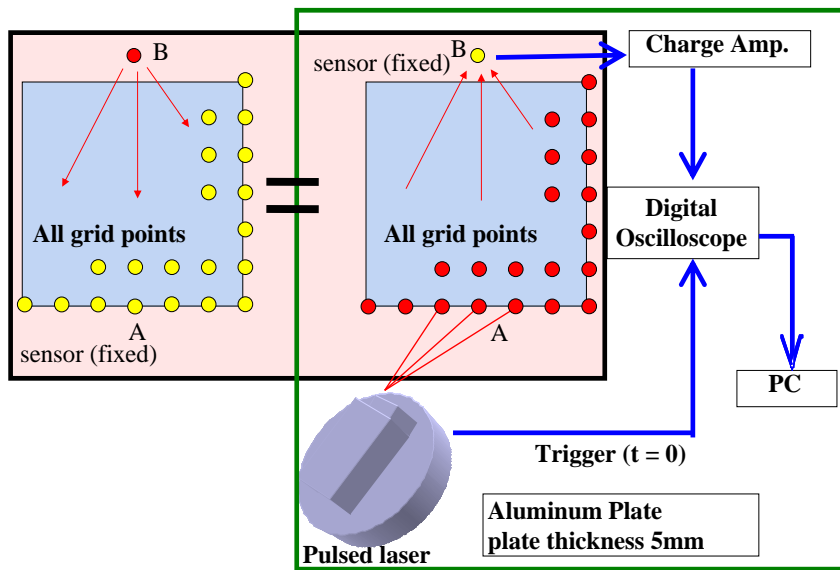


Figure 4.1 Schematic illustration of experimental setup

The present improved technique based on WEF map is innovative and has two advantages compared with the previous technique [19-21]. First, a simple signal processing algorithm can be adopted to construct the WEF map. As we all know, elastic wave propagation in media can be understood as an energy propagation

phenomenon, where the wave energy consisting of mutually interchanged elastic potential energy and kinetic energy is moving forward from a source point. The WEF map represents the distribution of a quantity, which is approximately equivalent to total wave strain energy density during an inspection time period when ultrasonic waves propagate through an inspection region. For a specified scanned point within the inspection region, this equivalent total wave strain energy density passing through this point during the inspection time period can be obtained by using a simple signal processing algorithm proposed in this work. Because the strain energy changes when waves propagate through damage or discontinuity, even for damages with the same maximum sizes but different shapes like a vertical crack-like elliptical hole ($A/B=0.1$) and a circular hole ($A/B=1$) shown in Figure 3.6, the detailed information about the damage, e.g., shape and size, can be simply evaluated from the WEF map. To construct the WEF map, the total wave strain energy density passing through all grid points in the inspection region within a sampling period should be estimated. Unlike the AE sensor used in [19-21], PZT sensors are employed here to collect wave signals, which represent the sum of two in-plane strain components, i.e., $\varepsilon_x + \varepsilon_y$. Therefore, it is easy to estimate a quantity related to strain energy by using the PZT sensor signals directly. Note that the strain energy density can be expressed as:

$(\varepsilon_x + \varepsilon_y)^2(\lambda/2 + G) + G(-2\varepsilon_x\varepsilon_y + \gamma_{xy}^2/2)$ for an isotropic elastic plane problem with two elastic Lame constants, λ and G . Therefore, the square of the PZT sensor signal is proportional to the first term in the above expression. Here, a quantity γ being approximately equivalent to the above strain energy density, which is

named as normalized strain energy density, can be estimated by using the following equation:

$$\left\{ \begin{array}{l} \gamma = \sum_{i=1}^n \alpha_i^2 \quad (i = 1, 2, 3, \dots, n) \\ n = T/\Delta T \\ \alpha_i = \beta(\varepsilon_{xi} + \varepsilon_{yi}) \end{array} \right. \quad (4.1)$$

where T is the sampling time period when ultrasonic waves propagate through the inspection region, ΔT is the sampling interval, β is a proportion constant, ε_{xi} is the strain in X direction at the i th sampling point within T , ε_{yi} is the strain of Y direction. In experiments, the wave signal amplitude (unit: V) of a PZT sensor at the i th sampling point within T was used, on the assumption that it is proportional to the sum of the in-plane strains, i.e., $\varepsilon_{xi} + \varepsilon_{yi}$. After applying Equation (4.1) to every grid point in the inspection region, the WEF map, denoting the distribution of γ , i.e., total normalized strain energy density in the inspection region where ultrasonic waves propagate through during T , can be constructed. Unlike [19-21], which only use the sensor data at a specific time point to reproduce the wave propagation image at this time point, γ in Equation (4.1) is the sum of the squares of the strain signal data during T . Generally, as the strains of elastic ultrasonic waves are very small, the proportional constant β in Equation (4.1) was taken as 1,000 in this work.

Second, multiple PZT sensors with a suitable placement were used to avoid possibly missing some severe defects or erroneous recognition in damage detection. In the chapter 3, it was found that the intensity of the wave reflected from a crack is very weak when the angle between the incident wave direction and the crack length direction is small. This problem cannot be solved when only two

fixed sensors (two artificial actuators here) are used since the straight line connecting them may be parallel to the crack length direction. Therefore, by arranging three or more fixed sensors to form a network, strong interaction between incident waves and damage can be induced from at least one sensor, leading to high reliability of inspection. In this work, three sensors were placed in an equilateral triangle pattern around an inspection region, as shown later. In this case, even if the straight line connecting any two sensors is parallel to a crack length direction, missing of the crack can still be prevented by the third sensor.

4.3 Experimental and numerical procedures for damage evaluation

4.3.1 Experimental set-up

A schematic diagram of the experimental setup is shown in Figure 4.1. The following main devices and components were used: a pulse laser device (lamp-pumped pulse YAG laser, Brilliant Ultra Stable, Big Sky Laser Tech., Inc., Bozeman, MT, USA), three PZT sensors (C6, diameter 10 mm, thickness 0.5 mm, 200 kHz resonant frequency, FUJI Ceramics Co., Shizuoka, Japan), three charge amplifiers (DLPCA-200, FEMTO Inc., Carlisle, OH, USA), an oscilloscope (TDS3034B, Tektronix Inc., Tokyo, Japan) and a personal computer. Note that the duration of the laser pulse is 8.5 ns (120 MHz). For the present laser irradiation, due to the comparatively slow heating speed in the aluminum and CFRP specimens, the wave spectrum shows that the wave energy is mainly distributed from 50 kHz~300 kHz depending on the specimens.

There are the following six steps in this experiment.

- Step 1. Determine the size of scanning interval. The scanning interval should be equal to or less than the half wavelength of Lamb waves propagating in the inspected structure to obtain a satisfactory result. In the aluminum and CFRP specimens, both S_0 mode (large wavelength) and A_0 mode (small wavelength) are generated by the pulse laser due to thermal expansion. The average wavelength of A_0 mode within the above frequency domain is around 10 mm. Therefore, the inspection region was divided into a square grid pattern with an interval of 5 mm. This scanning interval is obtained from our experimental experience, which can yield the high-quality wave propagation images with the minimum scanning data. Too large scanning interval may lead to the low-quality wave propagation images or even discontinuous wave fronts.
- Step 2. Project the pulse laser to a grid point to excite Lamb waves.
- Step 3. Receive the response signals by the three PZT sensors which were firmly bonded on the specimen using epoxy resin adhesive.
- Step 4. Import the signals into the computer through the charge amplifier and the oscilloscope. The length of recorded wave signals should be sufficiently long to ensure that these waves can completely pass through the inspection region. For instance, the velocities of S_0 mode and A_0 mode in the present aluminum plate

are about 5,000 m/s and 3,000 m/s, respectively, and they are of the similar, but slightly higher values in the CFRP plate. The dimensions of inspection region are 200×200 mm² for the aluminum plates, and 100×100 mm² for the CFRP plate. Therefore, the length of the recorded signals was approximately determined as 100 μ s. Band-pass filtering processing was conducted on the receiving data to remove experimental noises.

- Step 5. Repeat the above Step 2–Step 4 to scan every grid point.
- Step 6. Process the recorded signals using Equation (4.1) to calculate γ at every grid point, and then use γ of all grid points to construct the WEF map. Note that in the present experiments, there may be mode changes between A_0 and S_0 modes at damage area (e.g., non-penetrating slit in the aluminum plate or delamination in the CFRP plate). However, these mode changes do not affect the present technique because the new algorithm adds up the signal amplitudes at all sampling points in an entire signal during T no matter what wave modes are contained in this signal (see Equation (4.1)).

4.3.2 Evaluation of damage in aluminum plates

At first, an aluminum plate with an elliptical through hole (minor-axis 12 mm, major-axis 15 mm) as shown in Figure 4.2(a) was used to experimentally and numerically validate the technique of WEF map. Although the elliptical through hole is obviously not a real damage in practical cases, it was used here for

validation purpose only due to its simplicity. The thickness of the aluminum plate was 5 mm. The dimensions of inspection region were 200×200 mm². Three PZT sensors were placed as shown in Figure 4.2(c). Note that, for the aluminum plate, the spectrum of the present experimental Lamb waves mainly ranged from 100 kHz to 200 kHz, which were set as the lower and upper limits of signal band-pass filtering processing. Numerical simulations based on the pseudospectral Mindlin plate element proposed in the chapter 2 were also carried out to simulate wave propagation. Lamb waves were excited by applying the same wave signal as that generated by the pulse laser in the experiment to a PZT actuator. The computational time for one numerical simulation was around 4~5 h when using a personal computer. The length of numerical wave signals used to construct WEF map was also 100 μ s, which is the same as that used for experimental data.

For comparison, at 70 μ s, the snapshots of Lamb wave propagation from the PZTs 1, 2 and 3 obtained by the previous technique [19-21] are presented in Figure 4.3. By observing the wave scattering caused by the elliptical through hole in visualized wave propagation images, the position of the damage can be easily identified. However, the shape and size of damage area cannot be evaluated.

The experimental results obtained by the present technique based on the WEF map are shown in Figure 4.4. There are two points in Figures 4.4(a)–(c) which should be highlighted. The first one is that the normalized strain energy density γ in the hole area is very low. This is because that there is no Lamb waves generated when the inside region of the hole is illuminated by the pulse laser. The second one is that the γ in the area behind the hole decreases significantly due to strong reflections at the hole. The WEF maps of the three PZTs are added up as

shown in Figure 4.4(d). It can be found that the damage shape and area can be evaluated accurately compared to the real damage. For comparison, the numerical results of $\gamma = \sum(\varepsilon_x + \varepsilon_y)^2$ by setting $\beta=1$ in Equation (4.1) are shown in Figures 4.5. It can be identified that the numerical simulation results have the similar variation trends compared to the experimental ones, which indicates the validity of the present technique based on the WEF map.

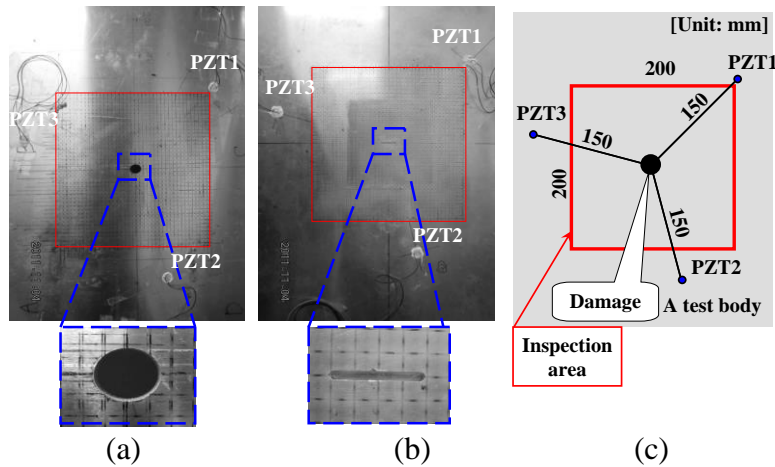


Figure 4.2 Aluminum plates: (a) with an elliptical through-hole; (b) with a non-penetrating slit; (c) position of sensors and damage.

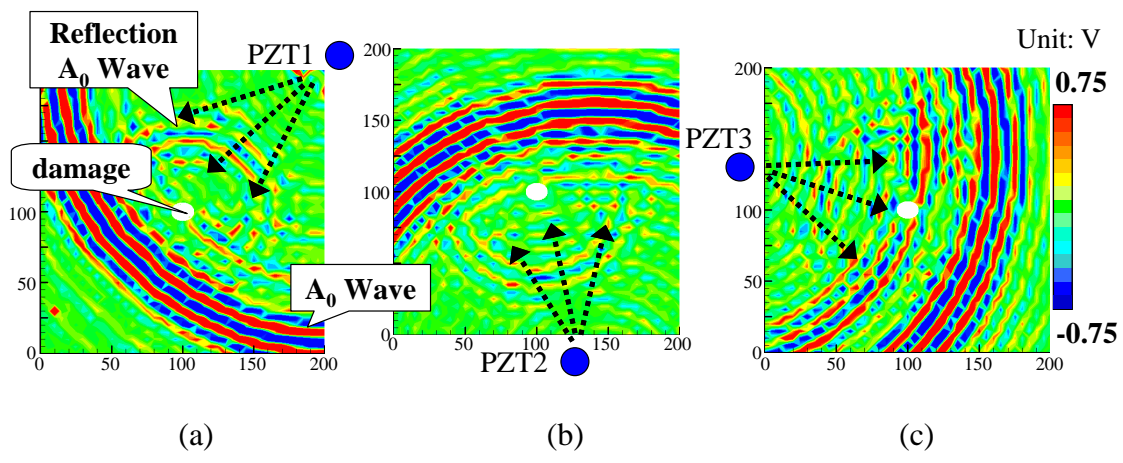


Figure 4.3 Experimental images of Lamb waves (time=70 μ s) using previous technique [19–21] for the aluminum plate with an elliptical through-hole: (a) PZT-1; (b) PZT-2; (c) PZT-3

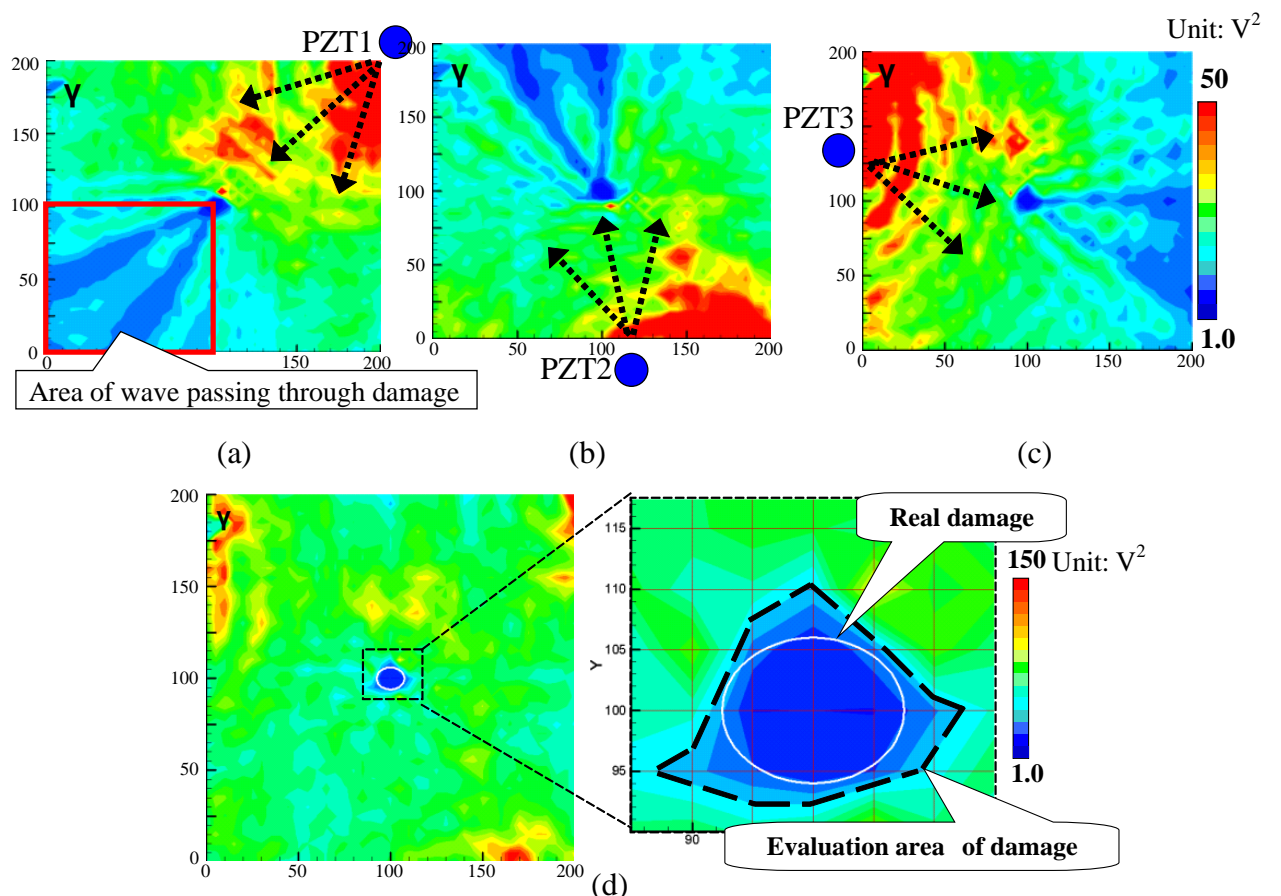


Figure 4.4 Experimental images of γ distribution using the present WEF map technique for the aluminum plate with an elliptical through-hole: (a) PZT-1; (b) PZT-2; (c) PZT-3; (d) PZT-(1+2+3)

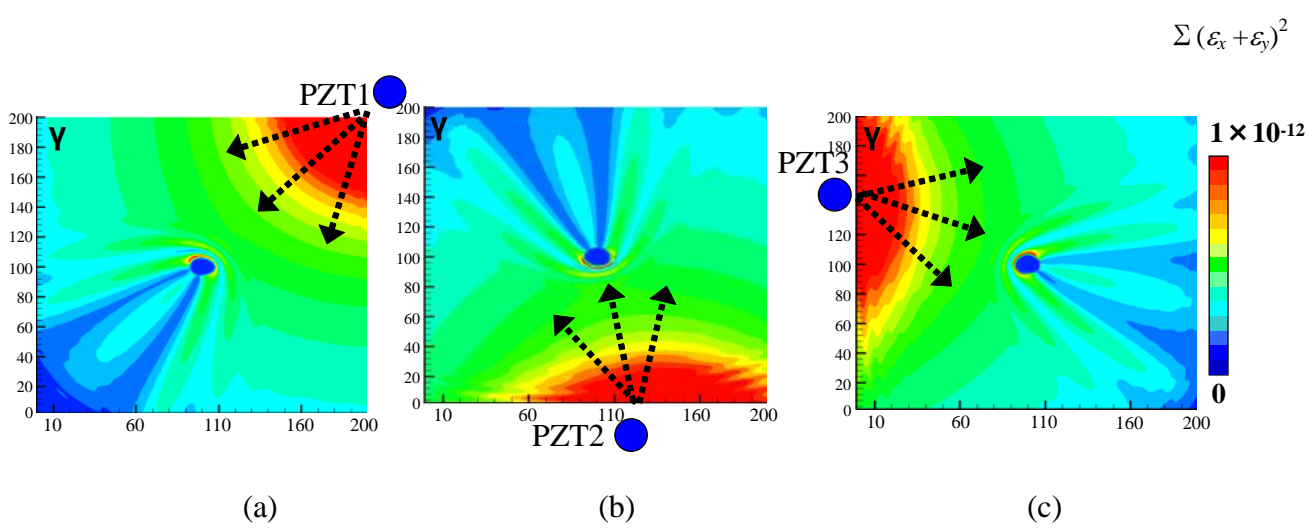


Figure 4.5 Numerical result images of γ distribution using the present WEF map

technique for the aluminum plate with an elliptical through-hole: (a) PZT-1; (b)

PZT-2; (c) PZT-3

Next, an aluminum plate with a non-penetrating slit (length: 20 mm, width: 2 mm and depth: 2.5 mm) as shown in Figure 4.2(b) was used to experimentally validate the present WEF map technique. Similar to the case of the through hole, the surface non-penetrating slit was used as damage due to its simplicity. The thickness of the aluminum plate was 5 mm. The dimensions of inspection region were 200×200 mm². The laser scanning both on the side with the slit and the opposite side was carried out. Firstly, for the side with the slit, the experimental results are shown in Figure 4.6. The decrease of the normalized strain energy density γ in the slit area and that behind the slit caused by the reflection of waves can be clearly observed. Figure 4.6(d) shows the sum of γ using the three PZTs. It can be found that the experimentally evaluated damage (black dashed line) agrees with the real one well in shape and size. Note that the scanning points located in the slit region were also irradiated by the pulse laser.

For the opposite side of the slit, it is useful to imitate some internal damages, such as an internal surface corrosion pit in a pipe because an inspector cannot find it from the inspected side using naked eyes. In this case, a similar result was obtained as shown in Figure 4.7. However, unlike Figure 4.6(d), the normalized strain energy density γ in the slit area in Figure 4.7 is higher than those in the neighboring regions of the slit. The reason may be from the following two aspects. The first one is that, when waves pass through the slit, there should be no obvious reflections in the slit region since the irradiated surface is of no discontinuity. The second one is that, when waves pass through the slit, there should be some strain concentrations or higher strains in the slit region with the smaller thickness. Moreover, there are some misrecognized regions near plate boundaries in Figures

4.6 and 4.7, which should be caused by the strong reflections from the boundaries, i.e., boundary effects, or the superposition of the reflections from the slit and those from the boundaries (e.g., the region near the bottom of the inspected area in Figure 4.7).

Finally, although satisfactory results are obtained in the present example when the slit is located on a grid line, it should be further justified in the future research that the relative position between grid (excitation) points and a damage would affect the results or not, that is, if the slit is not located on the grid points, the results would change or not.

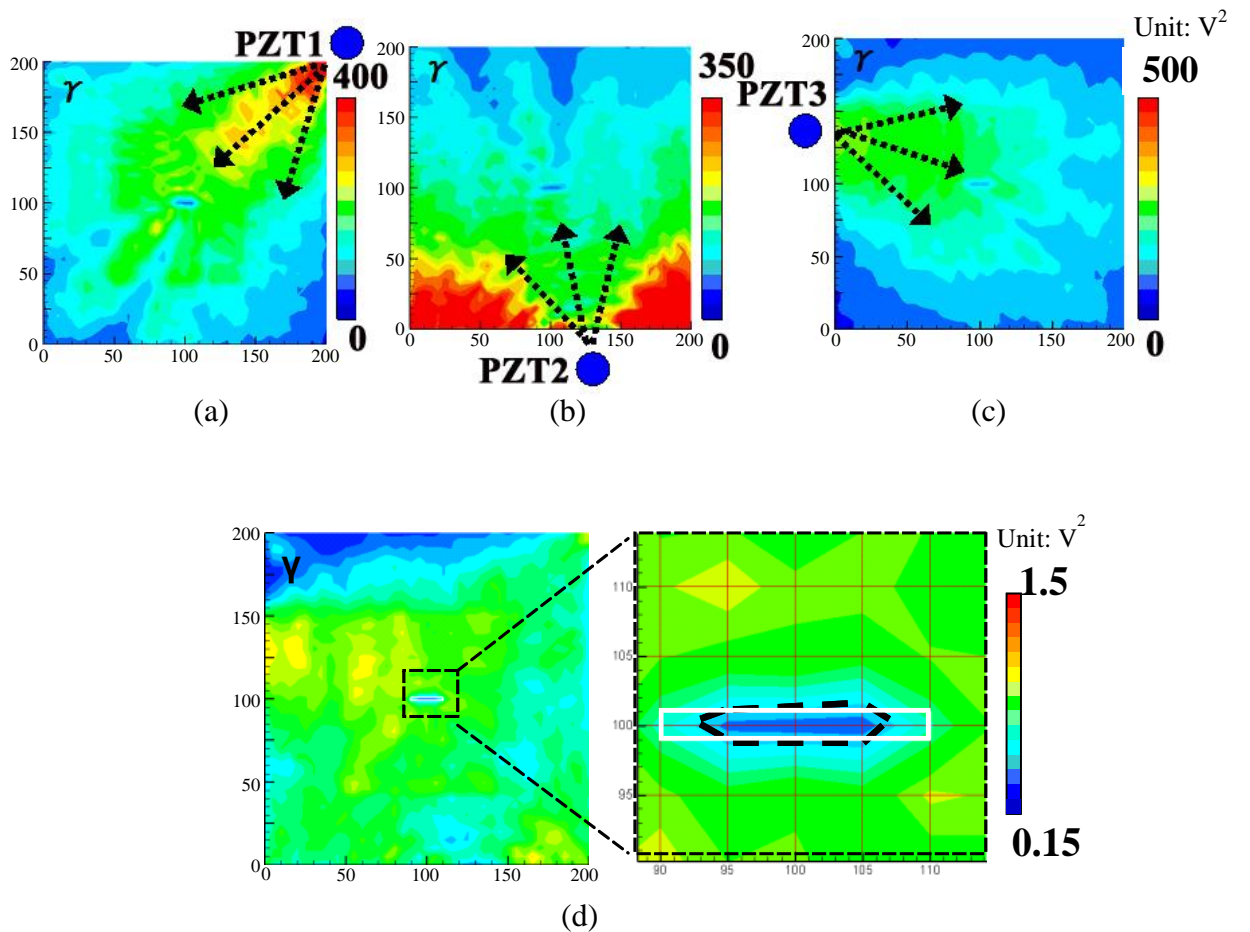


Figure 4.6 Experimental images of γ distribution for the aluminum plate with a non-penetrating slit (irradiated side with slit): (a) PZT-1; (b) PZT-2; (c) PZT-3; (d) PZT-(1+2+3)

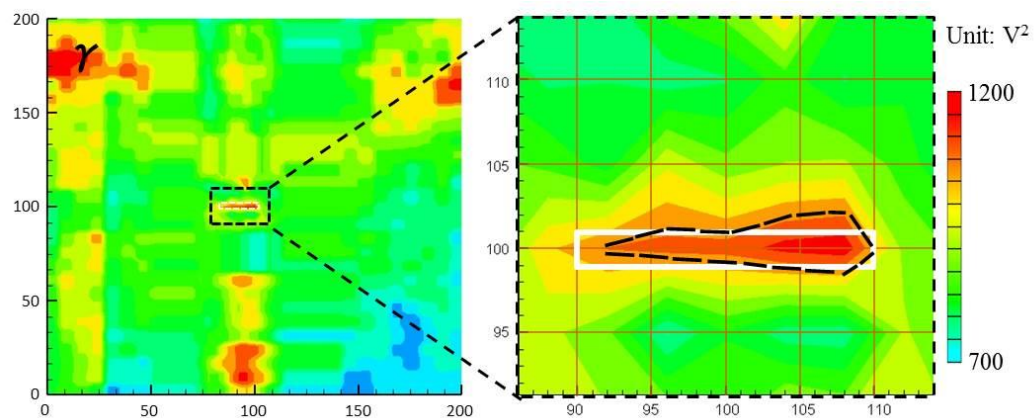


Figure 4.7 Experimental images of γ distribution for the aluminum plate with a non-penetrating slit (irradiated side without slit, result of PZT-(1+2+3))

4.3.3 Evaluation of delamination in a CFRP laminated plate

A 32-layer quasi-isotropic CFRP laminated plate with a stacking configuration of $[(45^\circ/0^\circ/-45^\circ/90^\circ)_8]$ as shown in Figure 4.8(a) was used to experimentally validate the present WEF map technique. The thickness of the CFRP laminated plate was 4.8 mm. For CFRP laminated plates, invisible internal delamination is one of the most dangerous damage patterns since it can significantly reduce the compressive strength of CFRP [22, 23]. In this work, invisible internal delamination was induced by performing a low-velocity impact test using a Dynatup 9250HD weight-drop impact test machine (Instron Inc., Norwood, MA, USA). The center of the plate was impacted by an impacting body of a lower semi-spherical shape, the mass of 4.6 kg and impact energy of 7.0 J.

For reference, Figure 4.9 demonstrates the images of the invisible internal delamination using traditional ultrasonic C-scan by putting the test specimen in water. The scanning was performed from the two sides of the specimen using the scanning interval of 0.5 mm. Figures 4.9(a) and (b) show that the delamination size in the opposite side of impact is slightly larger than that of the impacted side. The maximum diameter of the delamination is around 20.5 mm.

As shown in Figure 4.8(b), the impacted side of the CFRP laminated plate was inspected here with three PZT sensors attached, and the inspection region was $100 \times 100 \text{ mm}^2$. For the CFRP plate, the lower and upper limits of the band-pass filtering in frequency domain were set as 50 kHz and 300 kHz. For comparison, the snapshots of Lamb wave propagation from the PZTs 1, 2 and 3, obtained by the previous technique [19-21], are presented in Figure 4.10. The delamination cannot be easily identified since the wave scattering at the delamination is weak

when using the present scanning grid interval of 5 mm. However, some researchers [19-21] have reported that the wave scattering in a delamination region could be observed by using the scanning grid interval of 1 mm.

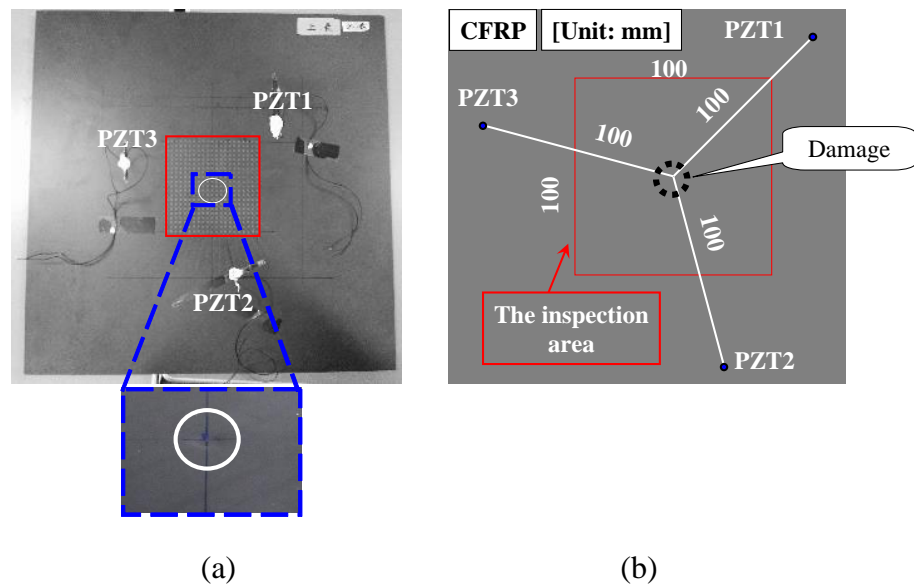


Figure 4.8 Test specimen of a CFRP laminated plate: (a) delamination damage; (b) position of sensors and damage

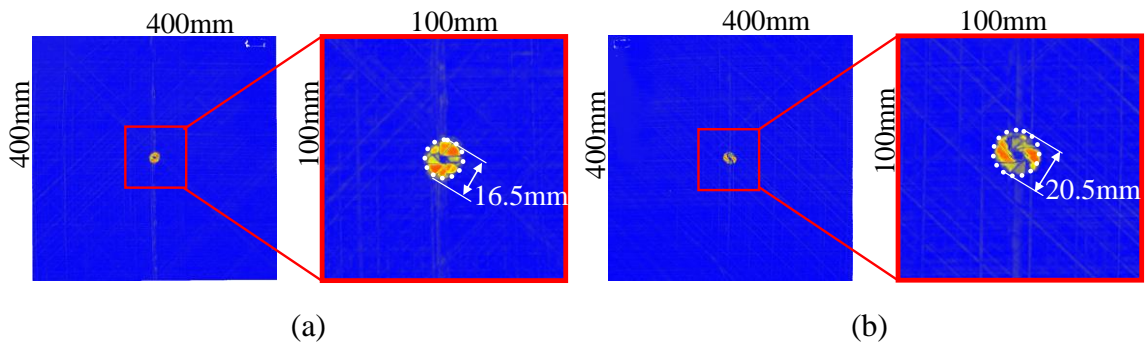


Figure 4.9 Images of delamination using traditional ultrasonic C-scan: (a) impacted side; (b) opposite side of impact

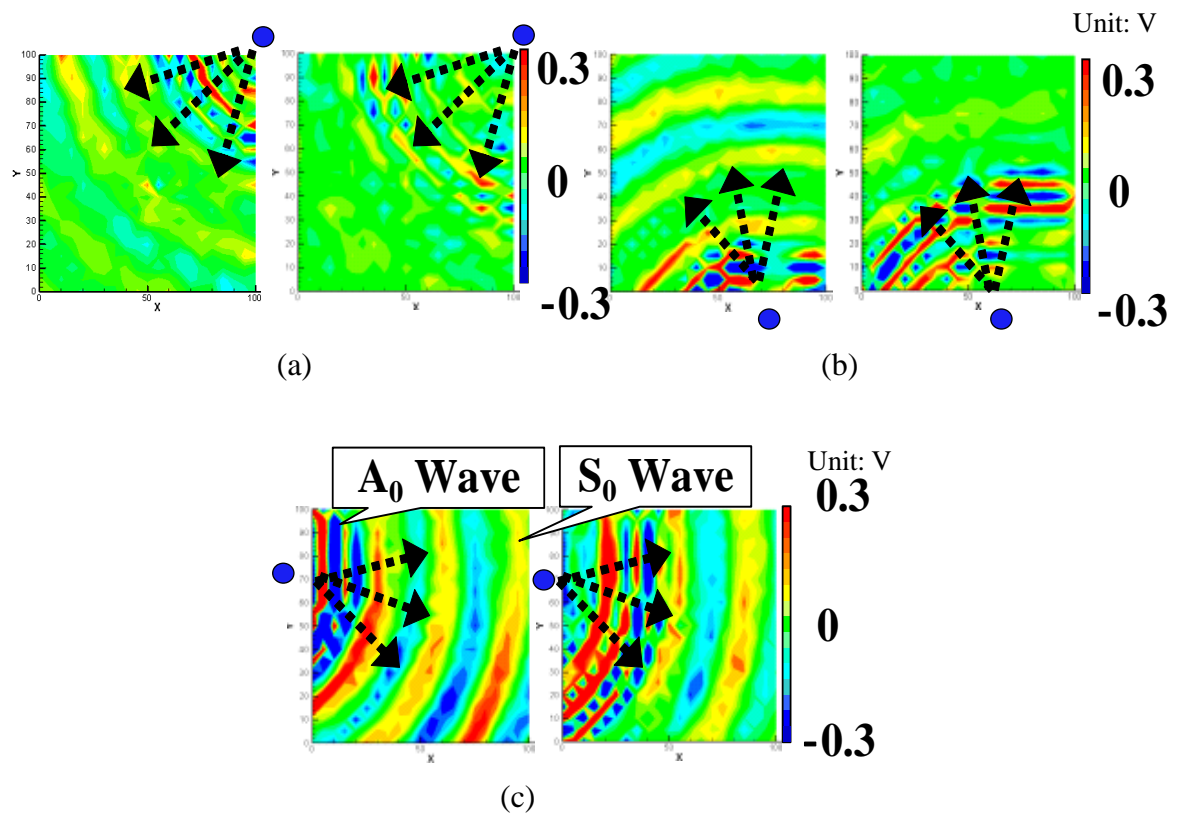


Figure 4.10 Experimental images of Lamb waves for CFRP laminate with delamination (time=40 μ s, 60 μ s) using the previous technique [15–17]: (a) PZT-1; (b) PZT-2; (c) PZT-3

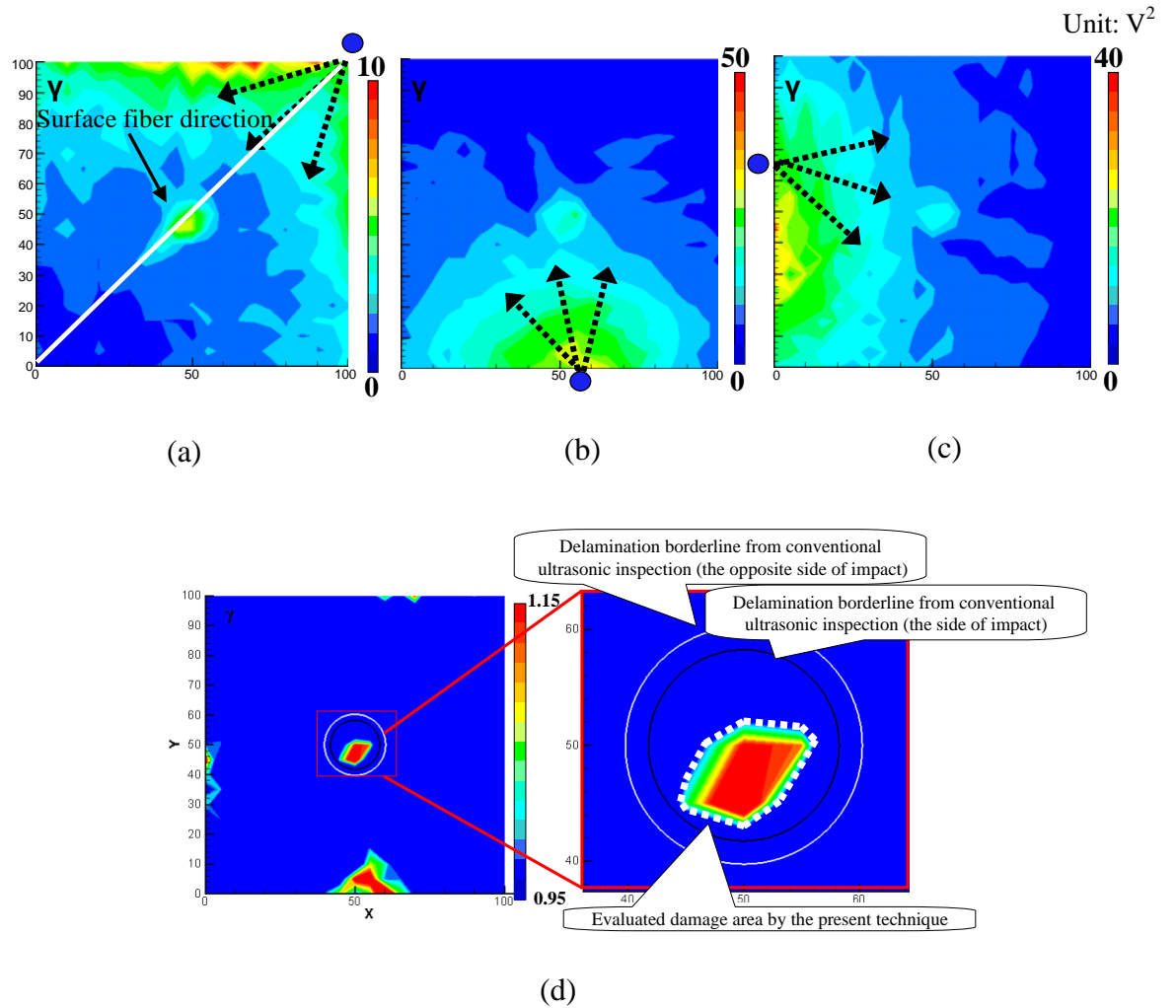


Figure 4.11 Experimental images of γ distribution using the present WEF map

technique: (a) PZT-1; (b) PZT-2; (c) PZT-3; (d) PZT-(1+2+3)

Figure 4.11 shows the results obtained by the present WEF map technique. We can find that the γ in Figure 4.11(a)–(c) decreases after waves pass through the delamination area. However, compared to the previous results of the aluminum plates in Figures 4.4 and 4.6, this decrease is not so obvious. The reason may be that the incident waves can pass through the internal delamination more easily due to no surface discontinuity. Therefore, the reflected waves are relatively weaker, and consequently the influence of the delamination on the transmitted waves is small. Figure 4.11(d) shows the sum of the γ of the three PZTs. Unlike that in Figures 4.4 and 4.6, the γ increases in the delamination area in Figure 4.11(d). The following two reasons may result in this phenomenon. One is that delamination generally leads to the bending stiffness reduction in the delamination area, and consequently bending strain in the delamination area should be larger compared to that of intact area. The other is that there may be many small transverse matrix cracks in the low-velocity impact-induced delamination region [24], leading to high strain concentration. Moreover, from Figure 4.11(d), we can see that the position of the delamination can be identified accurately, but the evaluated delamination area (marked by a white dashed line) is slightly smaller than that obtained by the conventional ultrasonic C-scan. Compared to the interval of 0.5 mm used in the conventional ultrasonic scanning method, the present 5 mm grid interval may lead to the lower accuracy of damage evaluation.

In Figure 4.11(d), there are some areas of high γ , especially at the bottom of the inspection region, which may result in false recognition. This phenomenon may be due to the material anisotropy of CFRP as discussed below. First, the maximum values of γ shown in Figures 4.11(a)–(c) are quite different. As shown

in Figure 4.12, due to a much lower thermal expansion coefficient in the fiber direction, it was found that when an angle between the direction of wave propagation and the surface fiber orientation is closer to 0° , the initial amplitude of the waves becomes smaller when using the laser irradiation to generate Lamb waves [5]. In contrast, when the angle is closer to 90° , the initial amplitude of the waves becomes larger.

Therefore, by observing Figure 4.11(a), the maximum value of γ is much lower than those in Figures 4.11(b) and (c). In this case, the angle between the direction of wave propagation and the surface fiber orientation is very small. On the other hand, the maximum values of γ in Figures 4.11(b) and (c) are very high since the wave propagates almost vertically to the surface fiber direction, which cause the unreal damage areas located on the left and bottom boundaries of the inspection region. Second, the square operation of α_i^2 in Equation (4.1) further amplifies the influence of material anisotropy.

To weaken this anisotropy influence, the sum of absolute value of the wave signals rather than the sum of squares in Equation (4.1) was used to construct the WEF map. The improved WEF map is shown in Figure 4.13. It can be seen that the unreal damages at the boundaries are removed and the evaluated damage area is slightly larger and more accurate than that in Figure 4.11(d).

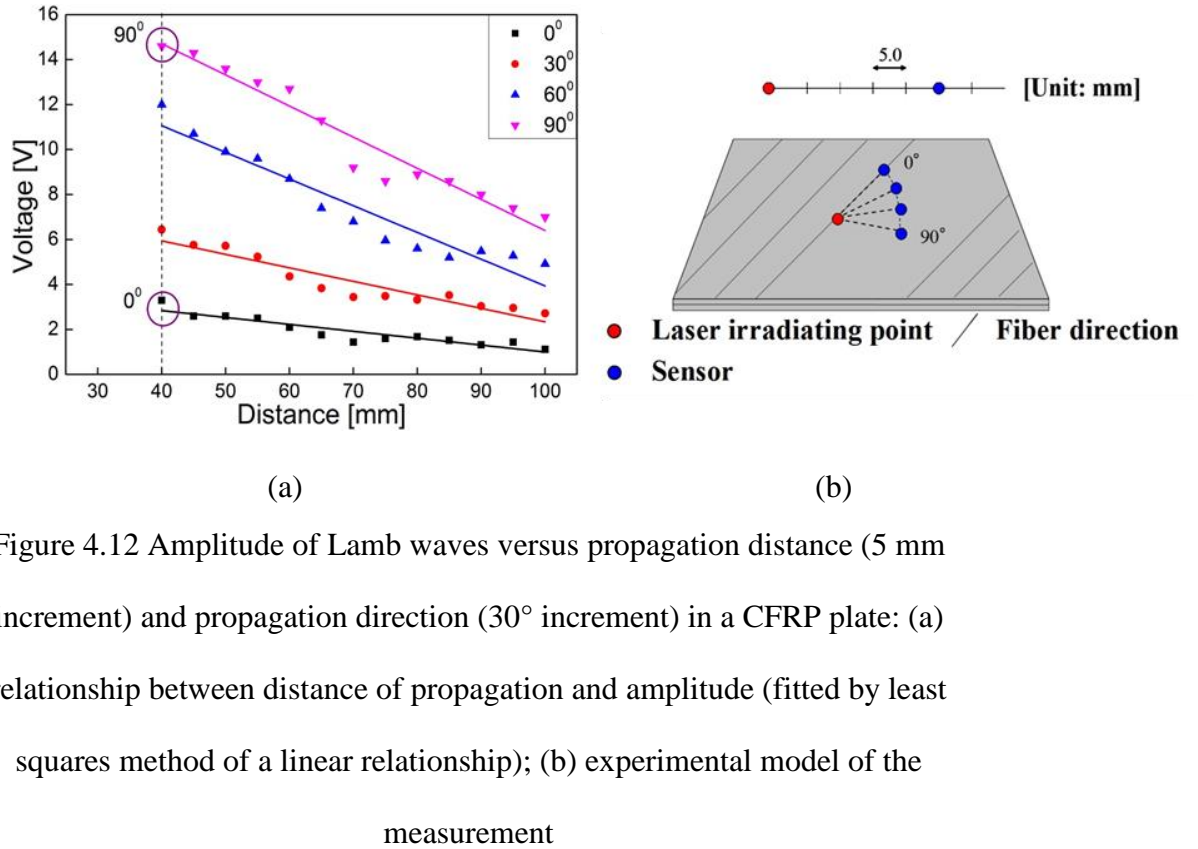


Figure 4.12 Amplitude of Lamb waves versus propagation distance (5 mm increment) and propagation direction (30° increment) in a CFRP plate: (a) relationship between distance of propagation and amplitude (fitted by least squares method of a linear relationship); (b) experimental model of the measurement

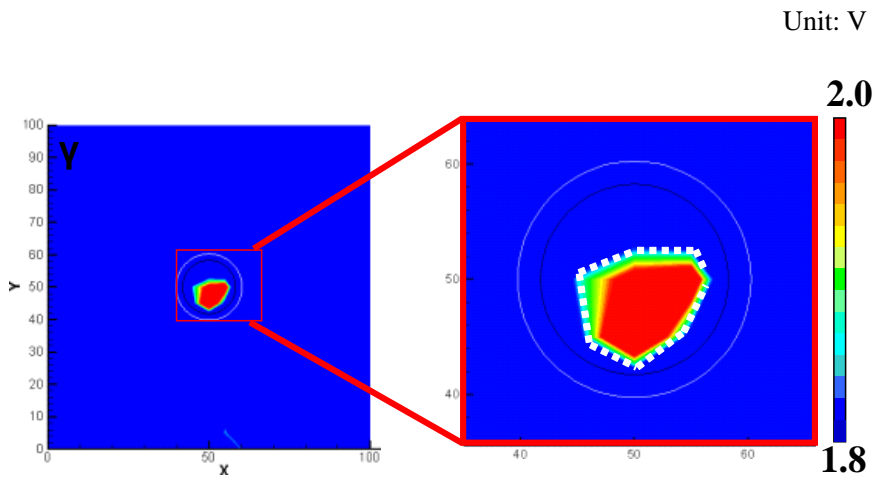


Figure 4.13 Damage image using absolute value of sensor signals in a CFRP plate with delamination

4.4 Conclusion

Based on the concept of WEF map, an improved technique incorporating LSM and Betti's reciprocal theorem was developed to evaluate the shape and size of damage, as well as to visualize wave propagation. In this technique, a simple signal processing algorithm was proposed to construct the WEF map, and multiple PZT sensors were employed to improve inspection reliability and to reduce cost. Two kinds of damages in aluminum plates and invisible internal delamination in a CFRP laminated plate were used to experimentally validate the proposed technique. In addition, numerical simulations were carried out to confirm the experimental results. The conclusions are summarized as follows:

- (1) The damage position in both aluminum and CFRP laminated plates can be accurately identified by the present improved technique based on the WEF map.
- (2) For aluminum plates with an elliptical through hole or a non-penetrating slit, the damage shape and size can be evaluated with comparatively high accuracy. For the CFRP laminated plate with internal delamination, the evaluated delamination area is slightly smaller than the real one. Moreover, it is important to weaken the effect of material anisotropy to improve the quality of delamination image.
- (3) There are still some weaknesses in the present technique, leading to instances of inspection uncertainty or misrecognition. Because the present technique is based on the information of strain within a selected time period, besides damages, a lot of other factors can cause the

variation of strain, e.g., scattering, propagation distance, boundary effects, stiffeners in complex structures, etc.. For instance, wave scattering in various directions due to localized non-uniformities in medium may influence the identification accuracy of damage size and shape, strong boundary reflections may lead to some misrecognized regions, and stiffeners with perfect bonding to host structures may also cause the variation of strain value.

References

- [1] R. Hanke, T. Fuchs and N. Uhlmann. X-ray based methods for non-destructive testing and material characterization. *Nuclear Instruments and Methods in Physics Research Section A: Accelerators, Spectrometers, Detectors and Associated Equipment*, 2008, 591: 14-18.
- [2] A. Mian, X. Han, S. Islam and G. Newaz. Fatigue damage detection in graphite/epoxy composites using sonic infrared imaging technique. *Composites Science and Technology*, 2004, 64: 657-666.
- [3] V. Dattoma, R. Marcuccio, C. Pappalettere and G. Smith. Thermographic investigation of sandwich structure made of composite material. *NDT & E International*, 2001, 34: 515-520.
- [4] P. Horan, P. Underhill and T. Krause. Pulsed eddy current detection of cracks in F/A-18 inner wing spar without wing skin removal using Modified Principal Component Analysis. *NDT & E International*, 2013, 55: 21-27.
- [5] M. Morii, N. Hu, H. Fukunaga, J. Li, Y. Liu, S. Alamusi and J. Qiu. A new inverse algorithm for tomographic reconstruction of damage images using Lamb waves. *Computers Materials and Continua*, 2011, 26: 37.
- [6] B. W. Drinkwater and P. D. Wilcox. Ultrasonic arrays for non-destructive evaluation: A review. *NDT & E International*, 2006, 39: 525-541.
- [7] F. Li, H. Murayama, K. Kageyama and T. Shirai. Guided wave and damage detection in composite laminates using different fiber optic sensors. *Sensors*,

- 2009, 9: 4005-4021.
- [8] D. Li and H. Cao. Monitoring of temperature fatigue failure mechanism for polyvinyl alcohol fiber concrete using acoustic emission sensors. *Sensors*, 2012, 12: 9502-9513.
 - [9] F. Ciampa and M. Meo. Nonlinear elastic imaging using reciprocal time reversal and third order symmetry analysis. *The Journal of the Acoustical Society of America*, 2012, 131: 4316-4323.
 - [10] R. K. Ing, N. Quieffin, S. Catheline and M. Fink. In solid localization of finger impacts using acoustic time-reversal process. *Applied Physics Letters*, 2005, 87: 204104.
 - [11] S. Catheline, M. Fink, N. Quieffin and R. K. Ing. Acoustic source localization model using in-skull reverberation and time reversal. *Applied Physics Letters*, 2007, 90: 063902.
 - [12] H. W. Park, S. B. Kim and H. Sohn. Understanding a time reversal process in Lamb wave propagation. *Wave Motion*, 2009, 46: 451-467.
 - [13] H. Jeong, S. Cho and W. Wei. A baseline-free defect imaging technique in plates using time reversal of Lamb waves. *Chinese Physics Letters*, 2011, 28: 064301.
 - [14] Z. Hai-Yan, C. Xian-Hua, C. Ya-Ping and Y. Jian-Bo. Focusing of time reversal Lamb waves and its applications in structural health monitoring. *Chinese Physics Letters*, 2010, 27: 104301.
 - [15] X. Miao, D. Wang, L. Ye, Y. Lu, F. Li and G. Meng. Identification of dual notches based on time-reversal Lamb waves and a damage diagnostic imaging algorithm. *Journal of Intelligent Material Systems and Structures*, 2011, 1045389X11421821.
 - [16] R. Gangadharan, C. Murthy, S. Gopalakrishnan and M. Bhat. Time reversal technique for health monitoring of metallic structure using Lamb waves. *Ultrasonics*, 2009, 49: 696-705.
 - [17] B. Poddar, A. Kumar, M. Mitra and P. Mujumdar. Time reversibility of a Lamb wave for damage detection in a metallic plate. *Smart Materials and Structures*, 2011, 20: 025001.

- [18] C. Zhou, Z. Su and L. Cheng. Quantitative evaluation of orientation-specific damage using elastic waves and probability-based diagnostic imaging. *Mechanical Systems and Signal Processing*, 2011, 25: 2135-2156.
- [19] J. Takatsubo, B. Wang, H. Tsuda and N. Toyama. Generation laser scanning method for the visualization of ultrasounds propagating on a 3-D object with an arbitrary shape. *Journal of Solid Mechanics and Materials Engineering*, 2007, 1: 1405-1411.
- [20] S. Yashiro, J. Takatsubo and N. Toyama. An NDT technique for composite structures using visualized Lamb-wave propagation. *Composites Science and Technology*, 2007, 67: 3202-3208.
- [21] S. Yashiro, J. Takatsubo, H. Miyauchi and N. Toyama. A novel technique for visualizing ultrasonic waves in general solid media by pulsed laser scan. *NDT & E International*, 2008, 41: 137-144.
- [22] H. Sekine, N. Hu and M. Kouchakzadeh. Buckling analysis of elliptically delaminated composite laminates with consideration of partial closure of delamination. *Journal of Composite Materials*, 2000, 34: 551-574.
- [23] N. Hu, T. Shimomukai, C. Yan and H. Fukunaga. Identification of delamination position in cross-ply laminated composite beams using S_0 Lamb mode. *Composites Science and Technology*, 2008, 68: 1548-1554.
- [24] N. Hu, Y. Zemba, T. Okabe, C. Yan, H. Fukunaga and A. Elmarakbi. A new cohesive model for simulating delamination propagation in composite laminates under transverse loads. *Mechanics of Materials*, 2008, 40: 920-935.

Chapter 5

**Development of a real-time technique for monitoring local
plasticity using Ultrasonic Lamb waves**

5.1 Introduction

As stated previously, SHM plays an increasingly important role in guarantee of structural safety in recent years [1-5]. To date, the majority of the research on SHM has been focused on detecting pre-existing visible or relatively large-sized damages, such as cracks [6-8], holes [9, 10], delamination [11-13], etc. On the other hand, the detection of plastic deformation in the early stage of damage is of paramount importance in engineering application of SHM, as the finally resulted fracture accompanied by crack propagation could lead to serious consequences. For instance, for most of metallic structural components subjected to cyclic loads, fatigue failure scenario usually consists of a crack initiation period and a crack growth period [14, 15]. The crack initiation period is supposed to include the formation and growth of some micro-cracks which are still too small to be visible. In the subsequent crack growth period, the micro-cracks merge together gradually to form the main short fatigue cracks which grow comparatively quickly until the complete failure.

Many microscopic investigations have shown that the initiation of invisible micro-cracks generally occurs very early in the fatigue life. The formation of the micro-cracks may be resulted by different reasons. For instance, at a fatigue cyclic stress lower than the yield strength, surface grains of materials are less constrained by neighboring grains and therefore easy to slip. As a consequence, micro-plasticity preferably occurs in grains at the material surface even at a lower stress, which finally leads to the formation of micro-cracks [16]. Also, the stress higher than yield strength resulted by stress concentration may appear in many structural components because of various reasons, such as the discontinuity of

materials, geometric irregularity, etc. This will result in local plastic deformation and consequent occurrence of micro-cracks.

Local plastic zone is considered as a dangerous position of structures, which makes its detection in earlier stage crucial for evaluating the residual life of the structures and preventing possible disasters. At present, there are few methods for detecting the local plasticity, such as chemical corrosion method [17], electronic speckle pattern interferometry [18, 19], electron backscatter diffraction [20, 21]. However, those methods are limited to specific materials and require pre-treatment for specimens. Furthermore, the literatures [22, 23] reported that nonlinear Rayleigh surface waves and nonlinear ultrasonic bulk waves were applied to the detection of material nonlinearity as an indicator of plasticity-driven damage, and the nonlinear parameters accumulated with wave propagating distance significantly increased when a plate-type intact specimen was under an increasing tensile stress above the yield stress or fatigued with increasing number of cyclic loading. These inspiring results were obtained for a very large plastic area in the specimen, and the sensitivity of the nonlinear parameters for the local plastic deformation needs further investigations. In addition, the nonlinear wave generation technique is very complex, which requires specific instrumentation, and especially, adjustment of excitation frequency for nonlinear Lamb waves. All of these points make the nonlinear wave techniques difficult to field inspection applications at the present stage.

Therefore, the effort on detecting local plasticity in the early stage of damage or some invisible defects is far from enough. This present work has put forward a real-time monitoring technique for local plasticity using linear Lamb waves,

especially fundamental Lamb modes (S_0 and A_0 modes). This technique is based on a hypothesis: supposing that the interaction of Lamb waves with a plastic zone is different from that of Lamb waves with an elastic zone. By investigating the characteristics of S_0 and A_0 modes propagating in an aluminum plate with a circular hole under axial tensile loading, the appearance of local plasticity around the hole can be monitored. In section 5.2, pre-requisite experiments were done to investigate the yielding property of the test specimen and select suitable sensors used in experiments. In section 5.3, an experimental scheme based on a directional actuator/sensor set was designed to demonstrate how the local plasticity could be detected using Lamb waves. Section 5.4 explained the signal processing methods and presented the experimental results. The experimental data were processed using a pulse compression technique for easily distinguishing the wave signals of S_0 and A_0 modes. The changes of wave amplitude with the increase of stress for both S_0 and A_0 modes were presented to monitor the appearance of the plasticity. Moreover, the obtained wave signals at different stress levels were further analyzed through wavelet analysis by virtue of a signal index I , whose variations caused by plastic deformation were more obvious. In section 5.5, a series of numerical stress simulations of tensile test were conducted using the finite element analysis (FEA) to further understand the experimental results. Finally, some conclusions were drawn in section 5.6.

5.2 Pre-requisite experiments

A thin plate specimen with a circular hole, made from A5052 aluminum with material properties listed in Table 5.1, was used. The dimensions and geometries

of the specimen are shown in Figure 5.1.

5.2.1 Measurement of stress-strain curve

As a pre-requisite, the yielding property of the specimen should be clarified. By using an Instron universal testing machine (Instron 5982, Instron Co.), a preliminary tensile test of the specimen was performed. A strain gauge was attached on the specimen at the position of 5 mm away from the hole (see Figure 5.1) to measure the strain. For reference, another intact plate specimen with the same size but without a hole was also tested. The obtained nominal stress-nominal strain curves are shown in Figure 5.2. The yield strength is defined at the stress level corresponding to the intersection of the stress-strain curve with a line parallel to the elastic slope of the curve with an offset of 0.2% strain. It can be seen from Figure 5.2 that the yield strength is 155 MPa for the specimen with a hole and plasticity occurs in the position attached by the strain gauge. On the other hand, at the same stress level, the same position in the intact specimen is still in elastic state. Such distinctive difference of these two specimens can be attributed to the high stress concentration around the hole.

Table 5.1 Material properties of A5052 aluminum

Density	Young's modulus	Poisson's ratio	Yield strength	Tensile strength
2710 [kg/m ³]	68.9 [GPa]	0.3	210 [MPa]	260 [MPa]

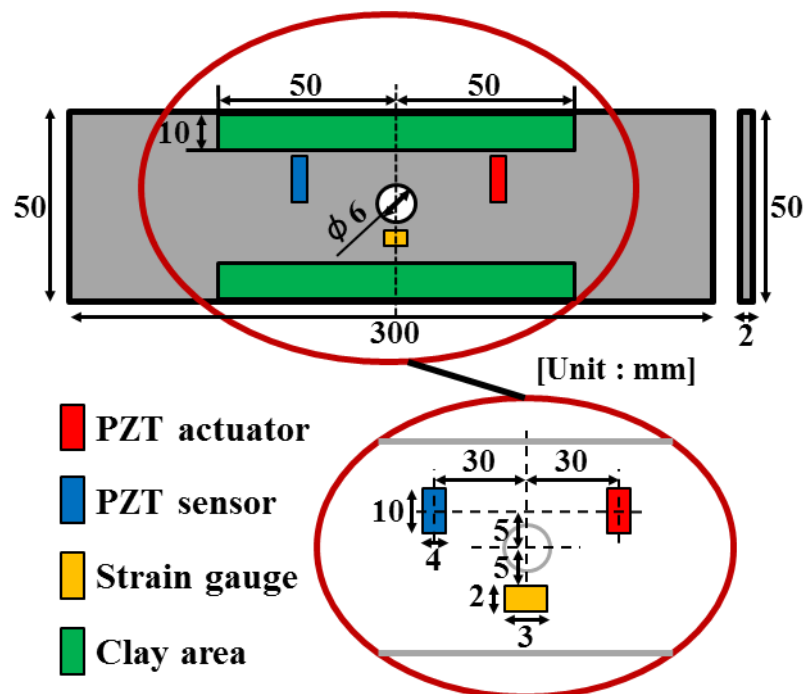


Figure 5.1 Schematic view of experimental specimen

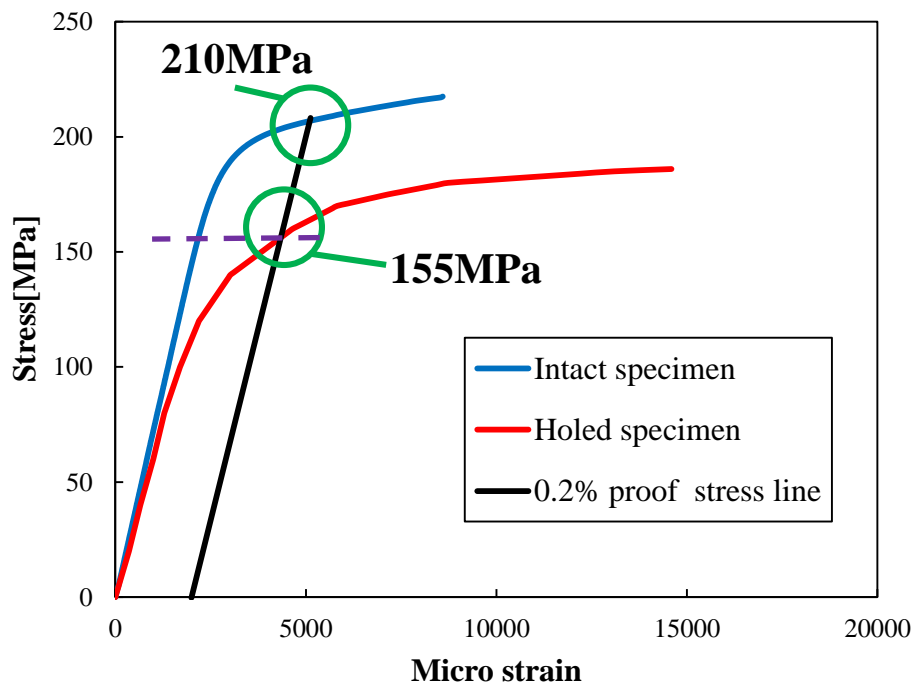


Figure 5.2 Nominal stress-nominal strain curves

5.2.2 Employment of clay and directional actuator/sensor set

For the plate specimen with small sizes as shown in Figure 5.1, during propagation, Lamb waves will reflect from the four edges of the specimen within a short time. It can be predicted that these reflections will be mixed with the target wave signals, which increases the complexity of wave signal analysis. To reduce the reflections from boundaries, we employed two methods. First, we laid fat clay of the thickness of 5 mm on the two sides of the plate (see Figure 5.1, front and back surfaces of the plate). It is well-known that acoustic impedance of the fat clay is much closer to that of the aluminum compared to air, thus the reflections from the two side boundaries might be decreased. The experimental data demonstrated that the fat clay can effectively reduce the reflection intensity from the two sides of the plate. Second, a directional actuator/sensor set was designed to concentrate wave energy in wave propagation direction as much as possible. As well-known, a circular-type PZT actuator or sensor can generate or receive waves uniformly in all directions, which is not suitable for the present plate specimen with small sizes. Therefore, rectangular-type PZTs were employed in the present research.

Two verification experiments were conducted to study the directionality of rectangular-type PZTs. The experiment as shown in Figure 5.3 was performed to investigate the characteristics of generated S_0 and A_0 modes in different directions and different distances, when a rectangular-type PZT (width 10 mm, thickness 0.5 mm, length 4 mm, FUJI Ceramics Co.) with around 200 kHz resonant frequency was used as actuator and an acoustic emission (AE) sensor (AE-930N, Electronic Instrument Co.) was used. Moreover, in this research, the chirp burst wave was

chosen as the input signal on the actuator, which can be described as follows:

$$P(t) = \begin{cases} \left[0.5 - 0.5 \cos\left(\frac{2\pi t}{T}\right) \right] \sin\left[2\pi\left(f_0 t + \frac{B}{2T} t^2\right)\right] & t \leq T \\ 0 & t > T \end{cases} \quad (5.1)$$

where t is time in second, f is the central frequency, and B is the frequency sweep width. In this experiment, $f_0 = 400$ kHz, $B = f_0/2$ kHz, $T = (1/f_0) \times 5000$ sec. Figure 5.4 shows the waveform in time domain and the frequency spectrum of the input signal. From it, we can see that the incident wave is a broad-band signal in frequency domain from 0 to 800 kHz. By virtue of dispersion curves of group velocity for an aluminum plate shown in Figure 5.5, it can be predicted that only S_0 and A_0 modes can be generated in the thin plate specimen.

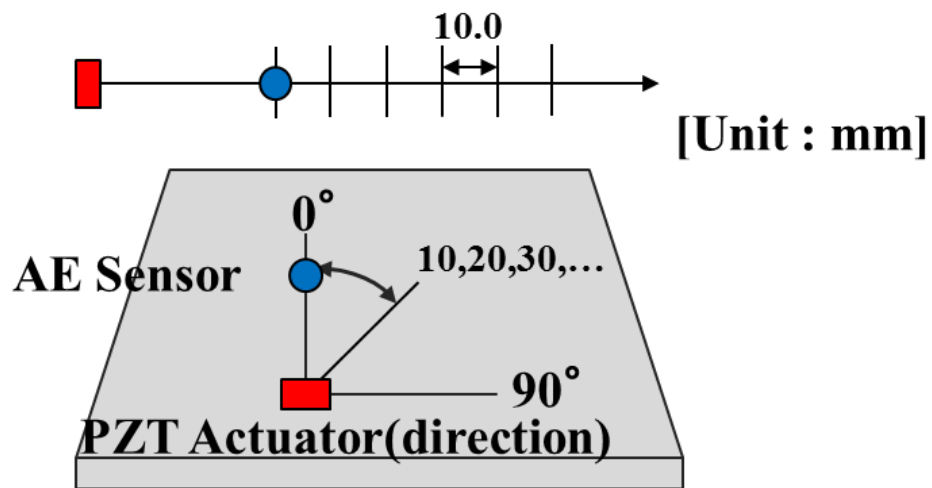


Figure 5.3 Schematic view of experiment (rectangular-type PZT used as actuator)

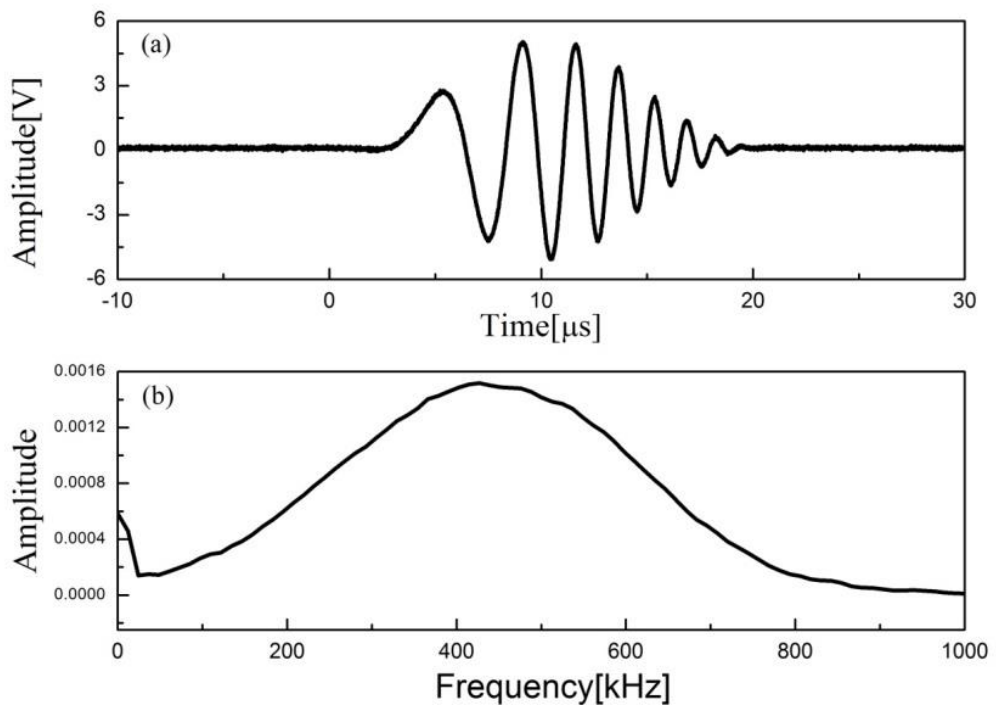


Figure 5.4 Input signal: (a) waveform in time domain; (b) FFT spectrum

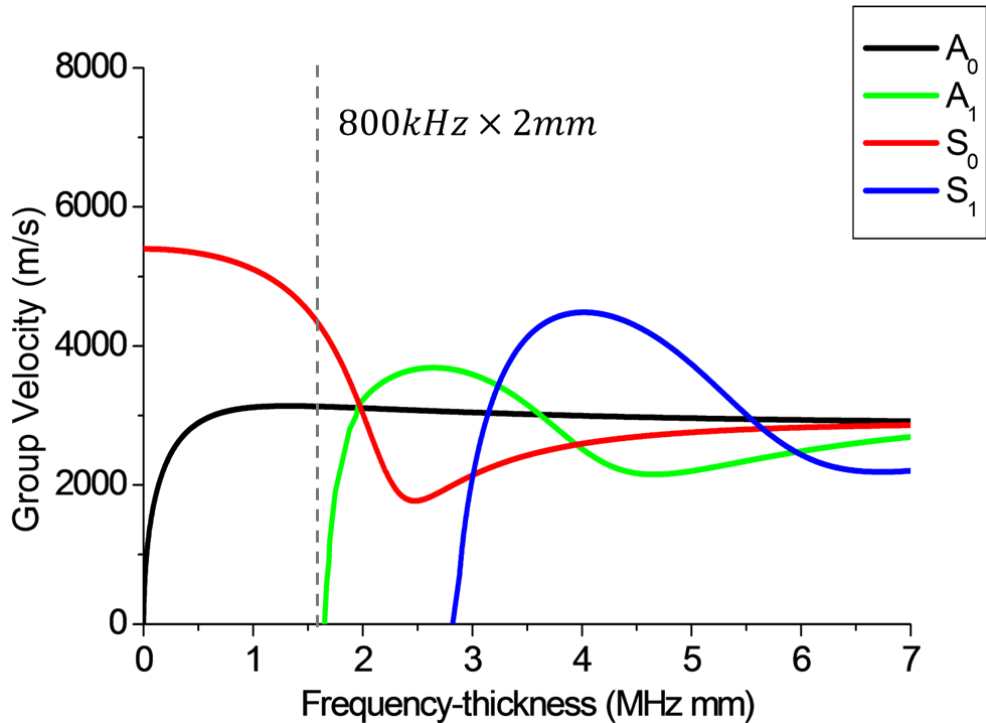
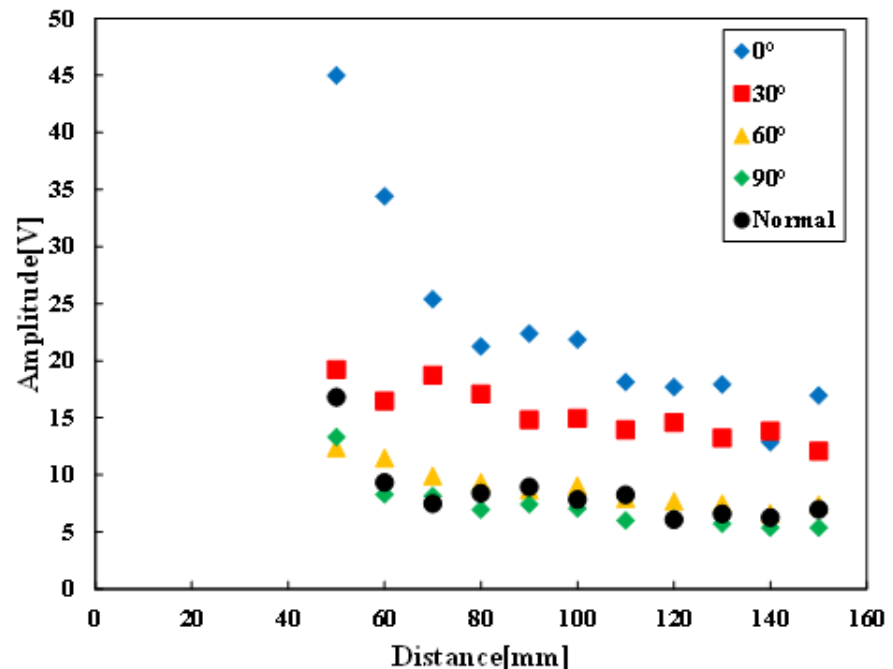
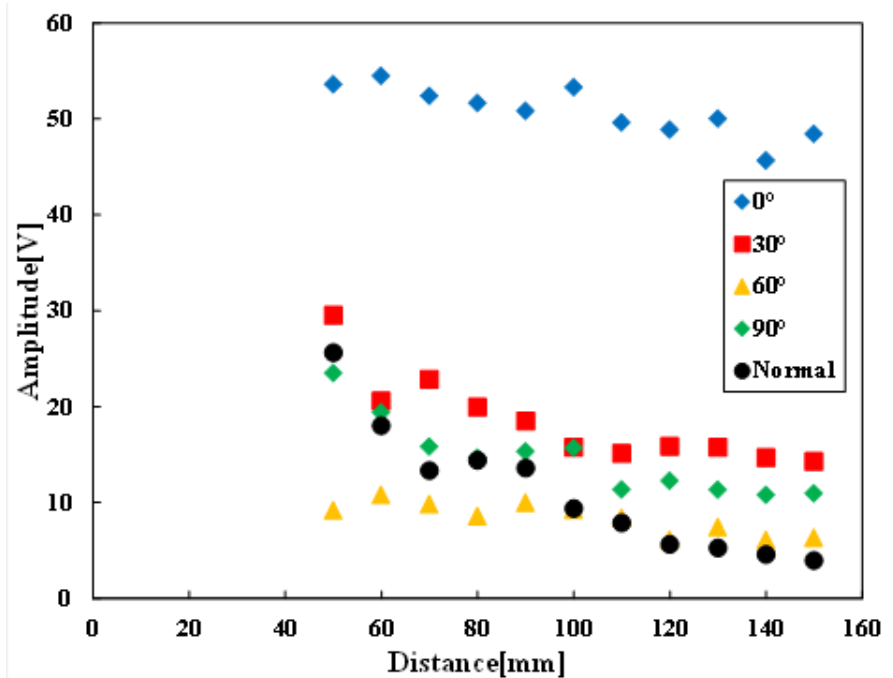


Figure 5.5 Dispersion curves of group velocity for an aluminum plate



(a)



(b)

Figure 5.6 Amplitudes of generated Lamb waves in different directions: (a) S_0 mode; (b) A_0 mode

The amplitudes of S_0 and A_0 modes generated by the rectangular-type PZT actuator in different directions were compared in Figure 5.6, and the result of a circular PZT actuator (diameter 10 mm, thickness 0.5 mm, FUJI Ceramics Co.) at 0° direction was also plotted (see Figure 5.6, “Normal”). It can be seen from Figures 5.6(a) and 5.6(b) that the amplitudes of both S_0 and A_0 mode at 0° direction are much larger than those of other directions using the rectangular-type PZT actuator and the circular-type PZT actuator in 0° direction. It implies that the rectangular-type PZT actuator can effectively concentrate the wave energy in the wave propagation direction, and reduce those wave energies in other directions, leading to the weak reflections of boundaries.

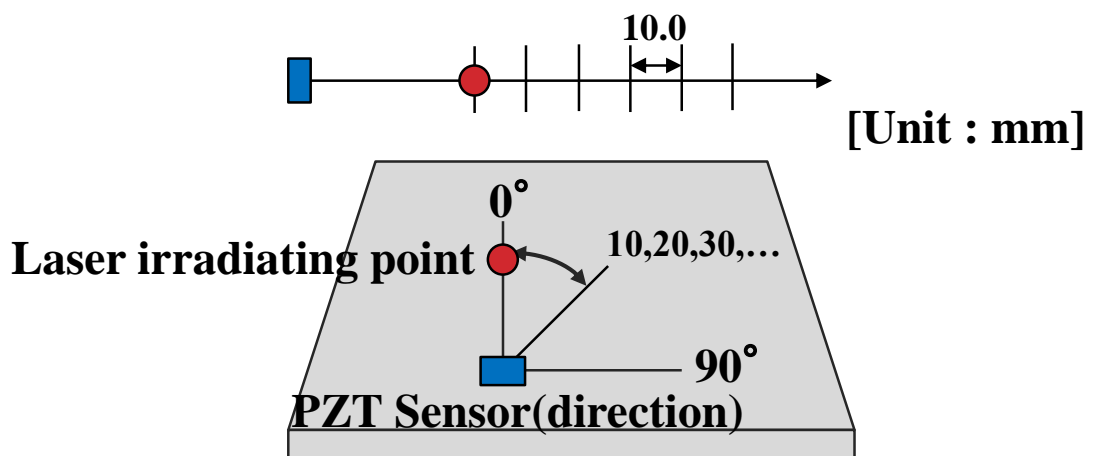


Figure 5.7 Schematic view of experiment (rectangular-type PZT used as sensor)

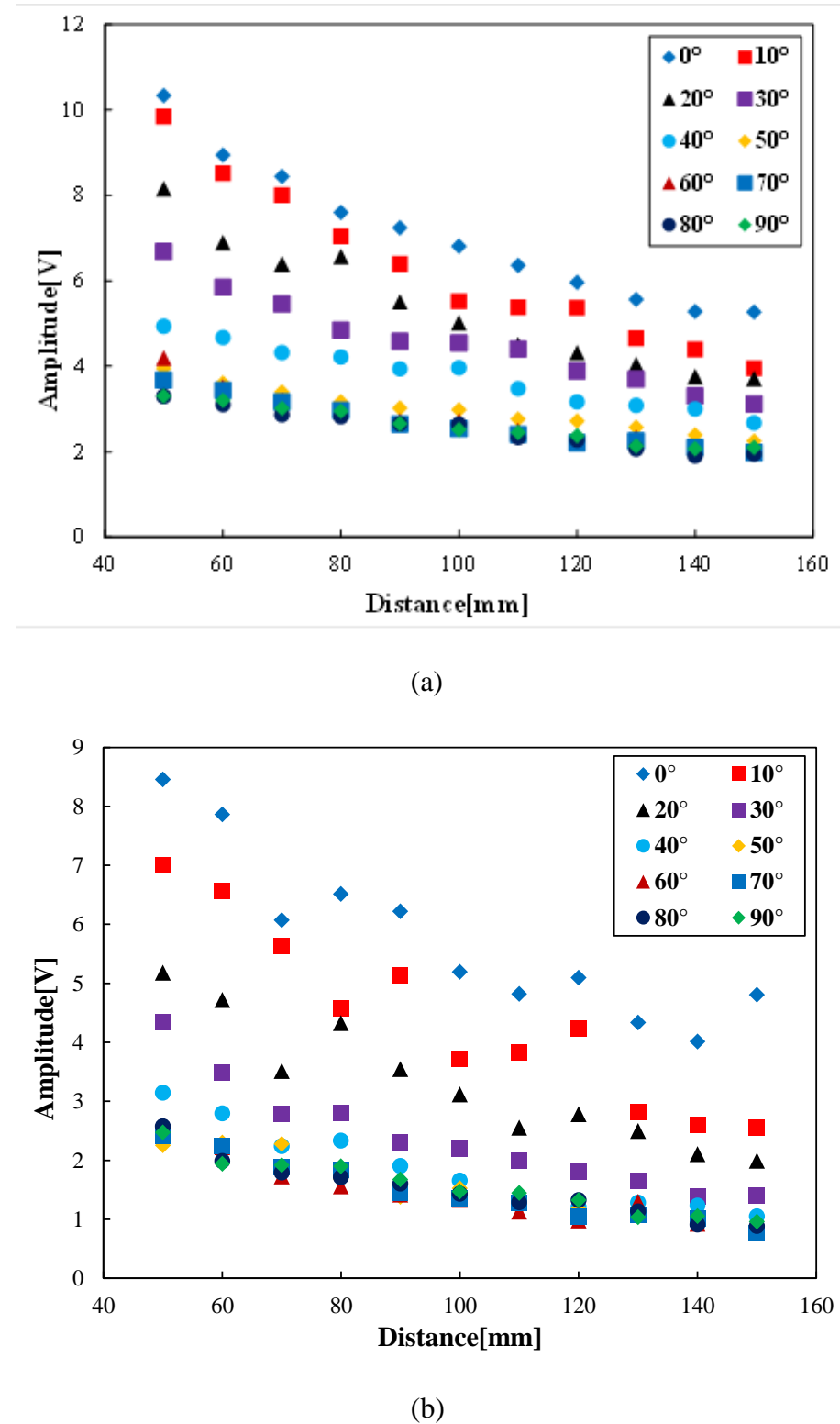


Figure 5.8 Amplitudes of received Lamb waves in different directions: (a) S₀ mode; (b) A₀ mode

When a rectangular-type PZT was used as sensor, and pulse laser irradiation was used as actuator, another experiment as shown in Figure 5.7 was carried out to investigate the sensor sensitivity when receiving S_0 and A_0 modes in different directions and different distances. The amplitudes of S_0 and A_0 modes received by the rectangular-type PZT sensor in different directions were compared in Figure 5.8. It can be seen that the rectangular-type PZT is much more sensitive to S_0 and A_0 Lamb waves at 0° direction than other directions. Therefore, it can mainly receive the wave energy in the wave propagation direction, and effectively avoid the mixing of other unnecessary reflections from boundaries. In the present study, a directional actuator/sensor set (see Figure 5.1) made from rectangular-type PZTs was employed.

5.3 Description of experimental scheme

Based on the above results, an experimental scheme was designed to monitor the change of wave signals during the tensile test, especially at the transition stage from elastic state to plastic state. The corresponding specimen and experimental setup are schematically shown in Figures 5.1 and 5.9. A thin aluminum plate specimen with a circular hole was gradually stretched to the nominal stress of 190 MPa, which was much higher than the previously measured yield stress, i.e., 155 MPa. At the same time, for every stress increment of $1/3$ MPa, Lamb waves were generated and received using the directional PZT actuator/sensor set bonded on the surfaces of the specimen (see Figure 5.1). The wave signals propagating along the straight path between the actuator and the sensor (see Figure 5.9) were recorded corresponding to different stress levels.

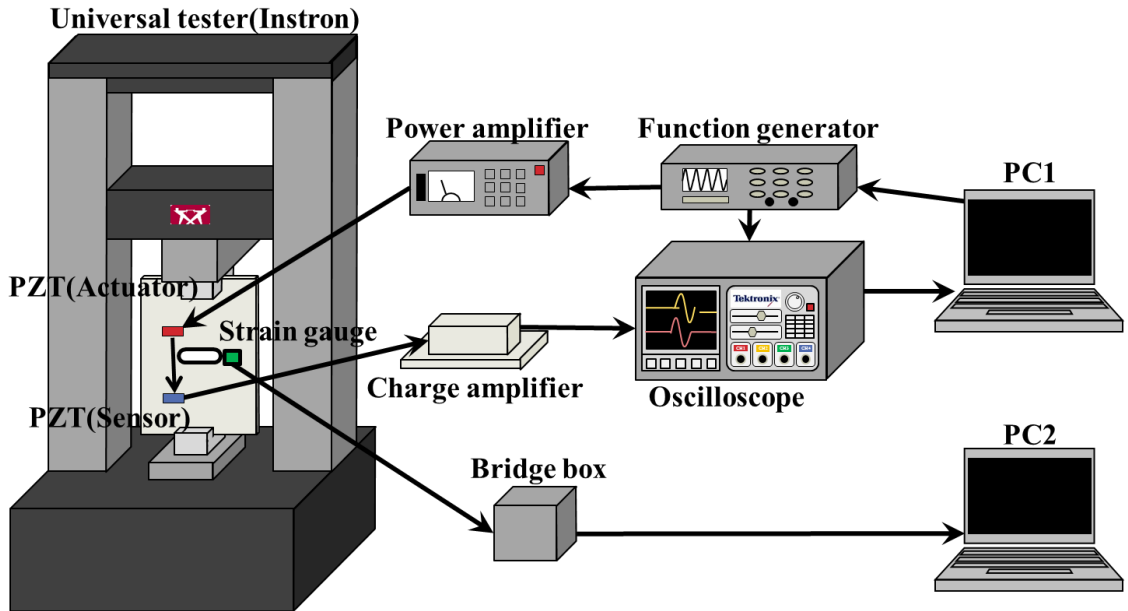


Figure 5.9 Experimental setup

Because of the narrow width of specimen, the target waves might be easily mixed with the reflections from the specimen boundaries, leading to more difficult analysis of wave signals. For this reason, the previously stated fat clay and directional actuator/sensor set with rectangular-type PZTs (see Figure 5.1), were used to increase wave intensity along the straight path between actuator and sensor and suppress the wave intensities from other directions.

5.4 Experimental results

Figure 5.10(a) illustrates the original waveforms at different stress levels obtained by the sensor during the tensile test. The first wave packet is S_0 mode and the second wave packet is A_0 mode. It can be seen that the two wave packets are slightly overlapped and the difference of those wave signals at different tensile loads are very small. To separate the S_0 and A_0 wave packets and amplify the

difference of the wave signals at different stress levels, a pulse compression technique was used. It can be expressed in the following equation:

$$C(t) = \int R(\tau)ref(t + \tau)d\tau \quad (5.2)$$

where $R(t)$ is a received signal and $ref(t)$ is a reference signal. The obtained pulse compression signal $C(t)$ expresses the cross-correlation of the received signal with a reference signal as shown in Figure 5.11. In general, the excitation signal (i.e., the chirp burst wave in this work) is used as the reference signal. This signal processing technique can compress the pulse width in time domain and increase the signal intensity. Figure 5.10(b) demonstrates the wave signals processed by the pulse compression technique at different stress levels. It can be seen that the S_0 and A_0 modes are separated clearly and the difference of wave signals at different stress levels becomes more obvious. Thus, the reported results in the following are based on the processed wave signals by this pulse compression technique. In this case, the meaning of the signal amplitude is different from that of a common PZT sensor signal in the unit of voltage.

Firstly, the amplitude change of S_0 and A_0 modes with the increase of stress level in the specimen was investigated. Figure 5.12 shows the amplitude variation of S_0 mode. The amplitude of S_0 mode increases slightly with the increase of the tensile load in elastic deformation. However, at around 130 MPa, it starts to decrease. At 155 MPa, it increases remarkably again. For the case of A_0 mode in Figure 5.13, unlike that of S_0 wave mode, the amplitude of A_0 mode decreases as the tensile load increases in elastic state. This decrease stops at around 130 MPa, corresponding to the lowest amplitude. Then, the amplitude starts to increase slowly, and grows rapidly when the stress level in the specimen reaches 155 MPa.

Note that, prior to 155 MPa, the variations of the wave amplitudes of both S_0 and A_0 modes in Figures 5.12 and 5.13 are very small.

Secondly, the difference of Lamb wave signals related to different loads was evaluated using wavelet analysis. Note that the intact wave signals containing both S_0 and A_0 wave packets were processed. In wavelet analysis, as shown in Figure 5.14, a signal can be divided into an approximate primary subset (low frequency information, A1) and a detailed subset (high frequency information, D1). A1 can then be further divided into a second-level approximate primary subset (A2) and its detailed subset (D2), and this process can be repeated. In this work, Daubechies wavelet (db10) was used as the mother wavelet. The decomposition level is 3 and the wave signals were decomposed into 4 subsets (A3+D3+D2+D1) in different frequency bands. A signal index I was defined as follows to evaluate the change of wave signals during the tensile test

$$I(\sigma_i) = \sqrt{\frac{\sum_n [w(X_n; \sigma_i) - w_b(X_n; \sigma_b)]^2}{\sum_n [w_b(X_n; \sigma_b)]^2}} \quad (5.3)$$

where X is one of the decomposed subsets (A3, D3, D2, D1), n is the number of sampling data, w is the n th number of the decomposed parameter X of subset at the stress σ_i , and $w_b(X_n; \sigma_b)$ is the corresponding baseline signal recorded at the stress level of σ_b . Here, the wave signal obtained in the unloaded specimen was used as the baseline signal, i.e., $\sigma_b = 0$. The signal index I of Lame waves was calculated and shown in Figure 5.15. It can be seen that the I corresponding to the A3, D3 and D2 subsets present some meaningful and interesting variations, but the I corresponding to the D1 subset are very scattered around a value of 1.35,

which is meaningless and may be caused by noises. In Figure 5.15, all I corresponding to the A3, D3 and D2 subsets increase with the stress level, and a sudden increase appears at 160 MPa for the D3 and D2 subsets, while the appearance of a sudden increase in the I of the A3 subset is at 170 MPa (Figure 5.15(a)). In this case, we can also find that the increasing rate of I increases remarkably from 160 MPa.

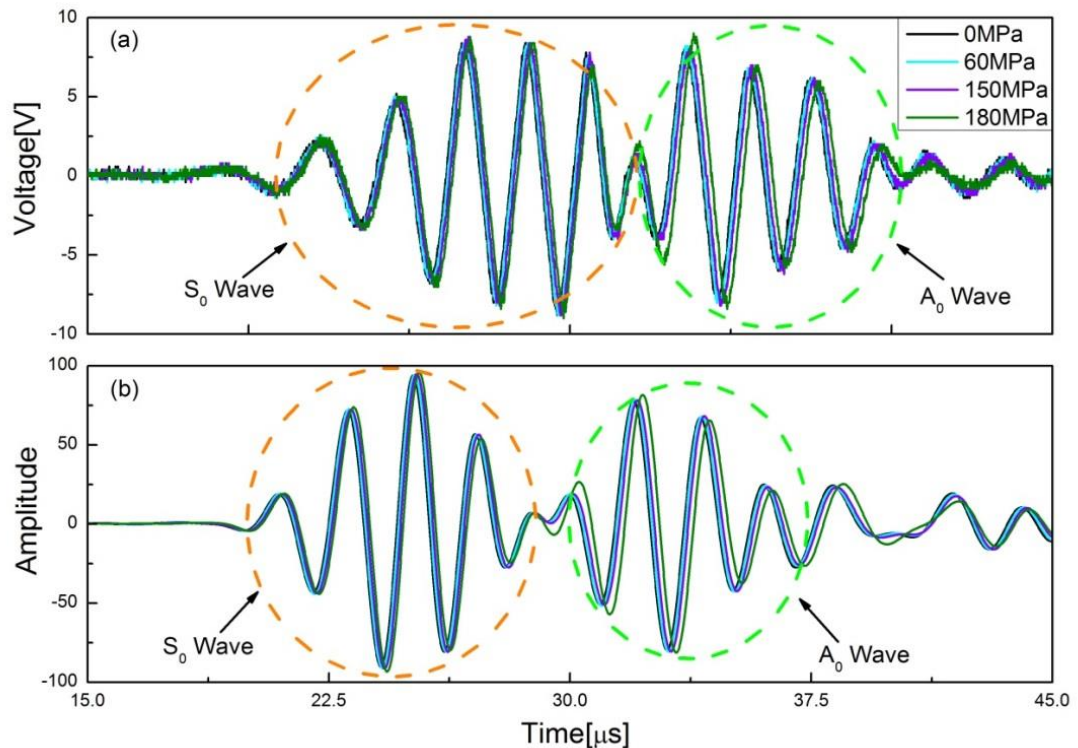


Figure 5.10 Wave signals: (a) original wave signals at different stress levels; (b) wave signals processed by pulse compression technique at different stress levels

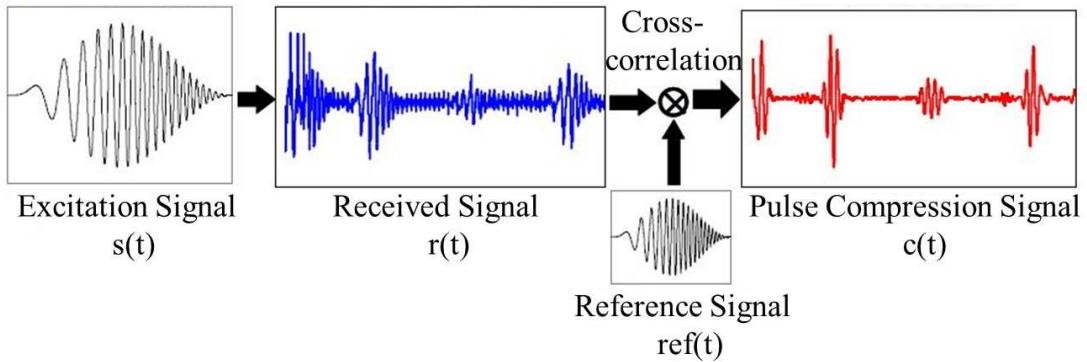


Figure 5.11 Pulse compression technique

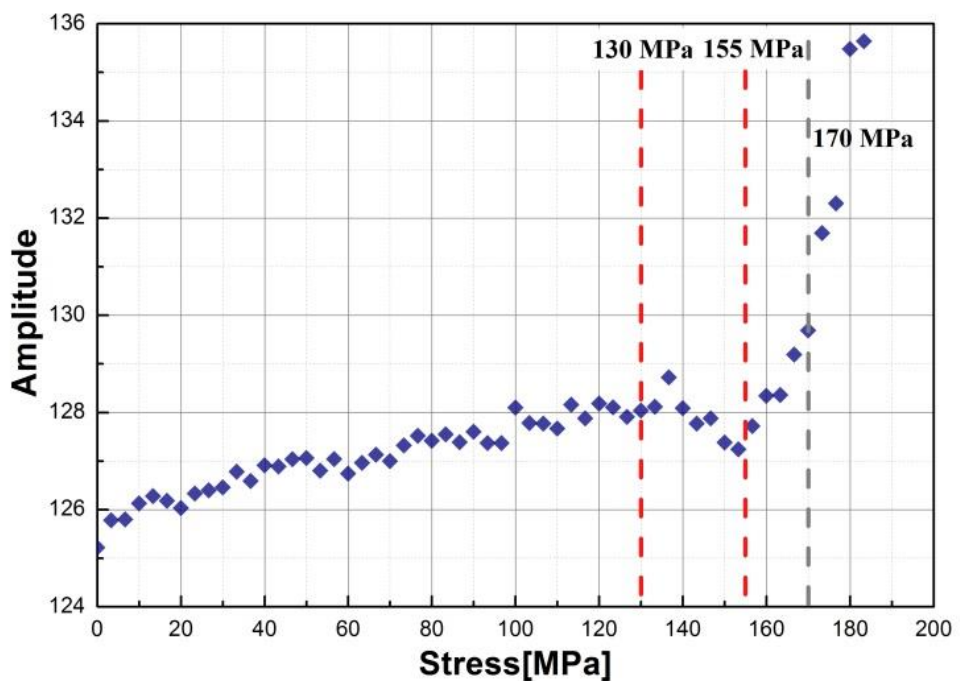


Figure 5.12 Amplitude change of S_0 Lamb mode with the increase of stress level
in the specimen

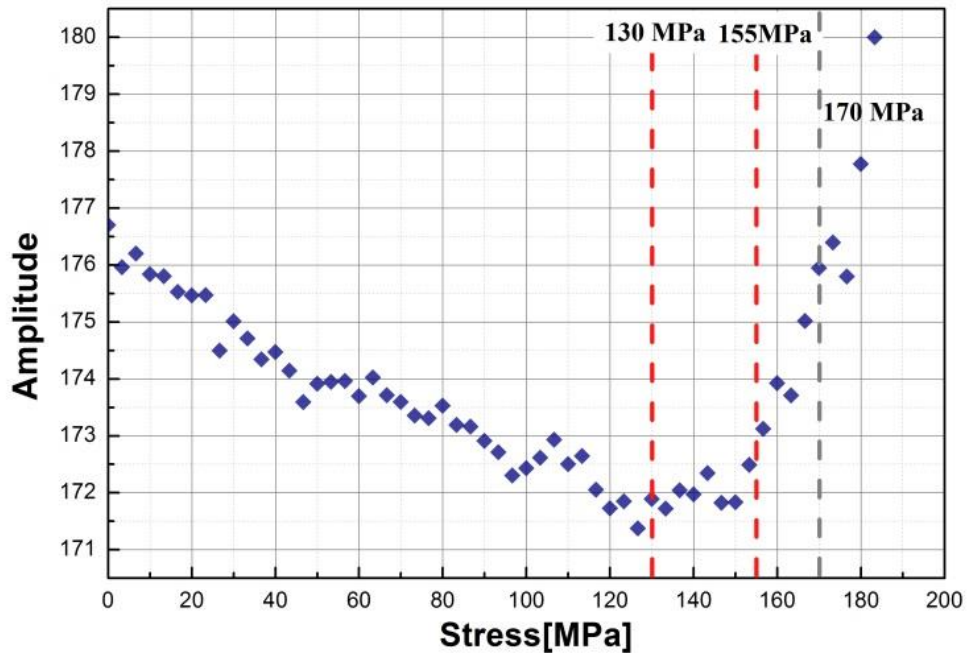


Figure 5.13 Amplitude change of A_0 Lamb mode with the increase of stress level
in the specimen

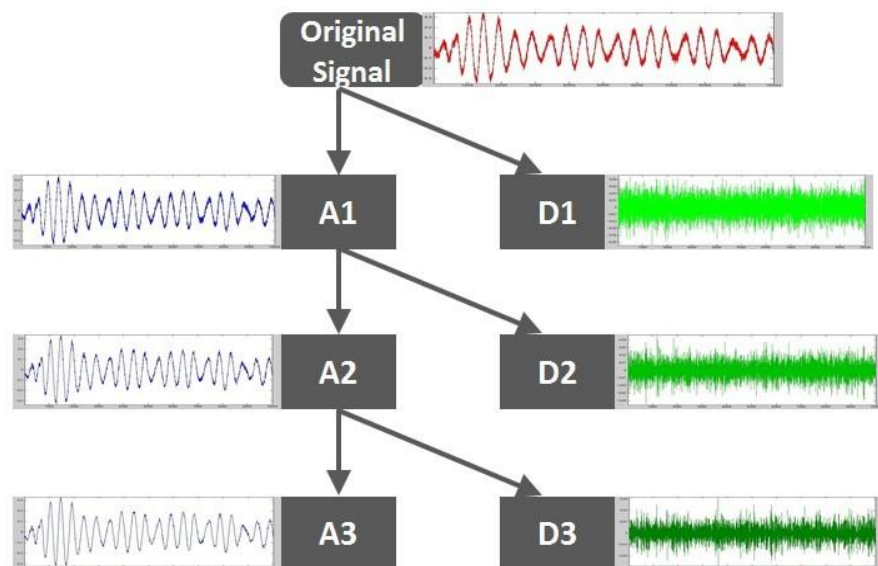


Figure 5.14 Wavelet analysis of signals

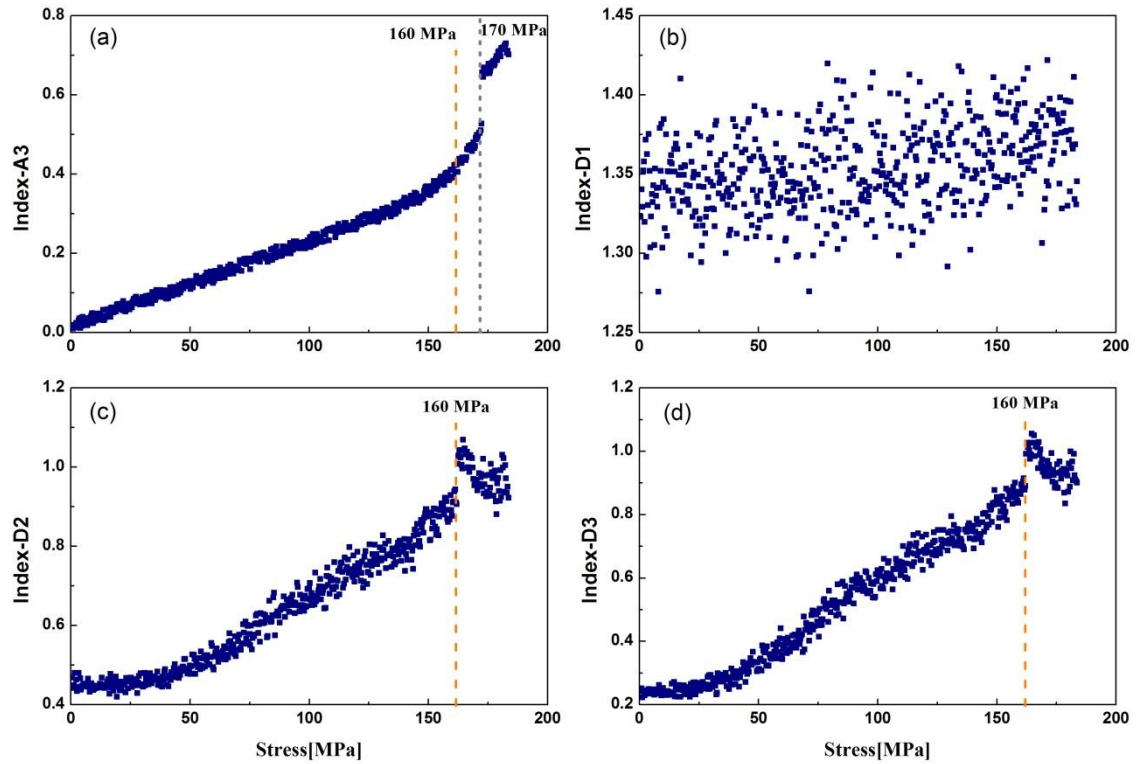


Figure 5.15 Signal index I related to different stress levels: (a) A3; (b) D1; (c) D2; (d) D3

5.5 Discussion

To further understand the above experimental results, a series of numerical simulations were conducted to explore the plasticity evolution around the hole during tensile test by using a commercial FEA software, ABAQUS. Here, a 2D model of a rectangular plate with a circular hole under stretching in plane stress was built up, and its sizes and material parameters are the same with those in the experiment.

The evolution of plastic zone around the hole at the stress levels from 75 MPa to 180 MPa is shown in Figure 5.16. The plastic zone is represented by dark grey color. When the stress in the specimen reaches 75 MPa, two small plastic

zones initially appear at both sides of the hole (Figure 5.16(a)). With the increase of the applied stress, they gradually become larger (Figure 5.16(b)). Figure 5.16(c) shows the plastic state when the stress is up to 155 MPa. At this stage, the position of the strain gauge goes into plastic state. As the applied stress continues increasing, plastic zones extend towards to the direction at the angle of $\pm 45^\circ$ (Figures 5.16(d) and 5.16(e)) due to shear banding, and the size of plastic zones grows rapidly when the stress increases from 170 MPa to 180 MPa (Figure 5.16(f)).

For convenience of discussion, the above process can be categorized into three stress stages: (1) $0 \text{ MPa} \sim 130 \text{ MPa}$, (2) $130 \text{ MPa} \sim 155 \text{ MPa}$, (3) $155 \text{ MPa} \sim 180 \text{ MPa}$.

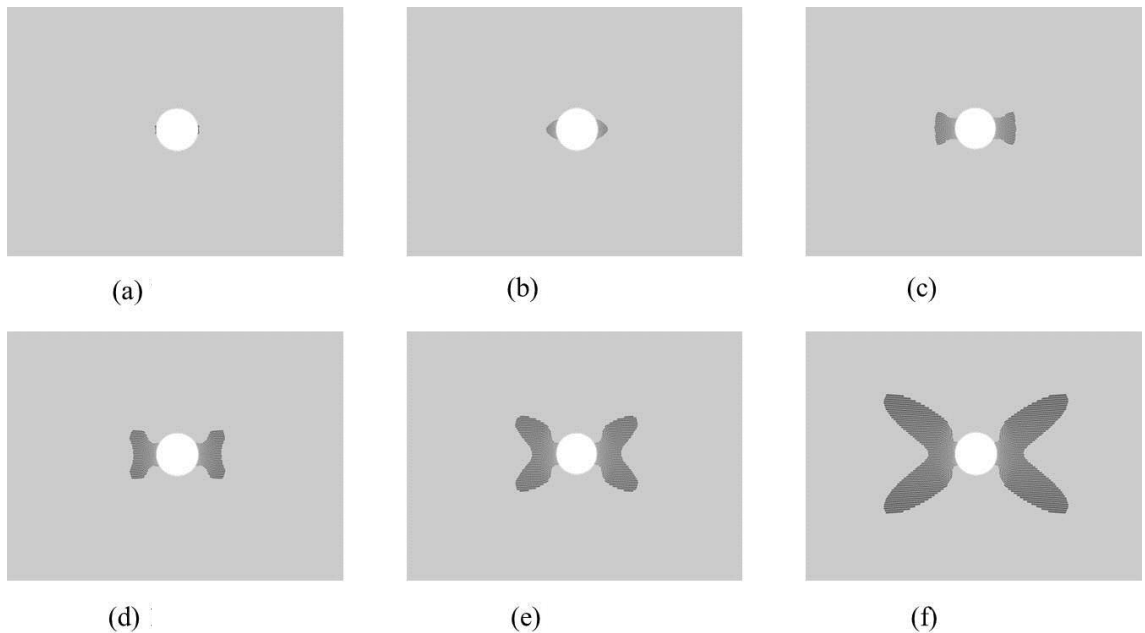


Figure 5. 16 Evolution of plastic zone during loading process: (a) 75 MPa; (b) 120 MPa; (c) 155 MPa; (d) 160 MPa; (e) 170 MPa; (f) 180 MPa

5.5.1 0 MPa~130 MPa

At this stage, the amplitude variation tendency of S_0 wave mode is opposite to that of A_0 mode (see Figures 5.12 and 5.13). For a particle-spring model as shown in Figure 5.17, it is well-known that, in S_0 wave mode, particles vibrate along the wave propagation direction, meanwhile, in A_0 wave mode, particles vibrate along the normal direction or plate thickness direction. Since the applied axial stress direction in the specimen is the same with that of particle movement in S_0 wave mode, this may promote the propagation of S_0 wave mode and amplify its amplitude (see Figure 5.12). On the other hand, since the applied axial stress is vertical to the particle movement direction in A_0 wave mode, the propagation of A_0 wave mode may be restrained by the axial stress (see Figure 5.13). This is just similar to the case where the transverse vibration amplitude of a spring can be suppressed by stretching the spring. In addition, the linear increase of the corresponding to the A3, D3 and D2 subsets also clearly indicates that the influence of the increase of stress levels on Lamb wave propagation is stable.

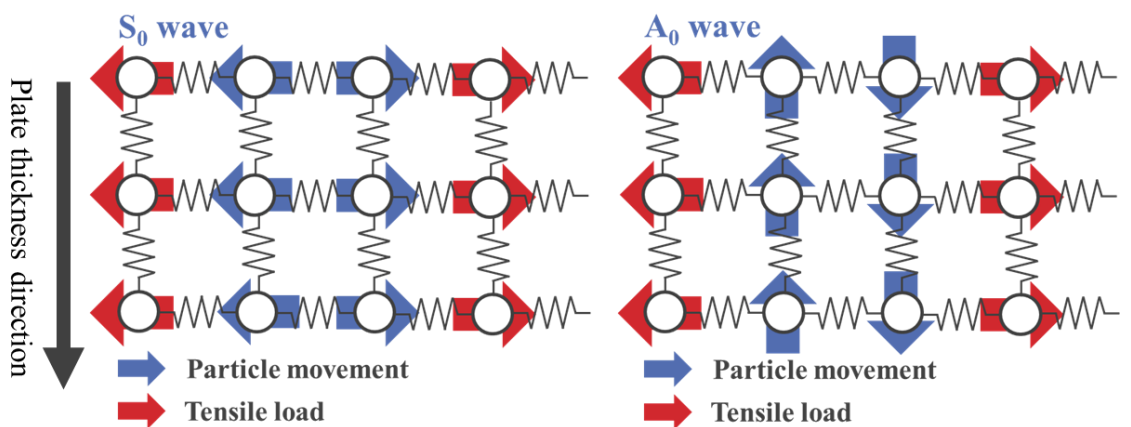


Figure 5.17 Lamb wave propagation model (one dimension)

From numerical results in Figure 5.16, we can see that the plasticity occurs initially when the stress is up to 75 MPa. However, at this stress level or even up to 130 MPa, we cannot identify any obvious change in either amplitude or I , which means that linear Lamb waves (S_0 and A_0 wave modes) are insensitive to the initial plastic deformation. At this stage, the plastic zone is too small to affect the wave propagation (Figures 5.16(a) and 5.16(b)).

5.5.2 130 MPa~155 MPa

At this stage, unlike the previous stress stage, the amplitude of S_0 wave mode decreases gradually (see Figure 5.12), while the amplitude of A_0 wave mode increases (see Figure 5.13). These changes may be due to the softening caused by plasticity evolution. At end of this stage (i.e., 155 MPa), the plastic zone extends to the position of 5 mm away from the hole as shown in Figure 5.1 and Figure 5.16(c). Although the plastic zone is still small, it already starts to influence the amplitude of wave signals, which means the plasticity can be firstly discovered by the amplitude change of wave signals. However, the change tendency of I is not obvious at this stage (see Figure 5.15). Therefore, the change of wave amplitude is more sensitive to mild plastic deformation than that of I .

5.5.3 155 MPa~180 MPa

At the starting point of this stage, i.e., 155 MPa, both wave amplitudes of S_0 and A_0 modes increase remarkably (see Figures 5.12 and 5.13), implying the significant softening of material or springs in Figure 5.17 caused by severe plasticity. However, the absolute increases of the wave amplitudes are small by observing the values on the longitudinal axe of Figures 5.12 and 5.13. Moreover,

the sudden increases of I for the D3 and D2 subsets at 160 MPa can be identified from Figures 5.15(c) and 5.15(d), which are caused by the extension of plastic zone. At the same stress level, the increasing rate of I corresponding to the A3 subset begins to increase slightly in Figure 5.15(a). Therefore, the detailed subsets (i.e., D3 and D2) are more sensitive to plasticity than the approximate primary subset (i.e., A3 subset). As the load keeps on going, a sudden increase of the I for the A3 subset also appears at 170 MPa. Besides, the amplitudes of both S_0 and A_0 wave modes in Figures 5.12 and 5.13 increase more rapidly from 170 MPa. This phenomenon may be caused by the geometry change of the hole in severe plasticity. In this case, because the circular profile of the hole changes into elliptic one with its major axis parallel to the wave propagation direction, the waves can transmit through the hole area more easily. Moreover, compared with the absolute changes of wave amplitudes in Figures 5.12 and 5.13, the absolute changes of I are much higher in Figure 5.15, indicating that I is more suitable for monitoring the severe plasticity.

5.6 Conclusion

In this chapter, we developed a real-time monitoring technique for local plasticity using Ultrasonic Lamb waves. To verify the effectiveness of the proposed technique, tensile test of a thin plate specimen with a circular hole was conducted. Stress concentration was generated around the hole, leading to local plasticity. Two rectangular-type commercial PZTs attached on the specimen were used as a directional actuator/sensor set to collect strong and clear wave signals during the tensile test. The path between the actuator and the sensor was chosen to monitor

the appearance of the local plasticity. Wave signals corresponding to different tensile stress were processed using a pulse compression technique. The amplitude changes of S_0 and A_0 wave modes with the increase of the tensile stress in the specimen were investigated, and a signal index I based on wavelet analysis was defined to study the difference of Lamb wave signals caused by plasticity. To further understand the experimental results, a series of FEA numerical simulations of the tensile test were conducted to explore the plasticity evolution process around the hole. Based on the experimental and numerical results, it can be found that both S_0 and A_0 wave modes are insensitive to the appearance of initial plasticity. As the plastic zone gradually extends larger, the amplitudes of S_0 and A_0 wave modes show their different change tendencies compared with those in elastic stage. It is also found that the amplitude change is more sensitive to mild plasticity than the change of I , while the change of I caused by severe plasticity is more obvious than the amplitude change. Therefore, the proposed technique can effectively monitor the evolution of plasticity.

References

- [1] C. R. Farrar and K. Worden. An introduction to structural health monitoring. *Philosophical Transactions of the Royal Society A: Mathematical, Physical and Engineering Sciences*, 2007, 365: 303-315.
- [2] S. Kulkarni and J. Achenbach. Structural health monitoring and damage prognosis in fatigue. *Structural Health Monitoring*, 2008, 7: 37-49.
- [3] S. Nagarajaiah, S. Dyke, J. Lynch, A. Smyth, A. Agrawal, M. Symans and E. Johnson. Current directions of structural health monitoring and control in USA. *Advances in Science and Technology*, 2009, 56: 277-286.
- [4] J.-H. Yi, D. Kim, S. Go, J.-T. Kim, J.-H. Park, M. Q. Feng and K.-S. Kang.

- Application of structural health monitoring system for reliable seismic performance evaluation of infrastructures. *Advances in Structural Engineering*, 2012, 15: 955-968.
- [5] D. Zhang, Y. Bao, H. Li and J. Ou. Investigation of temperature effects on modal parameters of the China National Aquatics Center. *Advances in Structural Engineering*, 2012, 15: 1139-1154.
 - [6] N. Hu, T. Shimomukai, H. Fukunaga and Z. Su. Damage identification of metallic structures using A0 mode of Lamb waves. *Structural Health Monitoring*, 2008, 7: 271-285.
 - [7] A. Maslouhi. Fatigue crack growth monitoring in aluminum using acoustic emission and acousto-ultrasonic methods. *Structural Control and Health Monitoring*, 2011, 18: 790-806.
 - [8] H. Cho and C. J. Lissenden. Structural health monitoring of fatigue crack growth in plate structures with ultrasonic guided waves. *Structural Health Monitoring*, 2012, 11: 393-404.
 - [9] S. S. Kessler, S. M. Spearing and C. Soutis. Damage detection in composite materials using Lamb wave methods. *Smart Materials and Structures*, 2002, 11: 269.
 - [10] N. Hu, Y. Cai, G. Zhu, C. Tsuji, Y. Liu and Y. Cao. Characterization of damage size in metallic plates using Lamb waves. *Structural Health Monitoring*, 2011, 1475921711414230.
 - [11] N. Hu, T. Shimomukai, C. Yan and H. Fukunaga. Identification of delamination position in cross-ply laminated composite beams using S₀ Lamb mode. *Composites Science and Technology*, 2008, 68: 1548-1554.
 - [12] Y. Zou, L. Tong and G. Steven. Vibration-based model-dependent damage (delamination) identification and health monitoring for composite structures—a review. *Journal of Sound and Vibration*, 2000, 230: 357-378.
 - [13] Y. Yan and L. Yam. Detection of delamination damage in composite plates using energy spectrum of structural dynamic responses decomposed by wavelet analysis. *Computers & Structures*, 2004, 82: 347-358.
 - [14] R. O. Ritchie. Mechanisms of fatigue-crack propagation in ductile and

- brittle solids. *International Journal of Fracture*, 1999, 100: 55-83.
- [15] K. S. Chan. A microstructure-based fatigue-crack-initiation model. *Metallurgical and Materials Transactions A*, 2003, 34: 43-58.
 - [16] D. V. Truong, H. Hirakata and T. Kitamura. Effect of loading frequency on fatigue crack growth between a submicron-thick film and a substrate. *JSME International Journal Series A*, 2006, 49: 370-375.
 - [17] W. France Jr. Effects of stress and plastic deformation on the corrosion of steel. *Corrosion*, 1970, 26: 189-199.
 - [18] X. Gong and S. Toyooka. Investigation on mechanism of plastic deformation by digital speckle pattern interferometry. *Experimental Mechanics*, 1999, 39: 25-29.
 - [19] S. Toyooka, R. Widiastuti, Q. Zhang and H. Kato. Dynamic observation of localized strain pulsation generated in the plastic deformation process by electronic speckle pattern interferometry. *Japanese Journal of Applied Physics*, 2001, 40: 873.
 - [20] M. Kamaya, A. J. Wilkinson and J. M. Titchmarsh. Measurement of plastic strain of polycrystalline material by electron backscatter diffraction. *Nuclear Engineering and Design*, 2005, 235: 713-725.
 - [21] M. Kamaya. Measurement of local plastic strain distribution of stainless steel by electron backscatter diffraction. *Materials Characterization*, 2009, 60: 125-132.
 - [22] P. B. Nagy. Fatigue damage assessment by nonlinear ultrasonic materials characterization. *Ultrasonics*, 1998, 36: 375-381.
 - [23] J. Herrmann, J.-Y. Kim, L. J. Jacobs, J. Qu, J. W. Littles and M. F. Savage. Assessment of material damage in a nickel-base superalloy using nonlinear Rayleigh surface waves. *Journal of Applied Physics*, 2006, 99: 124913.

Chapter 6

Summary and Future work

6.1 Summary of the thesis study

In this dissertation, we develop some new damage identification approaches for ultrasonic Lamb wave-based SHM and NDE of engineering structures. Besides, a pseudospectral Mindlin plate element is built up to simulate wave propagation in plate-like structures, and an aluminum plate with through-thickness elliptically-shaped damage is employed to study the physical mechanisms behind wave propagation and wave interaction with damage.

The conclusions from different chapters are summarized as follows:

1. Chebyshev polynomials are used to construct a pseudospectral Mindlin plate element. Chebyshev-Gauss-Lobatto points are used as the grid points and the quadrature points of the elemental mass matrix and stiffness matrix. A lumped elemental mass matrix is generated due to the discrete orthogonality of Chebyshev polynomials and overlapping of the quadrature points with the grid points. To verify the effectiveness and high accuracy of the new plate element, wave propagation problems in a long aluminum beam and an aluminum plate with a hole are solved using the present element and the commercial ABAQUS software or experiments respectively. The results show that the new plate element can yields very good results compared with those of ABAQUS and experiments.
2. The influences of Lamb wave dispersion, excitation frequency in wave signals, the shape of damage, and incident angle of Lamb wave on the relative reflection intensity (RRI) from through-thickness elliptically-shaped damages in an aluminum plate are studied. The results

present that: a) Lamb wave dispersion has no obvious effect on RRI; b) RRI differs with the different of the shape of damage. It is implied that the reflected wave from damage includes some information on the shape of damage. For the same damage, a higher RRI can be generated when the direction of Lamb wave propagation is perpendicular to the long or major axis direction of the elliptical hole; c) there exist one or multiple optimal excitation frequencies (OEF) for a damage to induce the strongest RRI. This phenomenon may be caused by the resonance at the local damaged region. This result can be helpful to design input wave signals; d) the highest RRI decreases and becomes more insensitive to the excitation frequency with the increase of the incident angle of Lamb wave. This result can be helpful to design actuator/sensor placements.

3. A structural damage imaging approach is developed to locate damage as well as evaluate the shape and size of damage. In this approach, a new wave energy flow (WEF) map concept is proposed and a simple signal processing algorithm is employed to construct the WEF map, and multiple lead zirconate titanate (PZT) sensors are employed to avoid possibly missing some severe defects or erroneous recognition in damage detection. Two aluminum plates with an elliptical through-hole or a non-penetrating slit and a CFRP laminated plate with invisible internal delamination are used to experimentally validate the proposed technique. The results show that: a) for aluminum plates with an elliptical through hole or a non-penetrating slit, the position as well as the shape and size of the hole are pictured by the WEF map; b) for the CFRP laminated plate

with internal delamination, the position is accurately identified but the evaluated delamination area is slightly smaller than the real one. The deviation on the size of delamination is due to the material anisotropy of CFRP.

4. A real-time monitoring technique for local plasticity using ultrasonic Lamb waves is developed. To verify the effectiveness of the proposed technique, an experiment on performing tensile test and generation/collection of Lamb waves simultaneously is designed. A thin aluminum plate with a circular hole is used in experiment to induce high stress concentration around the hole. Two rectangular-type PZTs attached on the specimen are placed to make the path between them through the area of stress concentration. The changes of the amplitude of S_0 and A_0 wave modes and a signal index I based on wavelet analysis with the increase of the tensile stress in the plate are investigated. A series of numerical stress analysis of the tensile plate are conducted to helpful interpret the changes. The results show that: a) at the stage of elastic deformation, the amplitude variation tendency of S_0 wave mode is opposite to that of A_0 mode, that is, the amplitude of S_0 wave mode increases while the amplitude of A_0 wave mode decrease with the increase of the stress in the plate; b) both S_0 and A_0 wave modes are insensitive to the appearance of initial plasticity; c) the amplitudes of S_0 and A_0 wave modes show their different change tendencies when the plastic zone becomes enough large, the amplitude decreases for S_0 wave mode while increases for A_0 wave mode; d) the I increases with the

increase of the stress in the plate, while a sudden change emerge when the plastic zone becomes enough large; e) the amplitude change is more sensitive to mild plasticity than the change of I , while the change of I caused by severe plasticity is more obvious than the amplitude change.

6.2 Further work

The damage identification approaches developed in this dissertation are not perfect so far, the following remaining tasks should be undertaken as a continuation of the present research:

For the structural damage imaging approach in chapter 4:

1. In order to implement a quick damage prognosis, the scanning efficiency of the inspection region needs to be enhanced. An algorithm for optimization of the positions of the scanning points should be developed to reduce the number of scanning points and save the scanning time.
2. It can be seen from Figures 4.6(d) and 4.7(d) that the damage area cannot be distinguished quickly and clearly from health area. Thus, an improved algorithm for constructing damage diagnostic image should be developed to enhance the difference between health area and damage area, especially for minor defects.
3. It can be seen from Figures 4.11(d) and 4.13 that the quality of the damage diagnostic image would be affected by material anisotropy. Thus, the effect of material anisotropy on wave attenuation should be quantitatively evaluated to compensate the loss.
4. The effectiveness of the present approach on shell structures should be

proven.

5. The effectiveness of the present approach on other types of damage should be proven.
6. All experiments in this dissertation are aimed at a single damage in the inspection region. The case of multi-damages in the inspection region should be considered, and the minimum distance necessary to detect two successive damages should be estimated.
7. Other effects such as thermal residual stress can be considered in the present approach to extend its application field. For example, thermal stress is crucial in ship structures. Thus, the improved approach can be used for residual stress identification in those structures.

For the real-time technique for monitoring local plasticity or micro-level damages:

1. Only using a path of wave propagation to monitor local plasticity may be not enough. A sensor network can be used to achieve full-range monitoring for local plasticity.
2. Other better signal processing techniques should be developed. For plastic zone, the change in signal waves is very small. Most current signal processing techniques cannot extract useful information from the signals. Therefore, signal processing techniques suitable for plastic zone are an imperative.
3. The present work only studied the metallic aluminum. The situation on other types of materials should be investigated, such as composite materials.